Power to Fuel: Optimisation and characterisation of a small scale methanol synthesis reactor

A.C. de Jong

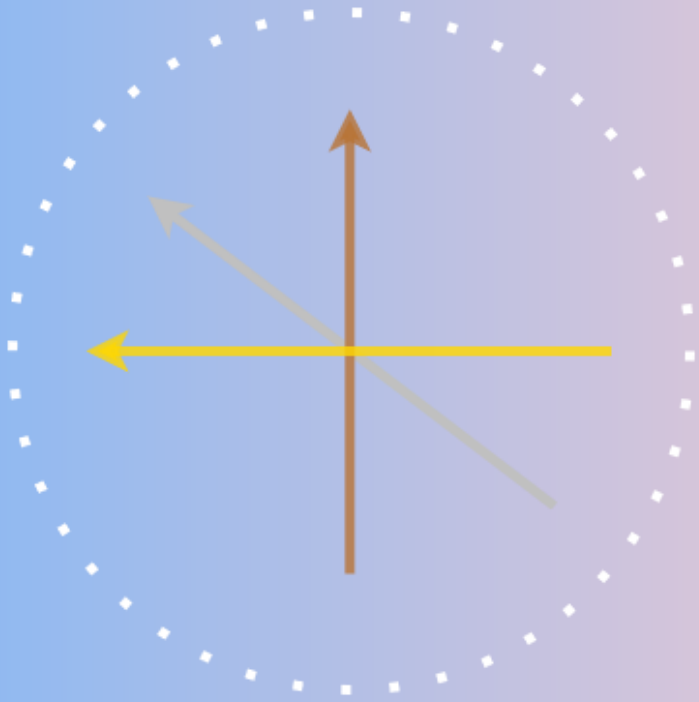

Technische Universiteit Delft

TU Delft

ZEF

Power to Fuel: Optimisation and characterisation of a small scale methanol synthesis reactor

by

A. C. de Jong

to obtain the degree of Master of Science
at the Delft University of Technology,
to be defended publicly on Wednesday December 7, 2022 at 12:00 AM.

Student number:	4582780	
Duration:	January 26, 2022 - December 7, 2022	
Supervisor:	Prof. dr. ir. W. de Jong,	TU Delft
Daily Supvervisors:	ir. P.S.M. Vroegindeweij	ZEF B.V.
	ir. J. van Kranendonk	ZEF B.V.
Thesis committee:	Prof. dr. ir. W. de Jong, Chairman	TU Delft
	Prof. dr. ir. E. Goetheer	TU Delft
	Dr. ir. H.B. Eral	TU Delft
	ir. P. S. M. Vroegindeweij	ZEF B.V.

This thesis is confidential and cannot be made public until December 7, 2024.

An electronic version of this thesis is available at `http://repository.tudelft.nl`.

TU Delft

”The life of a designer is no parade of victories.
There are innumerably more failures.
But they must not stop us”
Korolev - Public Service Broadcasting

Acknowledgements

"I am he as you are he as you are me
And we are all together"
I am the walrus - The Beatles

Having a flashback on this thesis one things stands out. That is the people with whom this work has been created, and therefore this page at the start of this work is reserved for you.

Many thanks to ZEF teams 8.5-9,10,11. It was a joy to work with you all, and made each day at ZEF like a day at the beach. Special thanks to the AEC team members on the bunker: Bart, Hans, Samarth, and of course safety guy. The experience in tackling the challenges faced there helped me enormously in commissioning for the reactor. Thank you Seda for testing the initial ideas we had on the previous reactor. Geert and Stijn you came in when the reactor was at the end of the commissioning cycle. You were thrown into the deep, and now you guys are going to keep improving on the reactor with undoubtedly success. None of this reactor could have been build without the extensive help of Stephan. Your insights in many of the mechanical designs was imperative. Thanks for everything during the 3 day rush! Blas, Kunal, Khaled thank you so much for all the drinks, coffee, jokes, insights, help, and good times. Doing our thesises in parallel was such a highlight of this work, and I cannot wait to see your guys next work. Special thanks to my supervisor Wiebren, for the guidance, enthusiasm and insights. No wonder that multiple courses which shaped the direction of my studies in Delft where given by you.

The core team of ZEF is the reason this whole project could even happen. Hessel, thank you so much for all the encouragement, the life advice and your endless enthusiasm. It has helped me to learn a lot outside the engineering aspects of these types of projects. Mrigank, during the commissioning you had many valuable insights and words of encouragement which helped in getting the reactor to work. Discussions like the paper vs plastic bag are definitely something I am going to miss. Ulrich, you were the first person of ZEF I met, and thank you so much for being part of the story that is ZEF. The encouragements and personal stories are definitely something I will remember for a very long time. Jan, thank you so much for allowing me to experiment so much with models and designs. For the help in so many aspects in this work, the reactor would have run in reverse otherwise. For always being happy to help when something was not as should be. Paul, thank you so much for everything: just try to count how often I have cited your work. Your support, guidance, and of course setting the bar in many aspects. This work would not even be half of what it is without your help, thank you so much. Especially for the most important lesson, can a result of something be true? ZEF, patent your story. It will be an exquisite series!

Twan, thank you for being such a good housemate, the distractions from work are refreshing! Marilene, you were one of the first to encounter my maths ideas. Thank you so much for all the guidance, support and advice. I definitely would not have been able to get to here. Philip and Sybel, your impact on this work is notable! All the advice, chats, jokes, and evenings off are what allowed me to remain effective at my work, and is why I could get where I am. Mom and Dad, from day one you were there for me and allowed me to do so many science experiments throughout all these years. For being there always when the going got though, and having the patience with all of it. Your efforts is why this work exists, and your name should be on the front of it.

To you who I have forgotten to name up here, my apologies. Our encounter in life has likely had an effect on this work, and feel free to scribble your name on here somewhere. Thanks so much!

A.C. de Jong
Delft, November 2022

Abstract

In the effort against climate change the company ZEF has as its target to make methanol (CH_3OH) out of atmospheric CO_2; a process which can be seen as power-to-fuel and/or power-to-x. In light of the developmental cycle within ZEF a new reactor with an increased size and enhanced mass manufacturability is required. The reactor contains three main components: reactor bed, condenser and heat exchanger. The heat exchanger design has been shown to be highly efficient as well as the underlying design philosophy [1]. However, an exact in depth evaluation of the condenser performance has not been performed yet. Furthermore, in light of reactor optimisation, an investigation on the reactor bed design for the use case of ZEF is seen as necessary.

The condenser plays a dual role in the reactor: it acts as the separation mechanism of products from the recycle stream and as vital factor in generating mass flow. Due to the current modelling architecture/philosophy of ZEF computationally simple descriptions of condensation phenomena are desired. A method based on linear relations for the latent heat release is developed. In combination with a PT-flash plug-in for MatLab this allows for modelling of heat effects and liquid-gas separation due to condensation. According to literature local heat transfer of condensation is significantly hampered compared to ideal Nusselt Film Condensation theory. The reason for this degradation is the presence of Non-Condensable Gasses which will limit the heat flux of the condensing species to the condenser surface. A sub model is used to evaluate whether this effect is significant. A combined model and experimental approach is used for evaluation of these models.

The reactor bed is the generation site of the methanol and in previous work it has been found there might be limiting effects in this bed [1]. Evaluation of literature on the causes indicates that mass transfer and temperature limitations are likely the cause. Furthermore literature suggests that the reactor bed might be able to attain a higher Space Time Yield. A set of models are made to describe the mass and heat transport of the reactor bed. These are based on 1-D heat transfer correlations, a linearized Thiele modulus, and the Bussche & Froment kinetic model. Furthermore, the reactor bed and condensation models are integrated into an existing overall model. This enables the simulation of synergy between these processes. A new reactor bed design is made based on these models which should increase the Space Time Yield, and is subject to experimental validation.

For the experimental validation a new reactor was designed and build based upon the new models developed. Characterisation experiments indicate satisfactory qualitative behaviour of the condensation modelling. Quantitatively deviations are observed which are expected to be due the over prediction of methanol formation by the reactor bed models. The reactor bed model deviations are mainly attributed to a lower than predicted mass flow rate, and adverse flow fields in the reactor bed. A new reactor bed design is proposed which should significantly reduce the adverse flow field effects while increasing thermal performance. The reactor bed design used allows for a decrease in catalyst size without causing a significant decrease in mass flow rate. An increase of a factor 1.25 for the Space Time Yield compared to the previous design has been observed during experiments. Insulation performance is satisfactory with the insulation performing within 20 W as modelled. Thermal efficiency has decreased by a factor 1.8 and is attributed to the under performance of the reactor bed.

Furthermore, the control of the reactor has been evaluated in terms of mass flow rate measurements,the prevention of the stalling of flow, and control. A new mass flow rate measurements device based on differential pressure, a new feed injection design, and further development of control have been experimentally validated. Designs for each of these subjects have been found to be satisfactory. Furthermore, it was found that reactor bed geometry also has an effect on the control of the reactor.

Contents

List of Figures

List of Tables

Nomenclature

Abbreviations

AEC	Alkaline EleCtrolysis
BASF	Badische Anilin- und SodaFabrik
BOP	Balance Of Plant
DAC	Direct Air Capture
DS	DiStillation
EOS	Equation Of State
FM	Fluid Machinery
GHSV	Gas Hourly Space Velocity
ICI	Imperial Chemical Industries
LED	Light Emitting Diode
MBR	Modified Brilman Reactor
MS	Methanol Synthesis
NCG	Non Condesable Gas(es)
PI	Proces Intensification
RDS	Rate Determining Step
STY	Space Time Yield
EOS	Equation Of State
(P)SRK	(Predictive) Soave-Redich-Kwong
VLE	Vapour Liquid Equilibrium
ODE	Ordinary Differential Equation
ZEF	Zero Emission Fuels
PT	Pressure Temperature
CNC	Computerised Numerical Control
PCB	Printed Circuit Board
COCO	CAPE-OPEN to CAPE-OPEN
(R)WGS	Reverse-Water-Gas-Shift
SS	Stainless Steel
SN	Stochiometric Number

symbols

C	Concentration	$\mathrm{mol\,m^{-3}}$
C_0	Surface or Baseline Concentration	$\mathrm{mol\,m^{-3}}$
C_i	Inlet Concentration	$\mathrm{mol\,m^{-3}}$
c^n	Reaction Concentration n-th order	$(\mathrm{mol\,m^{-3}})^n$
C_p	Heat Capacity	$\mathrm{J\,kg^{-1}\,k^{-1}}$
D_{eff}	Effective Diffusion Coefficient	$\mathrm{m^2\,s^{-1}}$
f	Fugacity	Bar
g	Gravimetric Constant	$\mathrm{kg\,m^{-1}\,s^{-2}}$
h_i	Heat Transfer Coefficeint	$\mathrm{W\,m^{-2}\,k^{-1}}$
Δh_v or $\Delta h'_{fg}$	Enthalpy of Vaporization	$\mathrm{kJ\,kg^{-1}}$
k_s	Rate Constant	$\mathrm{m^{-2}\,s^{-1}}$
k_i'',	Linearized Kinetic Constant	$\mathrm{s^{-1}}$
k	Thermal Conductivity	$\mathrm{W\,m^{-1}\,k^{-1}}$
$K_{eq,i}$	Pseudo Equilibrium Constant	-
KP_i°	Equilibrium Constant	-
K_{pi}°	Equilibrium Constant	-
K_p°	Controller Gain	-
Kf	Effective Fluid Flow Resistance	$\mathrm{g\,s^{-1}\,bar^{-1}}$
m_{cat}	Bulk Catalyst Mass	g
$\dot{m}$	Mass Flow Rate	$\mathrm{g\,s^{-1}}$
m''_{cond}	Condensate Mass Flux	$\mathrm{kg\,m^{-2}\,s^{-1}}$
n	Molls Present	mol
$\dot{Q}$	Heat	W
r_p	Radius Catalyst Pellet	m
r_i''' or r_i	Kinetic Rate	$\mathrm{mol\,m^{-3}\,s^{-1}}$
P	Pressure	Bar
P^{sat}	Saturation Pressure	Bar
PF	Poyniting Factor	$\mathrm{Bar^{-1}}$
RF	Radiative Forcing	$\mathrm{W\,m^{-2}}$
S_v	Specific Surface Area	$\mathrm{m^2}$
STY	Space Time Yield	$\mathrm{mmol\,g^{-1}\,h^{-1}}$
T	Temperature	°C
T_{avg}	Average Temperature	°C
T_s	Saturation Temperature	°C
T_0	Wall Temperature	°C
T_{dew}	Dew Temperature	°C
T_{mix}	Bulk Temperature	°C
u	Velocity	$\mathrm{m\,s^{-1}}$
v	Stichiometric coefficient	-
$\dot{V}$	volumetric Flow Rate	$\mathrm{m^3\,s^{-1}}$
v_r	Reaction Rate	$\mathrm{mol\,m^{-3}\,s^{-1}}$
$w_{v,}$	Mass Fraction	-
x	Distance/Position	m
x	Liquid Molar Fraction	-
X	Average Mass Fraction	-
y	Gas Molar Fraction	-
Y_i	Yield	mol

α	Reflection Coefficient	$\mathrm{W\,m^{-2}}$
α_i	Heat Transfer Coefficient	$\mathrm{W\,m^{-2}\,K^{-1}}$
δ	Condensate Layer Thickness	m
γ	Dimensionless Concentration	-
γ_i	Activity Coefficient	-
λ	Fluid Thermal Conductivity	$\mathrm{W\,m^{-1}\,k^{-1}}$
ρ	Density	$\mathrm{kg\,m^{-3}}$
μ	Dynamic Viscocity	$\mathrm{Pa\,s}$
η_{energy}	Energy Efficiency	%
η	Effectiveness Factor	-
η_{L}	Liquid Dynamic Viscosity	$\mathrm{Pa\,s}$
$\eta_{\mathrm{i}}^{\mathrm{e}}$	Linearized Effectiveness Factor	-
ϵ_{dr}	Dimensionless Radius	-
ϕ or ϕ_{m}	Thiele Modulus	-
ψ	Dimensionless Reaction Rate	-
τ	Residence Time	s

1 Introduction

One of the current subjects occupying public debate is the matter of climate change. Generally adjectives signifying danger are used such as crisis, emergency, existential threat etc. The underlying cause for the climate crisis is human action, and the sole option for negation of this crisis will be through humankinds efforts [2]. One of these efforts is the production of synthetic methanol and this thesis is made as part of this effort. Besides the background story this chapter will contain the research questions as well as a short description of the upcoming chapters.

1.1. CO_2 A measure of progression and regression

Since 1750 humankind has gone from horseback and candlelit rooms to steam trains and light bulbs, and to the current cars and LED. This progression can be subdivided in regions such as the industrial age, and can be seen as periods of increased industrialisation correlated with human development[3]. The main energy sources for industrialisation are fossil fuels, and with every increase of industrialisation more of this energy source is required as can be seen in figure 1.3.

When using fossil fuels one will have the release of, amongst others, the greenhouse gas CO_2 into the atmosphere. Especially the last 40 years a significant increase in concentration is observed as can be seen in figure 1.1 [2]. The correlation between figure 1.1 and 1.3 has been shown to be causal; the increased concentration of the greenhouse gas CO_2 is directly linked to the increased use of fossil fuels [2]. The term greenhouse gas indicates that the gas is able to increase the radiative forcing of the atmosphere [4]. The underlying reason being how the molecule is able to absorb and re-irradiate infrared energy[5].. As a consequence of this effect more energy of the sun is reflected back to earth instead of out into space. The resulting higher energy return is stored in various structures of the earth causing the average temperature to climb[5]. Generally the Beer-Lambert equation is accepted to describe this behaviour and is given as $\Delta RF = \alpha \ln(\frac{C}{C_0})$ [4] [6]. In this equation a base concentration is given C_0 vs the actual concentration C of gasses such as CO_2 in the environment. α describes the reflecting potential of CO_2, and is given by IPCC to be 5.22 indicating a significant potential of reflecting energy [6]. The unnerving aspect of this equation is its logarithmic nature: small concentration differences can have large effects. Luckily this also means that solutions which cause a small concentration decrease of greenhouse gasses can have big a impact.

The average temperature climb can thus be linked to the increase of the average CO_2 concentration which is closely linked to human activity. Nature deals with this increase by adopting its climate accordingly, however this is detrimental for many species living on earth including humans[2]. The list of harmful effects is plentiful but amongst them are: increased risk of flooding and wildfires, destruction of habitats, and reduced crop yields [2][7]. Images of the early appearances of these harmful effects are foreboding, such as figure 1.2 in which the disturbed water balance of a region can be seen. The earlier mentioned effects are those directly linked to climate change, while the indirect effects can be just as severe: such as war for access to water.

Minimising and ideally preventing these effects requires the planet to not warm up more than 1.5 degrees Celsius [2]. Therefore the amount of greenhouse gas emissions should be reduced to greatly reduce the radiative forcing [8] [9] [5].

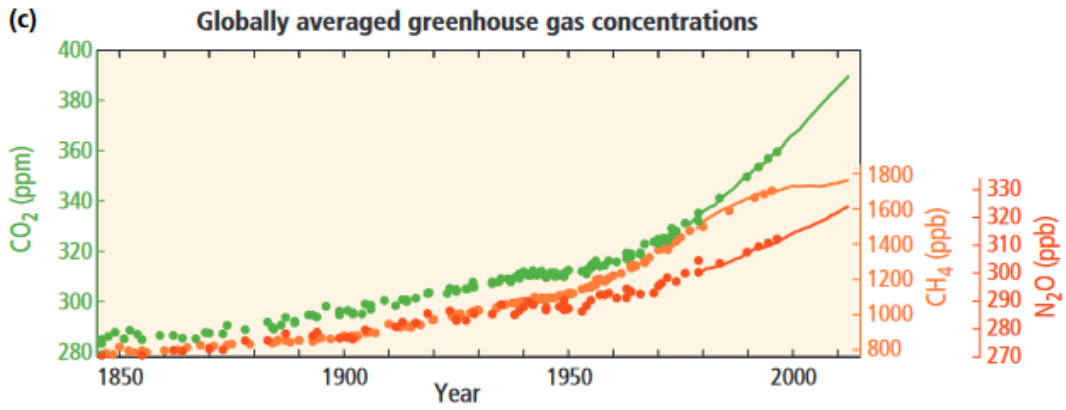

Figure 1.1: Concentration in the atmosphere of CO_2, N_2O and methane which are all greenhouse gasses. The significant increase since the start of the industrial age is apparent. Figure adapted from [2].

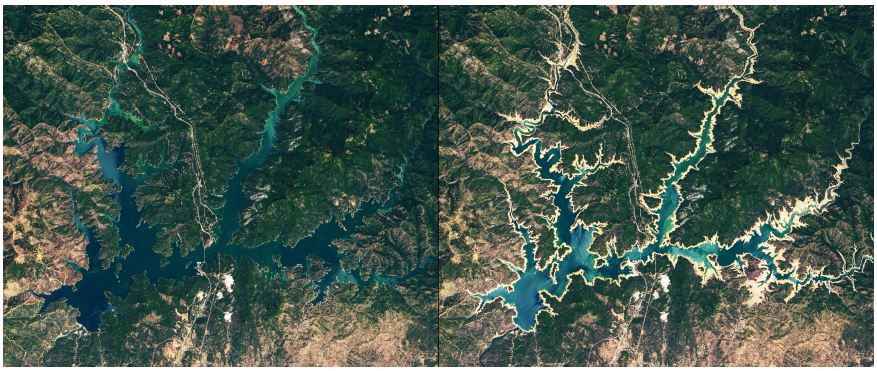

Figure 1.2: An example of the effects of climate change: in 2 years 40 % of the Shasta lake which is used as a water source has disappeared due to drought caused by climate change effects. Figure adapted from [10]

The current energy mix powering our world consists mainly of energy carriers which have a net positive CO_2 release as can be seen in figure 1.3 [11]. These carriers (oil, gas and coal) do hold advantages compared to the renewable energy sources already in the mix:

1. The energy density of fossil fuel sources such as oil are very high compared to batteries or hydrogen making them very effective energy carriers [12]. This aspect should not be taken lightly since most renewable energy sources produce hard to store electricity. Electric cars are already heavier and more short ranged than their oil fuelled counterparts, and no real electric option currently exists for aeroplanes.

2. Oil, gas and coal also function as important feedstocks for the production of many more complex molecules [13]. Hydrogen on itself cannot replace these feedstocks since it lacks the atoms carbon and oxygen. Although hydrogen will have a big role to play in the energy transition it cannot replace all aspects of the current fossil energy/feedstock mix.

The disadvantages of these fossil fuels/feedstocks are however of a very different order. The well known more visible examples of these disadvantages are pollution of the environment such as oil spills. However the main disadvantage is fossils direct link to the climate crisis. As indicated earlier the correlation between figure 1.1 and 1.3 has been shown to be causal [2]. Thus to mitigate the climate crisis the usage of fossils has to be significantly decreased. As indicated earlier most new energy sources have electricity as their output. The often resulting energy carrier hydrogen lacks the carbon atom fossils contain. This lacking of the carbon atom has implications for energy density, and usefulness in process/chemical industry. It can therefore be concluded that there is a need for renewable hydrocarbon sources as an energy carrier, and as feedstock for chemical industry.

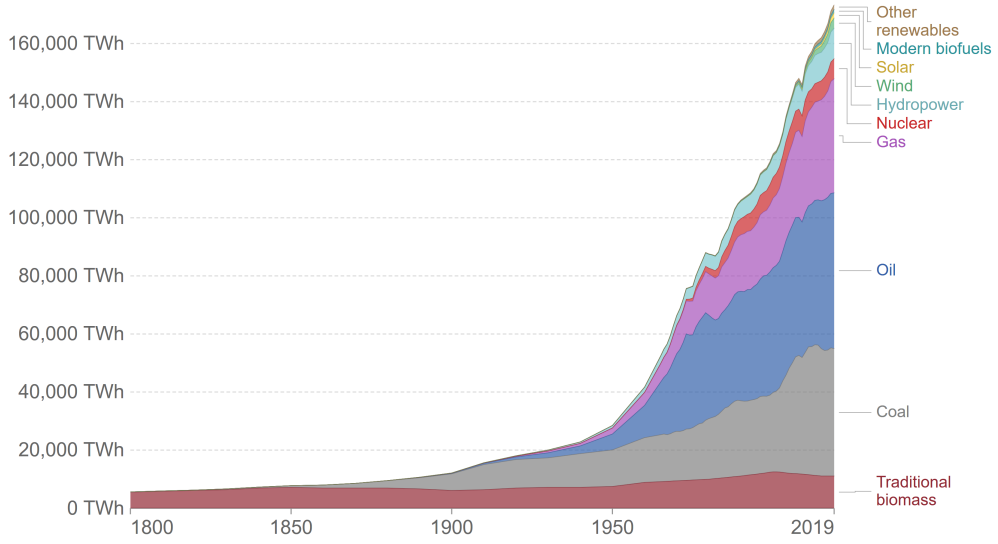

Figure 1.3: The historical trend of energy sources for humankind. The heavy use of fossil fuels can be observed aswell as the small amount of renewables in use. Figure adapted from [11].

1.2. Methanol: Inverting the root

One of the root causes of the climate issue at hand is thus CO_2, but it can also be one of the root methods for solving the issue. In combination with H_2 one can produce the shortest alcohol molecule CH_3OH also known as methanol [14]. Methanol appears at standard conditions as a liquid and furthermore contains a carbon atom [15]. Therefore it has a higher energy density per volume than compressed hydrogen, and can be transported easily due to its liquid state at ambient temperature and pressure [12]. Besides, methanol is able to function as a feedstock for chemical industry due to it containing hydrogen, carbon and oxygen atoms [16].

Methanol production in 2018 amounted to 110 million metric tons and demand for methanol has an average growth of 7 % per year [16]. Furthermore as indicated by figure 1.4 and other sources [16] [17] the potential uses for methanol are very diverse. These range from fuel for combustion engines (power-to-fuel) to the feedstock for many chemical processes, and from fuel for fuel-cells to an effective energy storage media [17]. With the upcoming energy transition one can easily see that the potential market for methanol is enormous. Effectively methanol is able to be the future sustainable carbon source for industry. Furthermore it can serve as an effective method for energy storage which is also easily transportable, and which can be used in already existing power systems [18].

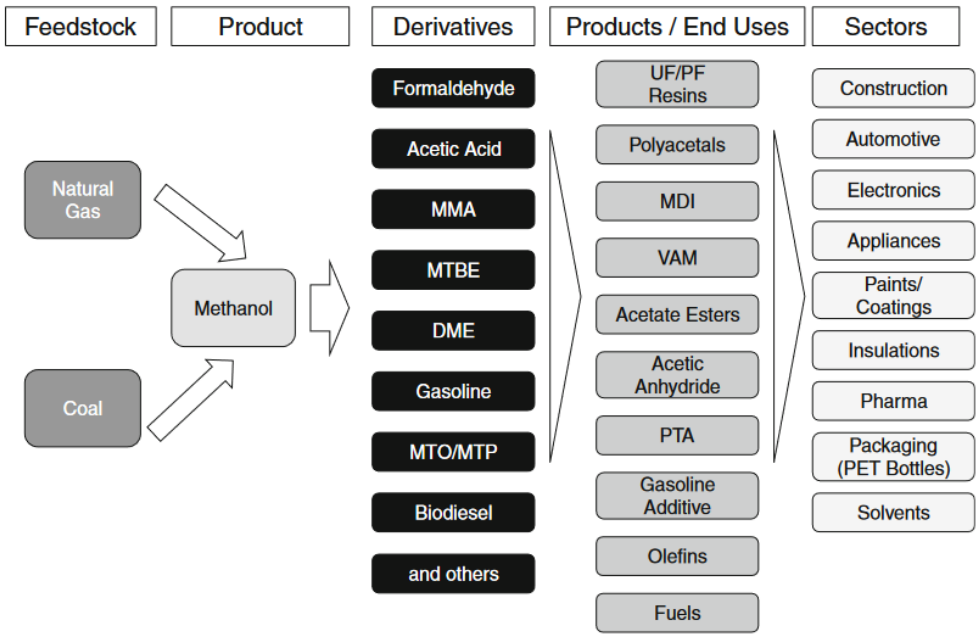

Figure 1.4: Methanol has a plethora of routes for synthesis and use as is apparent from this figure [19]. Note the feedstock section is not complete. Amongst the possible feedstocks not shown in this figure are those of ZEF which are CO_2 and H_2. Figure adapted from [19].

The chemical pathway towards methanol contains multiple routes, but all boil down to the following point: how to obtain the reactants for methanol?

$$CO_2 + 3H_2 \rightleftharpoons CH_3OH \tag{1.1}$$
$$CO + 2H_2 \rightleftharpoons CH_3OH \tag{1.2}$$

The reactants to produce methanol are hydrogen, and carbonmonoxide and/or carbondioxide (a mixture also known as syngas) [14][18]. These have to be sourced from either the atmosphere or derived from another feedstock. Generally industry uses steam reforming of natural gas but also sources from biomass and coal are used [18]. The frequently used methane steam reforming process contains multiple reactions amongst which are partial oxidation and the water-gas-shift. These can be summarised as follows [18]:

$$CH_4 + H_2O \rightleftharpoons CO + 3H_2 \tag{1.3}$$
$$CO_2 + 2H_2O \rightarrow CH_4 + O_2 \tag{1.4}$$
$$CO_2 + H_2 \rightleftharpoons CO + H_2O \tag{1.5}$$

These methods make use of natural gas which is a fossil fuel and therefore attribute to the climate crisis as set out above. Therefore either the source of methane (CH_4) needs to be renewable or a different source has to be sought. One of these renewable pathways is the usage of methods to capture atmospheric carbon-dioxide, and produce hydrogen from water using renewable energy sources [20]. In the case of this pathway methanol is generated through the following set of reactions [21]:

$$CO_2 + 3H_2 \rightleftharpoons CH_3OH + H_2O \tag{1.6}$$
$$CO_2 + H_2 \rightleftharpoons CO + H_2O \tag{1.7}$$
$$CO + 2H_2 \rightleftharpoons CH_3OH \tag{1.8}$$
$$\tag{1.9}$$

The nature of these reactions is highly exothermic (energy is released in the form of heat) and furthermore contains an equilibrium limit [21]. In chapter 2 an in depth review is given on the nature and modelling of these reactions. For now it suffices to say that the nature of these equilibria will have significant effect on methanol synthesis reactor design.

Renewable methanol production signifies a quantum shift: it allows industry to use a renewable carbon source instead of oil, it allows for long term energy storage, and simple transport for energy sources such as solar power. The underlying requirement to obtain renewable methanol is that the feedstocks of themselves are renewable. The major hurdle is cost since capturing CO_2 from air as well as electrolysis are expensive techniques [20]. Furthermore chemical plant design is a complex and time consuming endeavour. To surpass these hurdles a different approach then normally used by industry is required, and can be found in a company called ZEF [22].

1.3. ZEF: numbering up

One of the companies currently working on the production of renewable methanol is ZEF (Zero Emission Fuels) based in Delft, the Netherlands[22]. ZEF has opted to use the principle of numbering up to competitively produce methanol. Numbering up in this context means that many small methanol producing factories (called micro-plants) are used to achieve a significant methanol production volume. The approach of numbering up holds several advantages for ZEF compared to the typical scale-up approach currently used in process industry (make one single large device). The advantages of numbering up are (but not limited to): easy scaling to required demand, highly dynamic behaviour of a single device as well as the factory field, and low unit cost due to the principles of mass manufacturing. For example one has the option to switch of a section of a factory field when demand is lower. This very flexible behaviour towards operation is of vital importance due to the intermittency of the used renewable energy sources.

In the case of ZEF the current energy source to power the micro-plants will be solar power and due to its dynamic nature the microplant will be able to 'follow the sun' [22]. This is something conventional large scale reactors cannot due since start-up/shutdown cycles for large industrial process plants are in the order of days. Furthermore since the microplant is able to perform all its functions on electrical power it can be easily integrated with renewable energy sources. A significant advantage since process industry will have to use increasing amount of renewable (future) energy sources that predominantly have electricity as output [23]. Therefore one can see why a microplant coupled to renewable energy sources is a future-proof viable pathway for large scale methanol production.

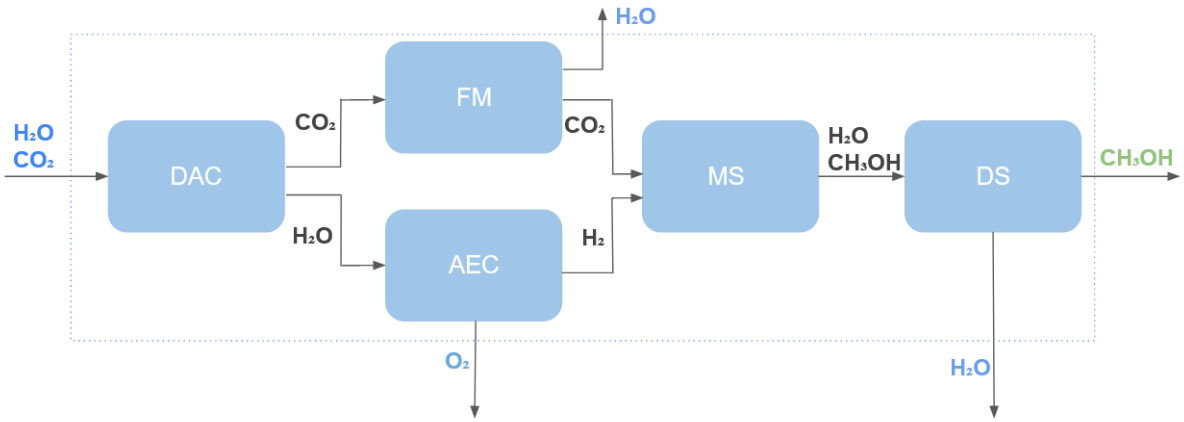

Figure 1.5: The general overview of the ZEF microplant and its subsystems. Plant border is the blue broken line, feed and waste streams are blue, and products are in green. All systems within the dotted line are powered by a renewable energy source such as solar power.

The ZEF microplant consists of several subsystems which together are able to generate methanol, and are powered by a form off renewable electricity such as solar power. The carbondioxide and water required are obtained from the air through an air capture unit using an amine flow exposed to the atmosphere. By using the principles of absorption and desorption the DAC (Direct Air Capture) subsystems captures CO_2 and H_2O and sends these feedstocks to FM and AEC respectively. FM (Fluid Machinery) dries and compresses the CO_2 to 50 bar for use in the methanol reactor subsystem known as MS (Methanol synthesis). This is accomplished by using an adsorption/desorption process in combination with a small compressor train. Simultaneously the AEC (Alkaline Electrolysis) system splits the captured water into its elemental parts by using an alkaline electrolyser. By operating the electrolysis system at a pressure of 50 bars and using a pump for water compression the costly exercise of hydrogen compression is circumvented. This results into the second required feed stream for the methanol reactor. MS uses a novel reactor design in which the products of water and methanol are condensed to circumvent the equilibrium limitations of methanol synthesis. The condensed products are then distilled in the DS (Distilation) system resulting in AA grade methanol.

Another unconventional aspect of ZEF is the method of product development and its workforce. Each 6 months ZEF starts a new iteration cycle in which a prototype/component of each subsystem is developed using the insights gained from the previous prototype and newly found theories at that point. Due to this approach ZEF can quickly develop and converge on successful designs of each subsystem. A further aspect is the structure of the workforce which consists of a core team with each member acting as lead engineer for a few of the subsystems. The main body of the workfoce (engineers) working on a certain subsystem consists exclusively out of students from all levels of ternary education, and from first internships up until master thesis's. A member of this section of the workforce will stay at ZEF for the duration of their study assignment which generally spans 1-2 ZEF iteration cycles. A symbiosis is established in which ZEF has a student workforce with the most up-to-date academic knowledge, while the student workforce has a chance to gain relevant experience working on cutting edge engineering systems.

1.4. This thesis

This thesis is made while being a member of the student workforce for the MS subsystem. In the past years the reactor has been developed from a concept developed by Brilman et al [14] to a highly energy integrated and efficient design [1]. The core principle of the reactor is that it makes use of natural convection in synergy with condensation of the products. By doing so the adverse methanol equilibrium otherwise encountered in methanol synthesis is bypassed [14]. The term synergy is used to signify that the heat sink required for the condensation to occur is also the reason natural convection takes place within the reactor. By employing heat exchange between this heat sink and the heat source (the reaction occurring) a high energy efficiency is reached [24]. This leads to a minimum of required heating power for the reactor bed to maintain methanol production [1]. In principle autothermal operation (the reaction providing all thermal energy required to keep the reaction going) is possible without the possibility of thermal runaway [1]. Due to the autothermicity the reactor will have a low energy requirement compared to other ZEF subsystems while keeping the numbering up benefits mentioned earlier. An in-depth review of the developmental work and principles of the reactor will be presented in chapter 2.

In this thesis an attempt is made to further develop the MS subsystem. The work will aim to increase the size of the reactor to fit half of the projected production requirements of the currently proposed ZEF micro-plant called 10X. The term 10X refers to the expected energy input of using 10 solar panels each rated at 300 W. From the overall BOP of the microplant this energy input gives a methanol yield of 285 g/h. Due to current safety concerns the sizing of the reactor for this work has been capped at an energy size of 5x giving a design yield of 142.5 grams of methanol an hour. Apart from this important design requirement, attention will be paid to the effects of condensation in the design using a combined modelling and experimental approach.

Furthermore research will be performed on the catalyst bed section of the reactor in terms of internal mass- and external heat transfer. Again use will be made of a combined modelling and experimental approach. Lastly attention will be paid to effects observed in the previous reactor design which mainly consists of unwanted drift and stalling (stopping of the natural convective flow). For these aspects mainly a design and experimental approach will be used.

1.4.1. Research lines

For this thesis the following three elements of the reactor are the main research focus: condensation of the produced methanol, packed bed, and operation/control.

Condensation is a vital element of the reactor since it allows for the circumvention of the equilibrium of the methanol synthesis reactions: the condensation drives the equilibrium in the reactor continuously towards methanol synthesis (an application of Chatelier's principles). It is known from previous work that the condensation mechanism has the desired effect [1]. However the exact mechanisms of the condensation and the consequences for the modelling/design are not fully known. In this thesis an investigation is made into the modelling and experimental characterisation of this condenser section, and the gathering of principles which can aid in further design and understanding of this condenser mechanism.

1. What is the effect of condensation on the temperature profile and lowest obtainable temperature of a natural convection methanol synthesis reactor designed to operate autothermally within ZEF's KPI's?

The ZEF's KPI's are thoroughly explained in chapter 3 of this work. For now it sufficient to state that amongst these are a required methanol yield of 142.5 g/h, and an optimised condenser in terms of heat duty and product separation performance.

Packed bed The packed bed of catalyst pellets is the generation site of the methanol and also the sole heat source for the reaction if autothermal operation is reached. Effectively a packed bed reactor in this case is nothing more than a tube packed with catalysts pellets through which the reactant gas flows. Due to the exothermic nature of the methanol synthesis reaction and the behaviour of the equilibrium ideally one would like to use an isothermal reactor design (the specifics are explained in chapter 2). Due to the numbering up strategy of ZEF advanced/complex reactor designs such as a shell and tube boiling water reactor (Lurgi reactor) are out of the question.

However by using Process Intensification principles within the reactor bed there could possibly be the potential to increase the reactor bed performance in terms of Space Time Yield. Therefore in this thesis an investigation is made into a method to passively increase Space Time Yield in the reactor while keeping mass-producability in mind.

To further understand the reactor bed also an investigation is made into the intra-particle diffusion of the catalytic pellets. Previous research at ZEF indicates that there are possible limitations due to some sort of mass transfer limitation [1]. Generally these are attributed to intra-particle diffusion limitations and therefore an investigation into these is warranted. By understanding these limitations one should be able to account for these in a design, and ideally also find methods to decrease/circumvent these limitations. For this thesis a modelling and indirect experimental study is performed to see if a) these limitations exist and b) their size and possible negation.

1. What is the significance of the intra-particle diffusion limitations and how can these be mitigated?
2. What packed bed reactor geometry/design is able to approach isothermal behaviour while maintaining a simple mass producible design?

Control is a required domain due to the highly dynamic behaviour of the reactor compared to conventional reactor designs. The reactor should be able to power-up, operate and shut-down everyday and perform all these aspects completely autonomously. To be able to do so control drift, flow stall (the stopping of circulation in the reactor due to the injection of cold gas), and knowledge on the mass flow rates in the reactor should be had. Combined with possible improvements for the dynamic behaviour implemented in the upcoming design the following questions can be posed:

1. What feed design is able to not let flow stall occur in the reactor?
2. What control method and/or design can prevent drift from occurring?
3. Which approach can be used to measure the mas flow rate in the reactor?

1.4.2. Structure of this work

Below the structure of this work is given and what information will be shown in each chapter. The general thought behind the structure is the standard scientific reporting structure: introduction/questions, theory, methods, results, conclusion/recommendations. The following chapters entail this work:

Chapter 1: Background information on the necessity of renewable energy sources, a possible candidate (methanol) and philosophy of production (ZEF). The research questions/objectives of this work are also introduced.

Chapter 2: Theory used in this work for a thorough understanding of the system, theoretical models which will be used for simulations, and potential reactor components which will serve as starting point for the new reactor design.

Chapter 3: Can be seen as the design section in which the development of the new reactor is detailed. The models used will be introduced, and the new reactor designed for experimental validation.

Chapter 4: In this chapter the experimental approach and its results, and the comparison with simulation results will be presented. In case of discrepancies between experimental results and expected/simulated behaviour the (expected) causes will be discussed.

Chapter 5: The results will be shortly stated and conclusions drawn. Furthermore recommendations will be made to improve models, experiments, reactor design, and anything which warrants improving compared to what is presented in this work.

Appendices: These will contain information which for some reason has not found a place within one of the above chapters, but requires inclusion in this work.

2

Literature review

In this review topics are discussed which are required for an understanding of the methanol synthesis reactor. Amongst these aspects is the historical context, and novel process intensification options for methanol synthesis. Also kinetic, equilibrium, and effectiveness models required for modelling of methanol synthesis are shown. Furthermore a review is made on the modelling of heat transport with an emphasis on condensation modelling due to the reliance of the reactor on this phenomena.

2.1. Methanol synthesis - basic principles

Methanol is a chemical which appears as a clear liquid at room temperature and standard atmospheric pressure. To obtain this product from the reactants used in the ZEF microplant (H_2 and CO_2) a set of chemical reactions are required. The reactions which occur when synthesising methanol from the named reactants are [25]:

$$CO_2 + 3H_2 \rightleftharpoons CH_3OH + H_2O \qquad \Delta H_r = -49.2 kJ/mol \tag{2.1}$$

$$CO + H_2 \rightleftharpoons CH_3OH \qquad \Delta H_r = -90.8 kJ/mol \tag{2.2}$$

$$CO_2 + H_2 \rightleftharpoons CO + H_2O \qquad \Delta H_r = 40.6 kJ/mol \tag{2.3}$$

The above equations show a few important characteristics of methanol synthesis:

1. Although only a feed of CO_2 is used due to the reaction (2.3) which is also known as the Water Gas Shift (WGS) CO will also be generated
2. The reactions involved for the generation of methanol are strongly exothermic indicating that heat management could be an important aspect of reactor design
3. The reactions are equilibrium reactions therefore thermal runaway is unlikely which has been proven by Vroegindeweij [1]
4. Due to the reactions being equilibrium reactions Le Chatelier's principle comes into play. This means the reactions can be influenced by changes in concentration, temperature, and pressure. But also inescapable limits are imposed for the generation of a certain chemical at a certain temperature, and pressure.

Le Chatellier's principle is a generally known concept in chemistry which dictates how a chemical equilibrium will react to external influences such as temperature, concentration, and pressure. It is usually introduced with sentences such as "*If a dynamic equilibrium is disturbed by changing the conditions, the position of equilibrium shifts to counteract the change to reestablish the equilibrium*" [26]. For example: the methanol synthesis reactions stated above show that the sum of products gives a lower amount of mols than reactants. As a consequence due to reaction the total pressure would decrease [26].

Therefore if the pressure is increased the equilibrium would react by trying to decrease the pressure, and therefore favour methanol synthesis. This tendency also extends to energy and since the reactions are exothermic a lowering of overall temperature would favour methanol synthesis [26]. Combining the above statements it can be seen why methanol synthesis is performed at moderate temperature and elevated pressure in industry.

Although one can give the equilibrium a tendency to favour the product side, one can never fully shift due to this balancing act to the product. Further down in the text this equilibrium will be quantified in the context of reaction modelling, but the takeaway of this qualitative discussion remains valid: methanol synthesis will always involve only partial synthesis due to chemical equilibrium, and this equilibrium will dictate significantly the chosen reactor conditions and possible yield.

2.2. Industrial methanol synthesis

Production at an industrial scale usually refers in the case of methanol to a volume in the order of tons/cubic meters. Two methods exist to reach this scale: scaling up and numbering up. First the method of scaling up (a single big reactor) is shown, since most historical and current methanol synthesis reactor designs are based on this principle. The other method of numbering up (many small reactors) is represented by the approach of ZEF. Since this thesis will be made in as part of reactor development for the use case of ZEF special attention will be paid on the methanol synthesis reactor history of ZEF.

2.2.1. History

Methanol is a natural occurring alcohol which can be found for example as a byproduct at very low concentrations during fermentation for wine production [15]. However it is not until some $\sim$ 175 years ago that methanol production has been attempted on an industrial scale [27]. The earliest methods (pre-industrial) made use of methods such as pyrolisis of wood giving a contaminated product or since 1661 (Robert Boyle) when including distillation to give a pure product [27][18]. Until 1834 (Jean-Baptiste Dumas and Eugene Peligot) the structure of methanol was unknown as was industrial scale production [27]. One of the major well known chemical process technologies form the start of the last century is the Haber-Bosch process for ammonia production. There is a large analogue between this and the start of effective industrial methanol production in time frame and methods[27]. The 26th of September 1923 at BASF saw the first process based on syngas (CO and $\mathrm{H_2}$) and using catalysts which were composed of zinc-chromite [27][21][18].

Figure 2.1: An example of a BASF high pressure reactor from the 1920's. Although it cannot be stated with certainty this specific one is a methanol or ammonia reactor they were highly alike. Figure adapted from [28].

The early industrial processes used high temperatures and pressures, and the sources of the syngas were feedstocks such as coals [27]. Due to the nature of this method of syngas generation contaminants were present in the syngas which would poison the catalyst [21]. Combining production methods giving cleaner syngas, and the finding that the best performing catalysts needed to contain copper and zinc oxides the high pressure methods could be changed for lower pressure options [27]. Between 1963 and 1966 ICI developed and built the so called low pressure plant which had an operating envelope of 30-120 bar and 200-300 °C [27]. This process has been shown to be much more efficient compared to high pressure designs, and has been the standard for methanol production plants ever since with facilities having daily yields of up to 10000 tons of methanol [27][21].

2.2.2. Current reactors

Amongst the designs of methanol reactors there are two dominant design philosophies and together these make up most of the built reactors. These are the adiabatic (quench) and isothermal reactor types as shown in figure 2.2 [29]. The limit imposed by the chemical equilibrium for methanol synthesis is relatively low and decreases in magnitude with increasing temperature and decreasing pressure [30]. The aim of these reactor designs is to have a controlled temperature profile which allows for an as high as possible equilibrium towards methanol synthesis. The ranges indicated for CO_2 feed gas methanol equilibrium conversion are 18-58 % for 200-250 °C and 50-100 bar [21]. ZEF's operational envelope will have the reactor run at 50 bar and therefore the equilibrium value can be expected to be low, and this has significant effect on reactor design. In order to maximise the per pass conversion the general idea used by industry is thus to control the temperature profile in the reactor since pressure can hardly be controlled (the reactor will run at a set pressure). The underlying idea is to keep the temperature as low as possible while maintaining adequate kinetics of the catalyst which gives the most advantageous chemical equilibrium for methanol synthesis as can be seen in figure 2.2 [29].

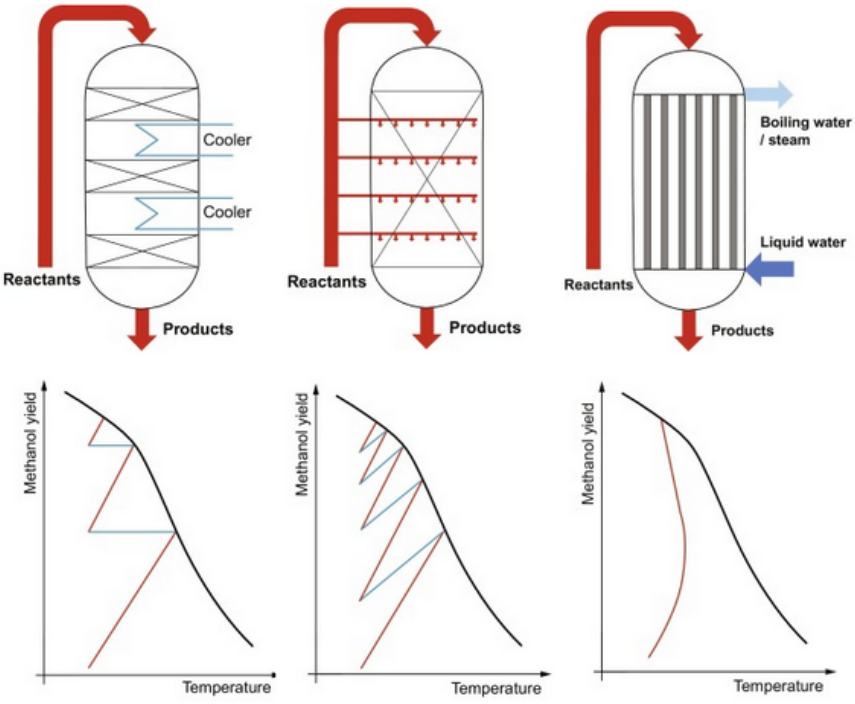

Figure 2.2: Examples of the two approaches in industrial methanol converters which aim to approach an optimal temperature in the reactor bed. The two left handside reactors are examples of quench based reactor systems, while the righthandside reactor is of the isothermal approach. Figure adapted from [29]

Generally when using the adiabatic approach the reactor bed is divided into multiple slices between which the species are cooled to increase distance to the equilibrium as can be seen in figure 2.2 [29]. The isothermal design takes this idea further and tries to keep the bed close to a constant temperature which is at a favourable position compared to the equilibrium [29]. Both approaches have positive and negative aspects: adiabatic reactors are generally cheaper but have a lower yield and less ideal temperature profile [29]. The isothermal reactors are much more complex and have a limited overall yield, but a much higher synthesis per pass [29].

Generally most reactors in use now follow the isothermal design philosophy as evident from figure 2.3. Most of these reactors also fall within the ZEF operational window either in terms of pressure, temperature or both [21]. It should be noted however that ZEF will not use a single reactor to achieve a yield of tons per day but rather uses a group of microplants (numbering-up strategy). Therefore a carbon copy of these reactors is not a justifiable approach. The complexity of these designs will not provide an economical business-case in terms of production and operation. However it does underline the need for a good understanding and control of the temperature profile of the reactor bed. Also the central design ideas behind these reactors still hold relevance as long as these can be adopted to the case of ZEF.

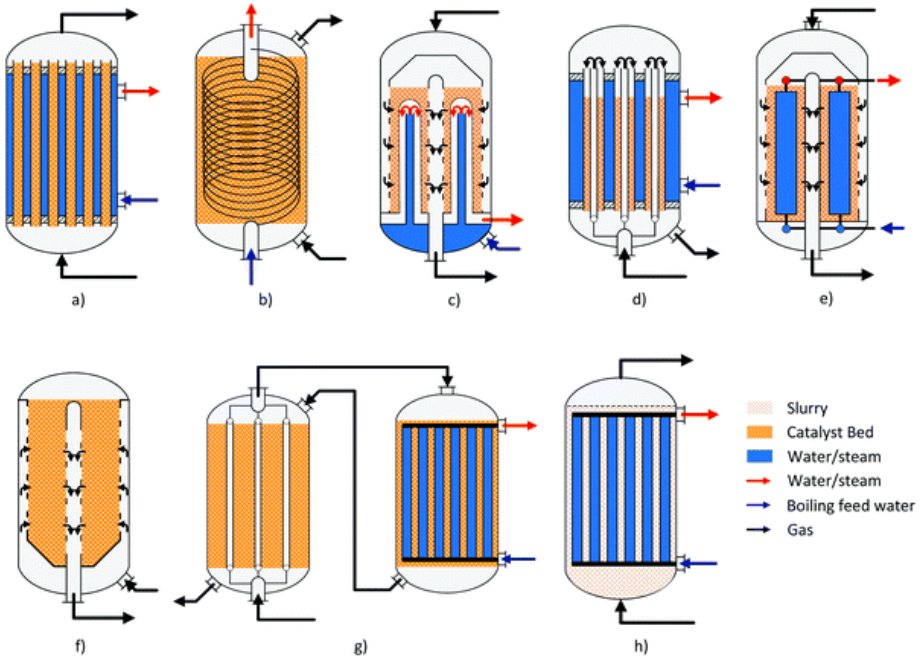

Figure 2.3: Current designs being operated and/or offered. Note the heavy use of the isothermal design philosophy and methods to control the temperature profile within the reactor. Reactors a, c-e and g-h make use of a heat transfer fluid, reactor b makes use of a cooling coil with gas, and reactor f uses a radial bed to have a degree of temperature control over the reactor bed. Figure adapted from [21]

2.3. ZEF's methanol synthesis reactor history

The history of methanol synthesis reactors at ZEF dates back to the start of the company. The initial muse for the reactor development is a reactor design proposed by the research group of Brilman [14].This muse and subsequent previous generation ZEF designs, and their major developments and discoveries are discussed.

2.3.1. Brilman reactor: ZEF's muse

Methanol synthesis at relative low pressure is significantly limited by the chemical equilibrium between products and reactants [31]. This limit is compounded if the temperature profile in the reactor bed is higher than necessary for reaction to sufficiently occur as indicated in the previous section. Brillman et al make use of the principle of condensation to bypass this equilibrium limitation [14]. By condensing the produced water and methanol the equilibrium will continuesly be shifted towards methanol synthesis in the reactor bed as per Le Chateliers principle. Due to the nature of the Vapour Liquid Equilibria (VLE) of methanol and water at 50 bar a low temperature section outside the packed bed section is required to enable the required condensation [14].

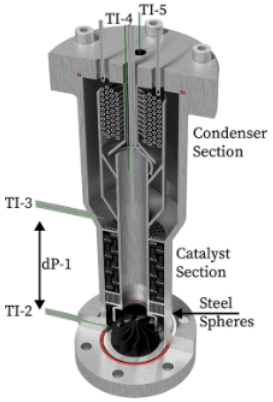

Figure 2.4: The reactor design used by Brilman et all. Note the relative height difference between reaction and condensation section to enable convective flow. Figure adapted from [31].

The Brilman reactor design achieves the required condensation by placing a set of water cooled pipes above the reactor bed. To prevent the relative cold condensation products from raining down on the reactor bed a fluid trap design is employed [14]. As can be seen in figure 2.4 the reactor is of an annular design. Roughly halfway the annulus the reactor bed is placed along with a heater to supply the required additional heat for attain reaction conditions [31]. The cooling coils are placed in the top of the reactor on the inside of the two pipes making up the annulus [14]. The condensing will take place directly on the cooling pipes. When the gravity force is larger than the surface tension of the condensate it will separate from the pipe surface, and fall into the collection basket directly below these pipes [31]. In this collection section a pipe is also placed to evacuate the condensate to prevent overflowing and thereby allow for semi-continuous operation [31].

The design is such that condensate is prevented from dripping on the reactor bed and the continuous condensation prevents chemical equilibrium from occurring in the reactor [14]. Furthermore by placing the hot reactor bed (the heat source) in the annulus and below the cooling pipes (the heat sink) which is placed on the inside of the two pipes a flow will occur due to natural convection. The density of the hot gasses will be lower than the density of the condensing gases/condensate. Since the volume of the reactor is fixed a pressure differential will occur inducing flow. The Brilman design incorporates a fan to boost this flow but it is not required to let this flow occur [14].

The exact performance values will be given at the end of this section. For now it is sufficient to state that the reactor shows proof of concept: methanol production under natural convective flow is possible with > 99 % carbon conversion [14]. It also shows the potential to run the reactor in autothermal mode (no external heat source required in steady state), but the design will need to incorporate a heat exchanger for that to be possible to occur [31].

2.3.2. Modified Brilman reactor - Basarkar

The Brilman design offers advantages which make it ideal for the use of a microplant design. Among these is the circumvention of chemical equilibrium at a relative low temperature and pressure, the use of natural convective flow removing the need of a pump, a very compact design, and product separation using solely condensation removing complex process equipment. Furthermore this reactor principle has the potential to operate in an autothermal mode therefore having a low overall energy demand [31]. Basarkar took the design as a muse and further developed this with an emphasis on heat integration to increase energy efficiency (named the Modified Brilman Reactor, MBR) [24]. This was also the first time ZEF designed, constructed and tested a methanol synthesis reactor, and it is therefore also a proof of concept in these aspects.

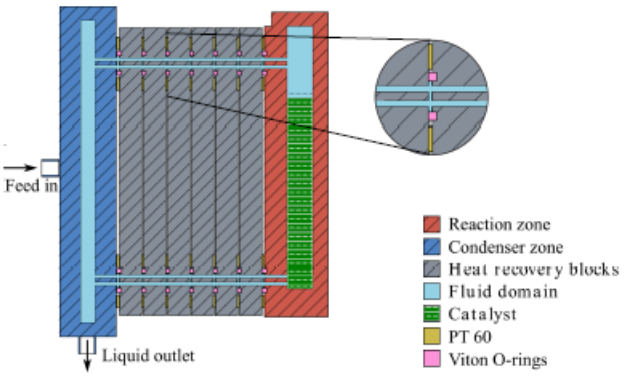

Figure 2.5: The Modified Brilman Reactor as developed. The basic returning sections of ZEF reactor design are apparent: condensation (blue), reaction (red) and heat integration (grey). Figure adapted from [24].

A circular loop design was created in which each vertical flowing column either housed the thermal source (the reactor bed) or the thermal sink (the condenser) [24]. The horizontal flowing sections are used for heat integration and are interconnected by aluminium blocks to facilitate the heat transfer by means of conduction [24] as can be seen in figure 2.5. The heat transfer blocks and reaction block are insulated with heaters placed at the reaction section to supply the required additional heat [24].

Experimental results indicated that the chosen route of thermal integration was a viable route [24]. Exact performance figures will be given at the end of this section, but the heat integration gave a great improvement in energy efficiency of the system [24]. Developmental points were also discovered: the reactor was heavy for its size ($\sim$ 5 kg) giving the reactor a slow dynamic response, the aluminium construction had corrosion issues with the methanol present, the insulation effectiveness should be increased, and improvements should be made on flow measurements and control [24].

2.3.3. Heat pipe based reactors - Van Laake & Mishra

The next iteration of the methanol synthesis reactor at ZEF was designed and developed by Van Laake [32]. This design was thoroughly investigated experimentally with improvements added by Mishra[33]. Van Laake kept the square loop design of Basarkar, but changed out the aluminium blocks for heat pipes as can be seen in figure 2.6[32]. Heat pipes are complex heat exchange structures which take advantages of condensation and evaporation mechanisms to enable much higher heat exchange than the conductive heat exchange of their shell material [32]. Van Laake furthermore placed fins within the heat exchange section connected to these heat pipes to further increase heat transfer. The overall construction was changed from aluminium blocks to Tri-Clamp SS304, and the first instance of automatic control is encountered. The control section takes on the shape of a block in which valves and a level sensor are placed which allows for continuous monitoring of the fluid levels in the system [32].

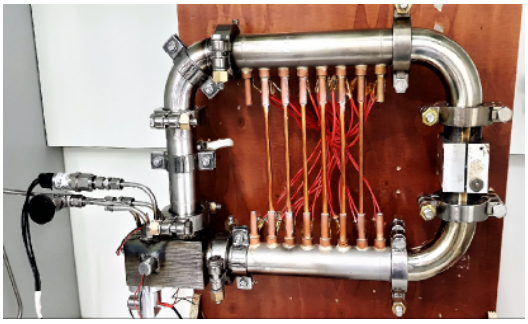

Figure 2.6: The Van Laake reactor. The reactor bed is on the right where the heater block is also placed, and the condenser is on the left side above the control block on the lower left. Insulation is not shown here but would cover everything except the condenser and control block. Figure adapted from [32].

The reactor performance showed improvement in heat exchange manifested experimentally in terms of significantly higher dynamic behaviour of the reactor. However the reactor suffered from a significantly higher mass flow rate than the reactor was designed for, and this adversely affected performance [32]. The main developmental points were to further increase the heat transfer with more heat pipes, distribute heat more evenly over the reactor bed, and get control on the mass flow rates in the system [32].

Mishra took the heat pipe based design further and doubled the number of heat pipes present on the system. Furthermore the block housing the valves was replaced with dedicated injection zones for each reactant which can be seen in figure 2.7 [33]. The amount of sensors was also significantly increased [33]. This allowed for a more in depth view of the behaviour of the reactor which was the primary aim of Mishra's research. Amongst these were the first inclusion of thermowells (temperature probes placed within the fluid stream) which allowed for accurate temperature measurements of the gas flow [33]. Further improvements made were the doubling of the amount of heat pipes, tweaking the thermal behaviour of the heat pipes, and the use of dedicated points for gas samples before and after the reactor bed [33].

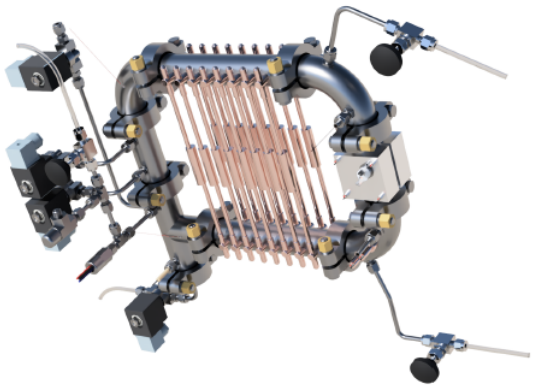

Figure 2.7: The reactor design of Mishra. The increased number and altered individual length of the heat tubes is evident. Furthermore the valve train on the left hand side makes used of a different valve system. The valves on the right side are for composition measurements over the reactor bed in between. Figure adapted from [33].

Mishra's experimental worked showed improvement in performance, and gathered significant experimental data on the dynamic performance of the system under different operational envelopes [33]. Furthermore the results indicated that the heat pipes were too fragile to be a viable heat integration method for the reactor. Developmental points on mass rate measurements, their control, as well as control of reactor heat, and feed composition remained despite more understanding having been developed [33].

2.3.4. New thermal design: Vroegindeweij

See Appendix D.

2.3.5. Historical performance

Evaluating the quantitative data for the latest reported values from the Brilman reactor and the reactors from ZEF one can see the significant development of energy integration [31] [24] [32] [33] [1]. The ZEF reactors show increasing performance in terms of energy efficiency while also maintaining production with increasing reactor size. Energy efficiency is evaluated as: the lower heating value of methanol divided by the higher heating value of hydrogen plus the total power consumption of the system. The STY shows a dip during the heat pipe era which is assumed to be due to the significantly higher mass flow rate decreasing overall effectiveness of the reactor bed [32][33].

Table 2.1: Reported performance values as found in and adopted from [1]. [1] lower bound reactor oven value [34]. The heat efficiency definition is given in chapter 4, and it is based on the amount of methanol produced vs amount of hydrogen injected and the heating power.

Performance value	Brilman [31]	Basarkar [24]	Van Laake [32]	Mishra [33]	Vroegindeweij [1]
m_{cat} [g]	52.2	45	120	120	460
STY [$mmolCH_3OH\,g_{cat}^{-1}h^{-1}$]	17	6.8	4.1	4.8	6.24
$T_{reactor\,wall}$ [°C]	317[1]	228	242	250	217
η_{energy} [%]	0	43.6	36.3	35.0	70.7

It should be noted that the Vroegindeweij reactor currently is subject of further optimisation studies within ZEF and the STY has further improved to a value of 6.96 $mmolCH_3OH/g_{cat} \cdot h$ [35]. The reported STY from Brilman might be possible although these values do differ from the best performing reactors in industry [21][31]. It is suspected that this value has been reached either by calculation errors, is caused by the reactor having a more advantageous temperature profile due to the radial bed design, or due to the internal fan. It should also be noted that the Brilman reactor has an internal fan to boost reactor performance causing possible further deviation between the ZEF and Brilman reactors [31]. Furthermore a decreasing condenser temperature can be seen as indicating higher product separation from the gas stream [14] [24] [32] [33] [1]. In conclusion an upward trend in reactor design/performance is shown indicating the current design is a good point to iterate forward from.

2.4. Catalysts

For the synthesis of methanol use is made of catalyst to enable synthesis at a temperature and pressure achievable within process equipment. Generally a catalyst allows for the reduction of the activation energies while not being consumed in the reaction taking place [36]. This effect can be seen well when reviewing the history of methanol synthesis (section 2.2.1), since one of the major driving factors for decreasing pressure and temperature were improved catalysts [27]. Generally methanol synthesis makes use of a catalyst containing copper and a mixture of the oxides of aluminium, and zinc or chromium[27]. Generally the most used catalyst blend is $Cu/ZnO/Al_2O_3$ with possible additives, and is used in the kinetic models and experiments used for this work [37]. There is ongoing scientific debate of the exact roles of each of the constituents of the catalyst, but general lines can be drawn. Copper is seen as the main active site, and the specific structure of the copper particles greatly determines the potency of the catalyst which is defined as structure sensitive reactions [38] [39]. ZnO is viewed as a supporter for the copper and scientific evidence suggest it has a role in dispersion of the copper sites [38]. Furthermore ZnO is able to decrease the poisoning by sulphur helping in increasing lifetime of the catalyst [21]. Al_2O_3 has been stated to be a promoter [38] and therefore helps in maximising catalytic activity. Overall the catalyst are known for their high selectivity towards methanol which is often stated to be over 99% [38] [21]. Catalysts are expected to generally operate for 4-6 years with thermal sintering being the primary cause for deactivation [21].

In practice to maintain the reactor yields at a certain level the temperature or pressure in the reactor is increased during the life of the catalyst [21]. Overall a catalyst is presented which as long as its not overheated or fed dirty gasses will perform with high selectivity for a significant amount of time. Furthermore the main constituents are not extremely rare or expensive metals giving a relative sustainable option compared to catalyst using more scarce materials.

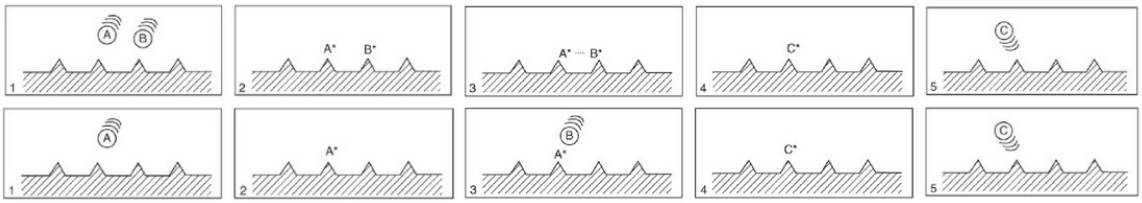

Figure 2.8: The Langmuir-Hinshwelwood mechanism (1-5 top) and the Eley-Rideal mechanism (1-5 below). The main difference is the moment in time in which reactant B adheres to the surface: before or during reaction to C. Figure adapted from [36]

In the case of methanol synthesis the catalyst can also be called a heterogeneous catalyst since the species are in gas phase while the catalyst is solid. Effectively this means that the reactant needs to have an interaction with the solid catalytic surface through a series of steps [36]. Knowledge of these steps is crucial since they provide information on how a catalyst will behave under certain conditions and provide a method to model the kinetics of the catalyst [36][40]. For methanol synthesis rate models usually either of two common adsorption models are used: the Langmuir-Hinshelwood or Eley-Rideal model [38]. Both models assume the interaction between two species, but the former model assumes reaction takes place with both species adsorbed to the surface. In the later model it is assumed that one species is adsorbed while the other species is not adsorbed to the surface as shown in figure 2.8 [38] [36]. The slowest reacting species adsorbing to the surface, and their respective products desorbing from the surface combined with the assumed mechanism will allow the identification of the rate determining step (RDS) [36]. This concept will make a significant return when evaluating the kinetic rate models in existence [40][25][41]. Furthermore when looking at what parameters affects these adsorption models one finds pressure an important parameter [36], and thus signifies the interplay between state parameters and overall reactor performance.

2.4.1. Pellet performance

Evaluating how well the catalyst in a reactor performs depends on a large number of diverse factors. Examples are variables such as temperature, pressure and flow velocities in the reactor, but also catalyst shape and mass transfer efficiency will affect the performance of the catalyst [36]. For this thesis the following parameters will be used to evaluate the effectiveness of the catalyst: mass flow rate, Space Time Yield and the effectiveness factor. The first and second parameter indicate the overall reactor performance while the the third indicates how well a single pellet performs. The effectiveness factor will be described more in depth in section 2.4.2 and 2.4.3, but generally it can be understood as how well a pellet allows conversion in the real vs ideal case. Factors such as selectivity are also great performance indicators, but since the catalyst all are based around the same $\mathrm{CuZnOAl_2O_3}$ and have similar high selectivity this will be of secondary importance.

The mass flow rate and Space Time Yield tell something about the flow rate in the reactor and how much each catalytic pellet is able to produce. The definition for STY and mass flow rate used in this work are [36]:

$$\dot{m} = uA\rho \tag{2.4}$$

$$\mathrm{STY} = \frac{\text{Desired product quantity}}{\text{Catalyst volume} \cdot \text{time}} \tag{2.5}$$

Especially the STY is reported across literature with a wide array of units especially the reporting units for the catalyst volume and product quantity [36]. An educative formula defining STY to note is the following [42]:

$$\mathrm{STY} = \frac{c_{k,in} Y_i}{\tau} \frac{v_i}{|v_k|} \tag{2.6}$$

In which $c_{k,in}$ is the molar concentration of a reactant into the reactor, Y_i the yield of the reactor, τ the residence time and v are the stochiometric coefficients (>0 for a product and 0< for a reactant). What this equations shows is the interplay between residence time and yield. Therefore if one would like to increase the STY one has to either decrease residence time while maintaining yield or increase yield for the same residence time, or a variant of these two extremes. The relevance of this concept in the research line for ZEF reactors is that it shows that just increasing mass flow rate while not increasing catalyst effectiveness will not increase performance. This is also a results Van Laake encountered in his work [32].

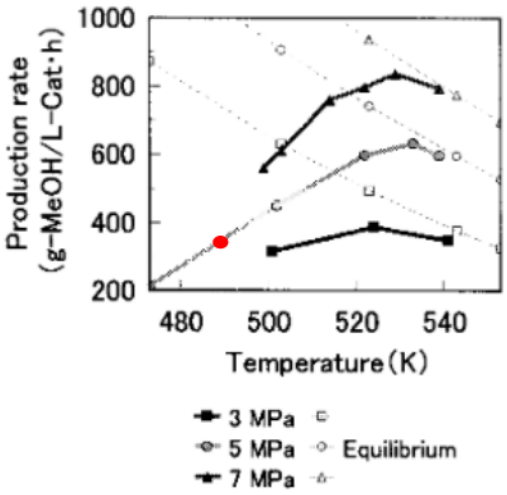

Figure 2.9: Reported STY's for a 50 kg/day CO_2 feed based methanol reactor within ZEF's operational envelope. The red dot represents the best STY achieved in the Vroegindeweij reactor at a pressure of 50 bar [1]. Note that the reactor of the source [43] is an isothermal design, and the reporting value for the Vroegindeweij reactor used here is the bed inlet temperature. What is evident from the figure is the great potential to increase STY with changing process parameters and/or reactor bed design. Figure adopted from [43]

Converting the reported values of the Vroegindeweij reactor [1], and assuming the volume of catalyst refers to the total reactor volume occupied by the reactor, one finds a best performance STY of 295 $g_{CH_3OH}/L \cdot hr$ or 0.295 $kg_{CH_3OH}/L \cdot hr$ or 9.19 $mol_{CH_3OH}/L \cdot hr$. The performance noted in literature are in the ranges of 200 - 650 $g_{CH_3OH}/L \cdot hr$ [43], 16-18 $mol_{CH_3OH}/L \cdot hr$ [44] and 0.4 - 0.8 $kg_{CH_3OH}/L \cdot hr$ [21]. The first two reported STY's are specifically for 50 bar and the temperature range of the ZEF reactor, and the last STY is a generally reported STY. As is evident from the figure 2.9 and the reported STY's there is a potential to improve the STY of the reactor. This would decrease the required catalyst for the reactor which decreases material usage (and thus cost). These STY's are generally reported for isothermal designs since as mentioned earlier this is the most used reactor design. It signifies again the effects of temperature distribution design on how well a reactor performs. Therefore significant attention will be paid on the performance of the reactor bed and its design.

2.4.2. Pellet effectiveness

From the previous reactor research it has come to light that there might be intra-particle diffusion limitations, and this is especially mentioned in the work of Vroegindeweij [1]. The simulations of COCO indicated a higher production than was actually achieved experimentally, and therefore some sort of

limitation within the reactor bed is suspected. The deviating effect observed was found during experiments with and without external fanned cooling of the condenser [1]. Therefore it is suspected that there are limitations of some sort preventing more production of methanol. Since the flow was increased in magnitude (external cooling of the condenser increased mass flow rate) one would expect the boundary layer thickness to decrease over the catalytic particles. This decreases the external mass transfer resistance towards the particle [45], and since this increase is possible this resistance is assumed to have negligible attribution to the observed limitation.

Looking at the surface of catalytic pellets one sees a porous landscape on which and within the catalytic active sites sit. This means reactants have to diffuse in and products out, and can be subject to so called internal or intra-particle resistance [45]. It should be noted that this resistance is next to the adsorption behaviour of heterogeneous catalysts and takes place before and or after the catalytic surface interactions [36]. In light of the previous paragraph it is expected that the resistance is due to this diffusive effect. It has been shown that $CuO/ZnO/Al_2O_3$ can have significant decrease in performance especially for low pressure methanol synthesis which is the envelope the ZEF reactor works in [46]. Literature gives values such as ranges of 32 % to 92 % of actual kinetic rates vs. what one can expect from kinetic law for low pressure methanol synthesis [38]. For quantification of these effects a wide array of possible models can be used. These range from relative simple models such as the Thiele concept to more complex models such as the Dusty-Gas model [38]. It has been found that the more simple Thiele modulus concept can be applied to quantify the effects without significant deviation from more complex models such as the Dusty Gas model [46][38].

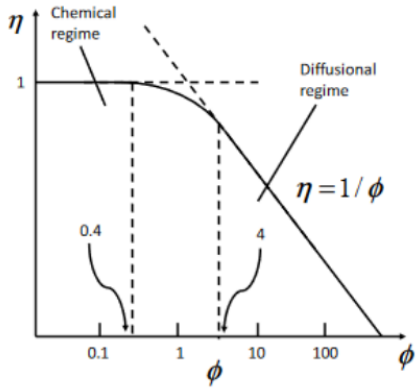

Figure 2.10: The general relation between the Thiele modulus η and effectiveness factor ϕ. One can see that with increasing modulus (large diffusion effects) the effectiveness of the reaction decreases. Ideally one would have a pellet which is on the left side of this graph. Figure adapted from [45]

2.4.3. Lommerts-Thiele Modulus

The Thiele Modulus is a concept which quantifies the effective reaction rate due to diffusion limitations versus the case these limitations do no occur as shown in figure 2.10 [45]. The Thiele modulus arises when putting the mass balance over a catalytic particle in a non dimensional form and can be shown to arise as follows [45]:

$$\frac{D_{eff}}{x^2}\frac{d}{dx}(x^2\frac{dc}{dx}) - S_v k_s c^n = 0 \tag{2.7}$$

$$\epsilon_{dr} = \frac{x}{r_p},\ \gamma = \frac{c}{c_s},\ \psi_r = \frac{v_r(c)}{v_r(c_s)},\ \phi = r_p\sqrt{\frac{S_V k_s c_s^{n-1}}{D_{eff}}} \tag{2.8}$$

$$\frac{1}{\epsilon_{dr}^2}\frac{d}{d\epsilon_{dr}}(\epsilon_{dr}^2\frac{\gamma_{dr}}{d\epsilon_{dr}}) = \phi^2\psi dr \tag{2.9}$$

In which D_{eff} is the effective molecular diffusitivity of the catalyst, x the radial position, c the concentration, c_s the surface concentration, S_v the specific surface area, k_s the kinetic constant, r_p the pellet radius, and the reaction rate is defined as $V_r = S_v k_s c^n$ [45]. The power of n in the concentration indicates the power of the reaction, and will play an important part in the upcoming Thiele modulus model. The Thiele modulus itself is ϕ and is effectively a dimensionless number indicating the relative size of the reaction versus diffusion due to catalytic pellet size [45]. The modulus can be coupled to the effectiveness factor allowing for a mathematical description of the mass transfer resistance which in case of a spherical particle and reaction order of n=1 gives [45]:

$$\eta = \frac{\int_0^{r_p} 4\pi x^2 v_r(c)dx}{\frac{4}{3}\pi r_{r_p}^3 v_r(c_s)} \tag{2.10}$$

$$\eta = \frac{3}{\phi}\left[\frac{1}{\tanh\phi} - \frac{1}{\phi}\right] \tag{2.11}$$

It should be noted that in cases of a reaction order different from 1 one has to resort to the use of numerical schemes [45] and this is likely why Lommerts et al, made use of a linearized Thiele modulus [46]. The core principles are the same but the expressions for certain parts of the Thiele modulus appear in different form in the Lommerts et al Thiele model description [46].

$$\phi_M = \frac{r_p}{3}\sqrt{\frac{k_i'''(K_{eq,i}+1)}{D_{mi}^e K_{eq,i}}} \tag{2.12}$$

$$\eta_i^e = \frac{1}{\phi_M}\left(\frac{(3\phi_M)\coth(3\phi_M) - 1}{3\phi_M}\right) \tag{2.13}$$

In which η_i^e relates to the effectiveness factor of a specific reaction, k_i'''' the fitted kinetic constant and $K_{eq,i}$ the equilibrium constant of a specific species. The core idea of their approach is to use first order kinetic relations, equations of the form $r_i = k_i \cdot c_i$, with a fitting factor fitted to the Graaf kinetic model at the required temperature and pressure [46]. Due to this approach the reaction rates remain first order and the analytical approach can be used. The used linearised kinetics are[46]:

$$r'''_{CH_3OH} = k'''_{CH_3OH}(c_{H_2} - c_{CH_3OH}/K_{eqCH_3OH}) \tag{2.14}$$

$$r'''_{H_2O} = k'''_{H_2O}(c_{H_2} - c_{H_2O}/K_{eqH_2O}) \tag{2.15}$$

The indicated equilibrium constants are referred to by Lommerts et al as pseudo-constants since these are also evaluated at the given temperature and pressure and therefore technically cannot be seen as a constant [46]. These are defined as [46]:

$$K_{eqCH_3OH} = \left(\frac{c_{CH_3OH}}{c_{H_2}}\right)_{eq} \tag{2.16}$$

$$K_{eqH_2O} = \left(\frac{c_{H_2O}}{c_{H_2}}\right)_{eq} \tag{2.17}$$

With this model it is possible to find and quantify the size of mass transfer resistance for the reactor bed in combination with a kinetic and convective (species transporting) model. Furthermore it has an applicable range of pressures and temperature of up to 140 bar and 540 K respectively which is well within the ZEF operational window [46]. By understanding the mass transfer resistance one should be able to a) design the reactor in such a way to minimise its effect, and b) have a clearer image of the to be expected performance of the reactor (ideally improving the STY).

2.5. Kinetics & equilibrium

It is crucial for reactor development to know how much methanol is produced and under what conditions. Furthermore understanding of the heat released due to exothermic reactions plays a significant part in the thermal design of the natural convection reactor. Therefore models are required that predict when reactions occur and to which extent. To this end use is made of kinetic rate and equilibrium composition models. The rate equations will indicate at what rate the reactions reach chemical equilibrium at a set inlet composition. The chemical equilibrium is the hard limit at which point all reactions are in equilibrium at a certain temperature and pressure.

2.5.1. Equilibrium composition

The reaction rate equations used take into account the equilibrium limitation through a sub-model [40] [41] [25]. Kinetic models will use this type of model to show to which extent a reaction will take place at a given state and concentration of species. In the case of the ZEF reactor design generally the equilibrium composition is desired to occur at the end of the reactor bed giving optimal bed usage [1]. Furthermore having an equilibrium model allows for understanding of how reaction kinetics can be limited by adverse temperature profiles in the reactor bed.

Therefore a model for this equilibrium is required and is found in the form of the equilibrium by Graaf and Winkellman which is valid for a temperature range of 472-1273 K, and makes use of the Soave-Redlich-Kwong EOS [30]. The model is based on a large amount of experimental data and is therefore seen as very accurate according to the authors [30]. The model is stated as [30]:

$$CO_2 + 2H_2 \rightleftharpoons CH_3OH \tag{2.18}$$

$$\begin{aligned}\ln KP_1^\circ(T) = \frac{1}{RT}(&7.44140 \cdot 10^4 + 1.89260 \cdot 10^2 T + 3.2443 \cdot 10^{-2} T^2 + 7.0342 \cdot 10^{-6} T^3 \\ &-5.6053 \cdot 10^{-9} T^4 + 1.0344 \cdot 10^{-12} T^5 - 6.4364 \cdot 10^1 \, T \ln T)\end{aligned} \tag{2.19}$$

$$CO_2 + H_2 \rightleftharpoons CO + H_2O \tag{2.20}$$

$$\begin{aligned}\ln KP_2^\circ(T) = \frac{1}{RT}(&-3.94121 \cdot 10^4 - 5.41516 \cdot 10^1 T - 5.5642 \cdot 10^{-2} T^2 + 2.5760 \cdot 10^{-5} T^3 \\ &-7.6594 \cdot 10^{-9} T^4 + 1.0161 \cdot 10^{-12} T^5 + 1.8429 \cdot 10^1 \, T \ln T)\end{aligned} \tag{2.21}$$

This specific model can be found in the Slotboom kinetic model mentioned in section 2.5.2. An older equilibrium also developed by Graaf [47] is used in the Graaf and the Van den Bussche models discussed. It is of a simpler nature, but gives similar results as the Graaf & Winkelman model[47]:

$$\log_{10} K_{p1}^\circ = \frac{5139}{T} - 12.621 \tag{2.22}$$

$$\log_{10} K_{p2}^\circ = \frac{-2073}{T} - 2.029 \tag{2.23}$$

It should further be noted that although two equilibrium relations are given there are three reactions, but due to the of the degrees of freedom in the system only two equilibria are required [30].

2.5.2. Rate equations

For the kinetic rate equations of methanol synthesis a plethora of models exists. These models represent many possible reaction conditions as well as possible reaction routes [25]. Generally in literature two models are named often and represent the two mostly used reaction pathways:

- Assuming a direct CO route to methanol by Van Der Graaf et al [40]. With a direct route it is meant that there is a reaction equation in which CO is a reactant and methanol a product.
- Assuming an indirect contribution of CO to the formation of methanol by Van Den Bussche and Froment [41]. Generally CO is formed by the reverse water gas shift (RWGS), and no pathway to methanol is assumed.

This immediately shows an ongoing debate in the world of methanol synthesis: what role do CO and CO_2 play in methanol synthesis? Initially when kinetic models where being developed for methanol synthesis it was assumed to start from CO [38] [25]. Later only CO_2 was assumed to be the source, and also a combination of these were assumed [25].

In the previous decades multiple methods have been used to find which reactant is the actual source in methanol synthesis. This ranges from statistical analysis of reaction rates under different feed conditions to using radioactively marked carbon atoms [38]. Nonetheless the discussion has not yet been definitively been settled, and new models based on the different pathways keep being proposed.

To set-up a kinetic model one can make use of the earlier mentioned adsorption models which models how a certain a molecule adheres to the catalytic surface [36]. Using a proposed pathway of intermediates between the reactant and products one seeks the rate determining step (RDS) [40]. Using this information kinetic rate equations are set-up and fitted to experimental data [40]. Although nowadays models are also developed based on micro-kinetic calculations which are able to view all reaction steps as rate determining [25][48]. For this work the Van Den Bussche and Froment work will be mainly used. It is the model historically used by ZEF, and therefore has to possibility for validation between this and previous works. The works of Graaf et al and Slotboom et al are included to show the different models in existence. The Graaf et al model is very dominant in literature and is a relatively old. The Slotboom et al model is relatively young and represents the new models being based on thorough statistical analysis and new insights.

Graaf et al

In 1988 Graaf et al published a kinetic model which has been frequently used since, and it is one of the best known for the modelling of low pressure methanol synthesis models [40] [38]. The model makes use of the assumption that the catalytic adsorption behaviour follows the Langmuir-Hinshelwood model with dual sites [40]. On the first site (s1) a competition adherence between CO and $\mathrm{CO_2}$ is assumed while on the other site (s2) a competition adherence of $\mathrm{H_2}$ and $\mathrm{H_2O}$ is assumed [40]. Therefore it is assumed both CO and $\mathrm{CO_2}$ partake in the generation of methanol [40]. This gives rise to the following set of adsorption equilibria and possible intermediate RDS [40]:

Adsorption equilibrium

$$\mathrm{CO + s1 \rightleftharpoons COs1}$$
$$\mathrm{CO_2 + s1 \rightleftharpoons CO_2s1}$$
$$\mathrm{H_2 + 2s2 \rightleftharpoons 2H_s s2}$$
$$\mathrm{H_2O + s2 \rightleftharpoons H_2Os2}$$

RDS & driving force group

$\mathrm{COs1 + s2H \rightleftharpoons HCOs1 + s2}$	$f_{CO}f_{H_2}^2 - f_{CH_3OH}/(f_{H_2}^{3/2}K^\circ_{P_1})$	A(1)
$\mathrm{HCOs1 + s2H \rightleftharpoons H_2COs1 + s2}$	$f_{CO}f_{H_2} - f_{CH_3OH}/(f_{H_2}K^\circ_{P_1})$	A(2)
$\mathrm{H_2COs1 + s2H \rightleftharpoons H_3COs1 + s2}$	$f_{CO}f_{H_2}^{3/2} - f_{CH_3OH}/(f_{H_2}^{1/2}K^\circ_{P_1})$	A(3)
$\mathrm{H_3COs1 + s2H \rightleftharpoons CH_3OH + s1 + s2}$	$f_{CO}f_{H_2}^2 - f_{CH_3OH}/K^\circ_{P_1}$	A(4)
$\mathrm{CO_2s1 + Hs2 \rightleftharpoons HCO_2s1 + s2}$	$f_{CO}f_{H_2}^{1/2} - f_{CO}f_{H_2O}/(f_{H_2}^{1/2}K^\circ_{P_2})$	B(1)
$\mathrm{HCO_2s1 + Hs1 \rightleftharpoons COs1 + H_2Os2}$	$f_{CO}f_{H_2} - f_{CO}f_{H_2O}/K^\circ_{P_2}$	B(2)
$\mathrm{CO_2s1 + Hs1 \rightleftharpoons HCO_2s1 + s2}$	$f_{CO_2}f_{H_2}^{1/2} - f_{CH_3OH}f_{H_2O}/(f_{H_2}^{5/2}K^\circ_{P_3})$	C(1)
$\mathrm{HCO_2s1 + Hs2 \rightleftharpoons HCO_2s1 + s2}$	$f_{CO_2}f_{H_2} - f_{CH_3OH}f_{H_2O}/(f_{H_2}^2K^\circ_{P_3})$	C(2)
$\mathrm{H_2CO_2s1 + Hs2 \rightleftharpoons H_3CO_2s1 + s2}$	$f_{CO_2}f_{H_2}^{3/2} - f_{CH_3OH}f_{H_2O}/(f_{H_2}^{3/2}K^\circ_{P_3})$	C(3)
$\mathrm{H_2CO_2s1 + Hs2 \rightleftharpoons H_2COs1 + H_2Os2}$	$f_{CO_2}f_{H_2}^2 - f_{CH_3OH}f_{H_2O}/(f_{H_2}K^\circ_{P_3})$	C(4)
$\mathrm{H_2COs1 + Hs2 \rightleftharpoons H_3COs1 + s2}$	$f_{CO_2}f_{H_2}^{5/2}/f_{H_2O} - f_{CH_3OH}f_{H_2O}/(f_{H_2}^{1/2}K^\circ_{P_3})$	C(5)
$\mathrm{H_3COs1 + Hs2 \rightleftharpoons CH_3OH + s1 + s2}$	$f_{CO_2}f_{H_2}^3/f_{H_2O} - f_{CH_3OH}f_{H_2O}/(f_{H_2}^{1/2}K^\circ_{P_3})$	C(6)

In which f are the fugacities of the species, K°_{pi} the chemical equilibria and, s the active sites to which the species adhere [40]. By assuming that one of each group (A,B and C) are a RDS a group of rate equations is generated, and other equations are at that time not limiting [40]. Graaf et al then performed a set of experiments with feeds of different CO, CO_2, H_2 compositions with a pressure set of 15, 30 and 50 bars temperature set of 483.5, 499.3 and 516.7 for most experiments and a volumetric gas flow range of 1-6 $m^3s^{-1}kg^{-1}$[40]. The reactor was a spinning basket reactor in which Haldor Topsoe MK 101 catalyst was used, and care was taken to prevent inclusion of data containing possible mass transfer limitations[40]. Following experimental fitting the model containing the RDS's A3B2C3 were found to be the best fit to experimental data. This gives the following rate equations [40]:

$$r_{CH_3OH,A3} = \frac{K'_{ps,A3}K_{CO}[f_{CO}f_{H_2}^{3/2} - f_{CH_3OH}/(f_{H_2}^{1/2}K^\circ_{P_1})]}{(1 + K_{CO}f_{CO} + K_{CO_2}f_{CO_2}[f_{H_2}^{1/2} + (K_{H_2O}/K_{H_2}^{1/2})fH_2O])} \tag{2.24}$$

$$r_{H_2O,B2} = \frac{K'_{ps,B2}K_{CO_2}[f_{CO}f_{H_2} - f_{H_2O}f_{CO}/K^\circ_{P_2})]}{(1 + K_{CO}f_{CO} + K_{CO_2}f_{CO_2}[f_{H_2}^{1/2} + (K_{H_2O}/K_{H_2}^{1/2})fH_2O])} \tag{2.25}$$

$$r_{CH_3OH,C3} = \frac{K'_{ps,C3}K_{CO_2}[f_{CO}f_{H_2}^{3/2} - f_{CH_3OH}/(f_{H_2}^{3/2}K^\circ_{P_3})]}{(1 + K_{CO}f_{CO} + K_{CO_2}f_{CO_2}[f_{H_2}^{1/2} + (K_{H_2O}/K_{H_2}^{1/2})fH_2O])} \tag{2.26}$$

In which the fitted parameters are defined as follows:

$$K'_{ps,A3} = (2.69 \pm 0.14) \cdot 10^{7} \cdot \exp(\frac{-109900 \pm 200}{RT}) \quad (2.27)$$

$$K'_{ps,B2} = (7.31 \pm 4.90) \cdot 10^{8} \cdot \exp(\frac{-123400 \pm 1600}{RT}) \quad (2.28)$$

$$K'_{ps,C3} = (4.36 \pm 0.25) \cdot 10^{2} \cdot \exp(\frac{-65200 \pm 200}{RT}) \quad (2.29)$$

$$K_{CO} = (7.99 \pm 1.28) \cdot 10^{-7} \cdot \exp(\frac{-58100 \pm 600}{RT}) \quad (2.30)$$

$$K_{CO_2} = (1.02 \pm 0.16) \cdot 10^{-7} \cdot \exp(\frac{67400 \pm 600}{RT}) \quad (2.31)$$

$$K_{H_2O}/K_{H_2}^{1/2} = (4.13 \pm 1.51) \cdot 10^{-11} \cdot \exp(\frac{104500 \pm 1100}{RT}) \quad (2.32)$$

(2.33)

An often noted critique of the model is that the intermediaries such as those in RDS A(3) and C(5) are duplicated in the model [25] [38]. This is not physical due to it allowing for different concentration for the same intermediary within the model [38]. Still the model has good performance within its experimental data set and is frequently used in literature [25] [38]. In the case of this thesis it will mainly be used for linking/comparison of the Busche and Froment kinetics to intra-particle diffusion limitation models which are based on the Graaf model.

Van den Bussche & Froment

In 1996 the model was published which next to the model of Graaf et al is used often in works on methanol synthesis [38] [41]. This model developed by Van den Bussche & Froment takes a different view on the reaction mechanisms towards methanol [41]. Based on previous work of other authors it is assumed CO_2 is the main reactant for methanol synthesis [41]. Furthermore the RDS are predetermined based on the available literature at that time rather than statistical analysis afterwards as in the case of Van der Graaf et al [41]. The postulated pathway of reactions is [41]:

Reaction	Adsorption constant	Notes
$H_2(g) + 2s \rightleftharpoons 2H.s$	K_{H2}	
$CO_2(g) + s \rightleftharpoons O.s + CO(g)$	k_1, K_1	RDS
$CO_g + O.s + s \rightleftharpoons CO_3.2s$	K_2	
$CO_3.2s + H.s \rightleftharpoons HCO_3.2s + s$	K_3	
$HCO_3.2s + s \rightleftharpoons HCO_2.2s + O.s$	K_4	
$HCO_2.2s + H.s \rightleftharpoons H_2CO_2.2s + s$	K_{5a}	RDS
$H_2CO_2.2s \rightleftharpoons H_2CO.s + O.s$	K_{5b}	
$H_2CO.s + H.s \rightleftharpoons H_3CO.s + s$	K_6	
$H_3CO.s + H.s \rightleftharpoons CH_3OH(g) + 2s$	K_7	
$O.s + H.s \rightleftharpoons OH.s + s$	K_8	
$OH.s + H.s \rightleftharpoons H_2O.s + s$	K_9	
$H_2O.s \rightleftharpoons H_2O(g) + s$	K_{H_2O}	

Following this a set of kinetics for the overall reaction rates were established, and the found combination of K-factors are assumed to be of an Arrhenhius or Van't Hoff type frequency factors [41]. Note that the factors K^* and k_3^* are the equilibrium constants, and are taken from the Graaf model which are stated earlier in this chapter.

$$r_{meoh} = \frac{k'_{5a} K'_2 K_3 K_4 K_{H_2} p_{CO_2} [1 - (1/K^*)(p_{H_2O} p_{CH_3OH} / p^3_{H_2} P_{CO_2})]}{(1 + (K_{H_2O}/K_8 K_9 K_{H_2})(p_{H_2}O/p_{H_2}) + \sqrt{K_{H_2} p_{H_2}} + K_{H_2O} p_{H_2O})^3} \tag{2.34}$$

$$r_{RWGS} = \frac{k'_1 p_{CO_2} [1 - K^*_3 (p_{H_2O} p_{CO} / p_{CO_2} p_{H_2})]}{(1 + (K_{H_2O}/K_8 K_9 K_{H_2})(p_{H_2}O/p_{H_2}) + \sqrt{K_{H_2} p_{H_2}} + K_{H_2O} p_{H_2O})^3} \tag{2.35}$$

$$K(i) = A^*(i) \exp(-\frac{B(i)}{R}(\frac{1}{T_{av}} - \frac{1}{T})) \tag{2.36}$$

The fitting values for A and B for the lumped frequency K factors where found using experimental data [41]. This data was generated by Van den Bussche and Froment using a thin tubular reactor with ground ICI 51-2 catalyst [41]. By grounding and diluting the pellets with inert components it was assured that mass transfer limitations would not interfere with experimental data [41]. The experiments were performed for temperatures between 180-280 °C, pressures of 15-51 bar and P_{CO}/P_{CO_2} ratio 0-4.1 with the total experimental set of 276 [41]. Based on the fitting results the following values are found [41]:

Table 2.2: The fitted parameters, their values and standard deviation as reported by [41].

Group	Numeric value	Standard deviation
$\sqrt{K_{H_2}}, A^*$	30.82	0.375
$\sqrt{K_{H_2}}, B$	17197	1864
K_{H_2O}, A^*	558.17	10.18
K_{H_2O}, B	124119	3058
$\frac{K_{H_2O}}{K_8 K_9 K_{H_2}}, A^*$	3453.38	260.29
$\frac{K_{H_2O}}{K_8 K_9 K_{H_2}}, B$	0	0
$k'_{5a} K'_2 K_3 K_4 K_{H_2}, A^*$	7070.34	259.75
$k'_{5a} K'_2 K_3 K_4 K_{H_2}, B$	36696	6102.8
k'_1, A^*	1.65	0.02
k'_1, B	-94765	1694

The model performs well within its experimental data set, and also fits the experimental conditions for ZEF [41]. Van den Bussche and Froment further state that since the model is based on a mechanistically system, which is physically sound, the model can be used with accuracy outside its experimental training set [41]. From the point of ZEF this model has been historically used for the reactor design [24][32][33][1]. This is due to it fitting the experimental conditions of ZEF, its mechanistically sound nature, and its often use in literature indicating high confidence in the model. For this work the model of Van den Bussche and Froment will also be used as the standard model. This means that for basic sizing and modelling it will be the first model of choice, but if required comparison/modelling with the other kinetic models stated could be made.

Slotboom et al

In the years since the publication of the model of Van den Bussche and Froment more data has become available on the intermediate reactions for methanol synthesis [25]. Slotboom et al have taken this data and developed a new model which is of the same family (no direct CO route to methanol) as the model of Van den Bussche and Froment. The aim of the authors was to make a model with the least amount of input parameters as possible while keeping the accuracy of the model high [25]. Slotboom et al achieve this by using a number of assumptions amongst which is an adsorbed hydrogen abundance, and statistical analysis is used to find the actual RDS [25].

The experimental data was generated by using two setups. The first set-up used a reactor with dimensions in the order of mm using the CP-488 catalyst from Johnson Matthey, and an experimental range of 483-533 K, 20-50 bar and 2000-10000 GHSV[25]. The other setup used a tubular reactor of 0.28 m catalyst bed length and 3 mm diameter using the same catalyst as the previously mentioned set-up of this section[25]. Slotboom et al indicate that the experimental range was 451-523 K, 20-50 bar and a GHSV of 3000. For both set-ups it was ensured that mass transfer limitations could not occur in the reactors[25]. Using these results the reaction equations based on the potential RDS mentioned were analysed statistically [25]. This gives rise to the following kinetic model and its parameters (note this is the 6 parameters model presented in the work of Slotboom et al) [25]:

$$r_{CO_2} = k_{CO_2} f_{CO_2} f_{H_2}^2 \left(1 - \frac{1}{k^\circ_{p_{CO_2}}(T)} \frac{f_{CH_3OH} f_{H_2O}}{f_{H_2}^3 f_{CO_2}}\right) \Theta^{*^2} \tag{2.37}$$

$$r_{RWGS} = k_{RWGS} f_{CO_2} f_{H_2}^{1/2} \left(1 - \frac{1}{k^\circ_{p_{CO_2}}(T)} \frac{f_{CO} f_{H_2O}}{f_{H_2} f_{CO_2}}\right) \Theta^{*} \tag{2.38}$$

$$\Theta^* = \left(f_{H_2}^{1/2} k_{H_2} + f_{H_2O} k_{H_2O/9} + f_{CH_3OH}\right)^{-1} \tag{2.39}$$

$$k_{CO_2} = 7.414 \cdot 10^{14} \exp\left(\frac{-166000}{RT}\right) \tag{2.40}$$

$$k_{RWGS} = 1.111 \cdot 10^{19} \exp\left(\frac{-203700}{RT}\right) \tag{2.41}$$

$$k_{H_2O/9} = 126.4 \tag{2.42}$$

$$k_{H_2} = 1.099 \tag{2.43}$$

$$Kp^\circ_{CO_2}(T) = Kp^\circ_{CO}(T) kp^\circ_{RWGS}(T) \tag{2.44}$$

$$kp^\circ_{RWGS}(T) \tag{2.45}$$

The model has been published in 2020 and since then been used in publications of newer models based on density functional theory data [48] and in the previous ZEF reactor development [1]. In literature the model shows good performance but experimental work on the previous ZEF reactor gave inconclusive results [25][1]. It is expected that the Slotboom gives more accurate performance due to it being based on more recent kinetic insights. This is also its weakness since due to it being younger there is less experimental/user data on how the Slotboom model performs. With the current ZEF experimental reactor data it is difficult to discern between both models with sufficient accuracy due to the difficulty of measuring mass flow rates in the ZEF reactors [1]. Using more accurate mass rate measurements its hoped it will be possible to settle on a model which most accurately captures the experimental behaviour of the ZEF reactors. If data is sufficiently accurate this comparison will made, and otherwise should be part of future reactor research at ZEF.

Table 2.3: The model of Slotboom et al assumes the following set of intermediate reactions and possible RDS equations[25]:

Reaction	Equilibrium constant	RDS
	CO_2 hydrogenation	
$H_2(g) + 2\otimes \rightleftharpoons 2H\otimes$	K_{H_2}	not RDS
$CO_2(g) + 2* + H\otimes \rightleftharpoons HCO_2** $	K_2	$k_{CO_2} f_{CO_2} f_{H_2} (1 - \frac{1}{kp^{\circ}_{CO_2}(T)} \frac{f_{CH_3OH} f_{H_2O}}{f^3_{H_2O} f_{CO_2}}) \Theta *^2$
$HCO_2** + H\otimes \rightleftharpoons HCOOH** + \otimes$	K_3	$k_{CO_2} f_{CO_2} f_{H_2}^{3/2} (1 - \frac{1}{kp^{\circ}_{CO_2}(T)} \frac{f_{CH_3OH} f_{H_2O}}{f^3_{H_2O} f_{CO_2}}) \Theta *^2$
$HCOOH** \rightleftharpoons HCO* + OH*$	K_4	$k_{CO_2} f_{CO_2} f_{H_2}^{2} (1 - \frac{1}{kp^{\circ}_{CO_2}(T)} \frac{f_{CH_3OH} f_{H_2O}}{f^3_{H_2O} f_{CO_2}}) \Theta *^2$
$HCO* + H\otimes \rightleftharpoons H_2CO* + \otimes$	K_5	$k_{CO_2} f_{CO_2} f_{H_2}^{3/2} (1 - \frac{1}{kp^{\circ}_{CO_2}(T)} \frac{f_{CH_3OH} f_{H_2O}}{f^3_{H_2O} f_{CO_2}}) \Theta *$
$H_2CO* + H\otimes \rightleftharpoons H_3CO* + \otimes$	K_6	$k_{CO_2} f_{CO_2} f_{H_2}^{2} (1 - \frac{1}{kp^{\circ}_{CO_2}(T)} \frac{f_{CH_3OH} f_{H_2O}}{f^3_{H_2O} f_{CO_2}}) \Theta *$
$H_3CO* + H\otimes \rightleftharpoons CH_3OH(g) + * + \otimes$	K_7	$k_{CO_2} f_{CO_2} f_{H_2}^{5/2} (1 - \frac{1}{kp^{\circ}_{CO_2}(T)} \frac{f_{CH_3OH} f_{H_2O}}{f^3_{H_2O} f_{CO_2}}) \Theta *$
	Water formation	
$O* + H\otimes \rightleftharpoons OH* + \otimes$	K_8	not RDS
$OH* + H\otimes \rightleftharpoons H_2O* + \otimes$	K_9	not RDS
$H_2O* \rightleftharpoons H_2O(g) + *$	K_{10}	not RDS
	RWGS reaction - CO_2dissociation	
$CO_2(g) + * \rightleftharpoons CO_2*$	K_{11}	$k_{RGWS} f_{CO_2} f_{H_2}^{1/2} (1 - \frac{1}{kp^{\circ}_{RWGS}(T)} \frac{f_{CO} f_{H_2O}}{f_{H_2O} f_{CO_2}}) \Theta *$
$CO_2* + \odot \rightleftharpoons CO\odot + O*$	K_{12}	$k_{RGWS} f_{CO_2} f_{H_2}^{1/2} (1 - \frac{1}{kp^{\circ}_{RWGS}(T)} \frac{f_{CO} f_{H_2O}}{f_{H_2O} f_{CO_2}}) \Theta *$
$CO\odot \rightleftharpoons CO(g) + \odot$	K_{13}	$k_{RGWS} f_{CO_2} (1 - \frac{1}{kp^{\circ}_{RWGS}(T)} \frac{f_{CO} f_{H_2O}}{f_{H_2O} f_{CO_2}}) \Theta *$
	RWGS reaction - COOH decomposition	
$CO_2* + H\otimes \rightleftharpoons COOH* + \otimes$	K_{14}	$k_{RGWS} f_{CO_2} f_{H_2}^{1/2} (1 - \frac{1}{kp^{\circ}_{RWGS}(T)} \frac{f_{CO} f_{H_2O}}{f_{H_2O} f_{CO_2}}) \Theta *$
$COOH* + \odot \rightleftharpoons CO\odot + OH*$	K_{15}	$k_{RGWS} f_{CO_2} f_{H_2} (1 - \frac{1}{kp^{\circ}_{RWGS}(T)} \frac{f_{CO} f_{H_2O}}{f_{H_2O} f_{CO_2}}) \Theta *$
	RWGS reaction - $*$ and $\odot$ similar sites	
$CO_2* + * \rightleftharpoons CO* + O*$	K_{16}	$k_{RGWS} f_{CO_2} f_{H_2} (1 - \frac{1}{kp^{\circ}_{RWGS}(T)} \frac{f_{CO} f_{H_2O}}{f_{H_2O} f_{CO_2}}) \Theta *^2$
$CO* \rightleftharpoons CO(g) + *$	K_{17}	$rk_{RGWS} f_{CO_2} f_{H_2}^{1/2} (1 - \frac{1}{kp^{\circ}_{RWGS}(T)} \frac{f_{CO} f_{H_2O}}{f_{H_2O} f_{CO_2}}) \Theta *$
$COOH* + * \rightleftharpoons CO* + OH*$	K_{18}	$k_{RGWS} f_{CO_2} f_{H_2}^{3/2} (1 - \frac{1}{kp^{\circ}_{RWGS}(T)} \frac{f_{CO} f_{H_2O}}{f_{H_2O} f_{CO_2}}) \Theta *$

2.6. Packed beds - Improvement Potentials

For the discussion on the relevant process intensification potentials for the use case of ZEF the reader is referred to appendix D.

2.7. Heat transport modelling

The model which forms the basis for further development has been presented by Vroegindeweij [1]. Although further developments will be made it is inevitable that parts of the model will be identical and/or use the correlations selected by Vroegindeweij. To prevent unnecessary re-explanation of these selections and models a short listing below of reused models is made. The general premise will be stated as well as the choice of keeping these models. The exact formula can be found in the appendix, but for in depth explanation the reader is referred to Vroegindeweij's work[1].

1. **Single phase tube flow** Churchill's correlations will be used [1]. No results of previous work have indicated significant issues with these correlations, and therefore it will be reused in this work. Equation I in appendix.
2. **Shell side pressure drop** Kern's correlations will be used [1]. No results of previous work have indicated significant issues with these correlations, and therefore it will be reused in this work. Equation II in appendix.
3. **Packed bed pressure drop** Ergun's correlations will be used [1]. No results of previous work have indicated significant issues with these correlations, and therefore it will be reused in this work. Furthermore this correlation is seen as an industry standard. Equation III in appendix.
4. **Convective heat transfer - tubes** Gnielinski's correlations will be used [1]. No results of previous work have indicated significant issues with these correlations, and therefore it will be reused in this work. Equation IV in appendix.
5. **Convective heat transfer - shell** Kern's correlations will be used [1]. No results of previous work have indicated significant issues with these correlations, and therefore it will be reused in this work.
6. **Convective heat transfer - bed** Mill's correlations will be used [1]. No results of previous work have indicated significant issues with these correlations, and therefore it will be reused in this work. Equation VI in appendix.
7. **Property correlations** CHERIC data will be used in most models, however it will be used in parallel with COCO chemsep imports for VLE [1]. The main transport properties will still be based of CHERIC data, and previous work has shown these are sufficiently accurate. Equation VII and accompanying table in appendix.

2.8. Condensation

Condensation describes the process of matter transitioning from a gaseous to a liquid state. For this to occur it requires the to be condensed species to cool below its dew temperature, and this can by achieved by a heat sink with a contact temperature below this boiling temperature [49]. Generally equipment meant for this action is called a condenser and in process industries appears as some sort of heat exchanger.

For initial sizing design of a heat exchanger standard heat transfer coefficients can be used such as in [50]. What becomes apparent is the wide range of heat transfer coefficients for condensation. Since the functioning of the methanol synthesis reactor of this thesis depends for a significant part on condensing performance a thorough understanding is required. Therefore in the following sections the fundamentals of condensation applicable for the reactor are presented.

2.8.1. Film condensation - the basics

Condensation of a vapour on a surface can occur in the shape of atomization, dropwise, and filmwise [51]. Generally atomization and dropwise condensation do not occur in most process equipment, and therefore will not be looked into further in this work [51]. The first mathematical description of film condensation was obtained by Wilhelm Nusselt in 1916, and is known as Nusselt's film condensation theory with a graphic representation shown in figure 2.11 [49]. The solution assumes: the film flow behaves in a laminar manner, heat is only transferred by conduction over the fluid film, no slip conditions; gravity being the driving force, negligible shear stress by the vapour, and inertia effects being negligible, the properties of the fluid and gas are constant over the film, and the wall is isothermal [52][49]. The derivation of the resulting equation for a vertical plate is omitted but can be found as a standard example in many heat transfer textbooks. In the case of the local heat transfer coefficient one finds [49]:

$$\mathrm{h_{Nusselt}} = \left(\frac{\rho_\mathrm{L}(\rho_\mathrm{L}-\rho_\mathrm{G})\mathrm{g}\Delta\mathrm{h_v}\lambda_\mathrm{L}^3}{4\eta_\mathrm{L}(\mathrm{T_s}-\mathrm{T_0})}\frac{1}{\mathrm{x}}\right)^{\frac{1}{4}} \tag{2.46}$$

In which $\mathrm{h_{Nusselt}}$ is the heat transfer coefficient, ρ_L the density of the fluid phase, ρ_G the density of the gas phase, g the gravimetric constant, $\Delta\mathrm{h_v}$ the enthalpy of vaporisation, λ_L the conductivity of the fluid phase, η_L the dynamic viscosity of the fluid phase, $\mathrm{T_s}$ saturation temperature, $\mathrm{T_0}$ wall temperature, x the distance along the wall from starting of the condensation film [49].

When evaluating this formula for common laminar condensation parameters the high value of the heat transfer coefficient becomes apparent and can be in the order of thousands of $\mathrm{W/m^2K\cdot s}$. However experimental data can deviate significantly (25 %) which is attributed to the following causes [49]:

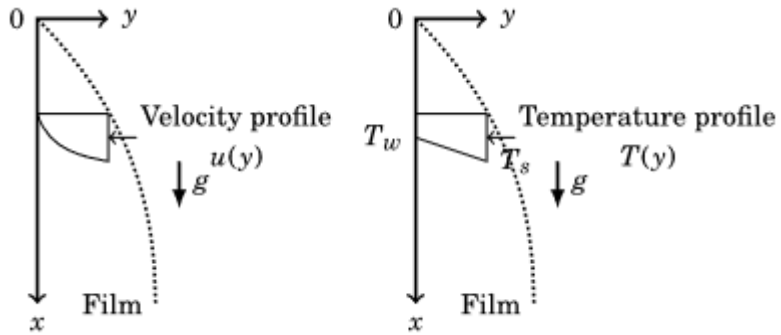

Figure 2.11: Qualitative view of the velocity and temperature profile present in the Nusselt Film condensation theory. Note that the flow is a gravity driven flow. Figure adapted from [52]

1. **Waves:** Above a certain Reynolds number (while still within the laminar regime) waves will appear in the condensate [49]. The waves give the condensate an average lower thickness which causes the conductive heat transport over the film to increase [49]. This increase of the heat transfer coefficient is reported to be in the range of 10-25 % [49]. There exist predictive formulas for the onset of this phenomena for certain liquids however no universal theory exists at the moment [49].

2. **Properties:** Nusselt's theory assumes constant properties throughout the condensate film, however this is an idealisation [49]. The size of deviations depends for a large part on the temperature sensitivity of the dynamic viscosity and conductivity of the fluid[49]. One should evaluate these properties to see if large deviations can be expected when applying Nusselts formula.

3. **Subcooling:** Subcooling indicates that the condensate has a temperature below its boiling point. However Nusselt's theory assumes that the enthalpy difference in the film is due to the change in phase [49]. If the fluid is below the saturation temperature the additional enthalpy difference between saturation and evaluated temperature should be accounted for . However in most situations this correction is of minute significance [49].

Although Nusselt's equation has some deviations from real world experimental results as mentioned above it remains a useful result [53]. In wave-less laminar condensation it is applicable and can be used as departing point for more advanced condensation equations. Furthermore it remains a good explanation of the basics of condensation, and the reason for the high heat transfer coefficient seen during condensation of pure vapours.

Correlations for the transitional and turbulent regime are based on interpolation and experimental or computational works respectively. For the turbulent regime the following correlation deviates ±12 % from experimental values and is based on simulation studies of turbulent flow [49]:

$$\mathrm{Nu} = 0.0325\mathrm{Re}^{\frac{1}{4}}\mathrm{Pr}^{\frac{1}{2}}, \quad 400 \leq \mathrm{Re}_{\mathrm{film}} \leq 7 \cdot 10^{7}, \quad 1 \leq \mathrm{Pr} \leq 25 \tag{2.47}$$

$$\mathrm{Re} = (89 + 0.024\mathrm{Pr}^{\frac{1}{2}}(\frac{\mathrm{Pr}}{\mathrm{Pr}_0})^{\frac{1}{4}}(\mathrm{Z} - 2300))^{\frac{4}{3}} \tag{2.48}$$

$$\mathrm{Z} = \frac{\mathrm{C_{pL}}(\mathrm{T_s} - \mathrm{T_0})}{\Delta \mathrm{h_v} \frac{1}{\mathrm{Pr}} \frac{\mathrm{x}}{(\mathrm{v_L^2/g})^{\frac{1}{3}}}} \tag{2.49}$$

In which Re is the Reynolds number, Pr the Prandtl number evaluated at fluid temperature, Pr_0 the Prandtl number evaluated at wall temperature, C_p the heat capacity of the fluid, $\mathrm{T_s}$ is the fluid temperature, T_0 wall temperature, x distance along the fluid, v_L kinematic viscosity of the fluid and g the gravimetric constant. The interpolation for the transitional regime is given as[49]:

$$\alpha = \sqrt{(f\alpha_{\mathrm{lam}})^{\frac{1}{4}} + (\alpha_{\mathrm{turb}})^{\frac{1}{4}}} \tag{2.50}$$

In which α is the interpolated heat transfer coefficient, α_{lam} the laminar heat transfer coefficient, f a correction factor which can be used in case the laminar has waves and α_{turb} the turbulent heat transfer coefficient. Furthermore a notion should me made of the case when the vapour velocity is of such magnitude that shear effects on the surface affect the heat transfer coefficient [49]. The effect increases with increasing vapour flow velocity, and correlations exist to see the relative contribution of gravity and vapour shear forces [53] [52]. However in this thesis the expected vapour flow velocities are expected to be low based on mass flow rates of the previous reactor of the same type (in the sub g/s category) [1]. Lastly it should also be noted that the Nusselt theory above was developed for a flat plate [52]. However as long as the condensate thickness is considerably smaller than the pipe diameter this plate theory holds for condensation in vertical pipes [52].

2.8.2. Film condensation - non-condensable gasses

In the case of the methanol synthesis reactor the conditions at which the condensation has to occur are peculiar; a relatively low amount of condensable products due to the equilibrium limitations mentioned earlier, a natural convective flow (the velocity of which depends on the difference between condenser and reactor temperature), and a pressure of 50 bar. Due to the presence of gases (which will not condense) the theory on condensation in the presence of non-condensable gases (NCG) has to be used [49].

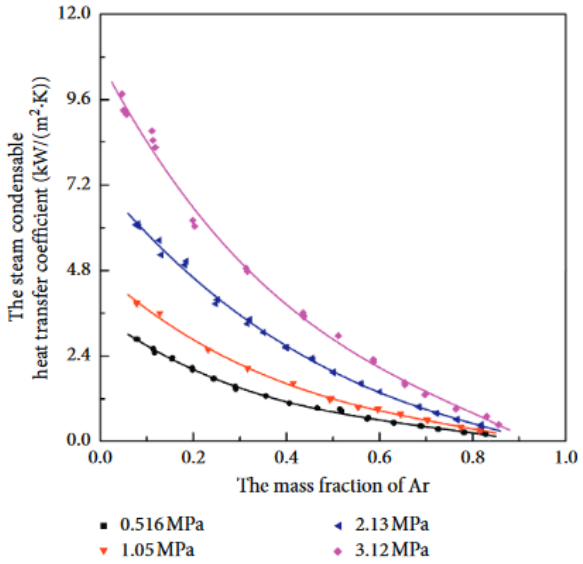

Figure 2.12: An example of the significant decrease in the heat transfer coefficient due to the presence of NCG in condensation at different pressures. Figure adapted from [54].

Understanding of the effective heat transfer coefficient is vital for condenser design, since in the case of the use of air cooled fins on the external surfaces of the condenser the NCG present could limit its effectiveness. An example of the significantly lower heat transfer coefficient due to NCG pressence is given in figure 2.12. Furthermore, understanding the effective cold sink temperature of the reactor will aid in more accurate flow and heat transfer modelling.

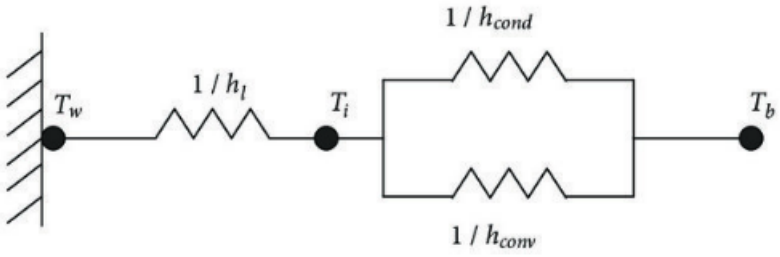

Figure 2.13: The equivalent thermal resistance network in the case of condensation in the presence of non-condensable gasses [55]. Note how the parallel resistance consists of conductivity and mass transfer resistances over the gas layer between the condensate and the bulk gas [56] [55]. Figure adapted from [56].

In the case of condensation in the pressence of NCG, an extra resistance will start to occur due to the nature of the thermodynamics of Vapour-Liquid Equilibria (VLE). At the condensing surface the partial pressure of the condensing species in the gas phase will decrease (the species transitions from vapour to liquid), and inversely the partial pressure of the NCG component will increase as per thermodynamic equilibrium [49][57]. Therefore the partial pressure of the NCG is higher at the condensate film surface

than in the bulk giving a diffusive flux away from the condensate surface [57]. This flux away from the surface frustrates the flux of the to be condensed species directed to the surface. This creates a mass transfer resistance which results in a decreased heat transfer coefficient, since an additional resistance now exist for the condensable species to reach to condenser surface as can be seen in figure 2.13 [57].

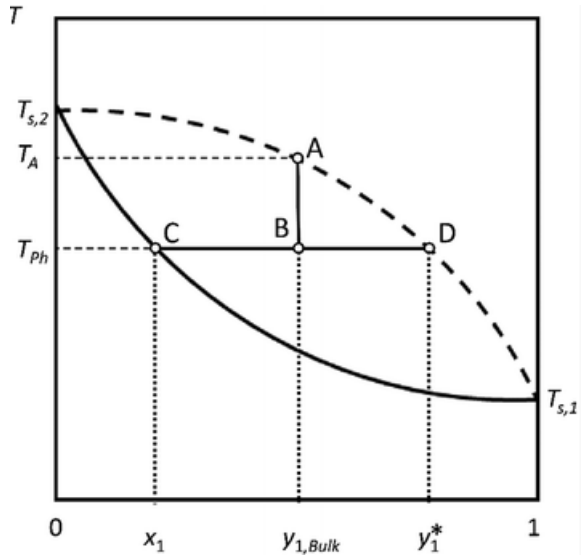

Figure 2.14: An example of the VLE of a binary mixture. Condensation starts at point A if the temperature is held at point B the relative gas content (y) of the later condensing component (effectively the NCG) increases. Figure adapted from [57]

Besides, due to the nature of VLE of which can example is shown in figure 2.14, the presence of the NCG decreases the temperature over the condensate film [49]. This can be made apparent when applying the VLE pressure equations for the condensing species (assuming both phases behave ideally):

$$\frac{\mathrm{y}}{\mathrm{x}} = \frac{\mathrm{P^{sat}(T)}}{\mathrm{P}} \tag{2.51}$$

In which y is the vapour mol fraction, x is the liquid mol fraction, $\mathrm{P^{sat}(T)}$ is the saturation pressure depended on temperature and P is the pressure. In case of the condensing species the value of y is decreasing while x increases due to condensation occurring, thus the left hand side decreases in size. Since the pressure doesn't change in a VLE the saturation pressure has to change and this effect can be seen in figure 2.15 [49].

The relation between saturation pressure and temperature is positive for methanol and water meaning: an increase in temperature means an increase in saturation pressure [58][59]. Therefore in the case of NCG condensation the saturation pressure decreases with the changing gas/liquid ratio and therefore the temperature decreases. This means a lower local temperature at the condensing film front than is the case in single component condensation. The temperature difference over the condensation film will therefore be lower which means a lower amount of conductive heat flux as seen in figure 2.15 [49].

Since the discovery of the degrading effect of NCG on condensation in 1929 (Donald Othmer) multiple approaches exist on quantifying the condensation heat transfer in presence of NCG [51]. The list is plentiful and ranges from relatively simple models fitted to experimental data to rigorous CFD based approaches which can be computationally intensive [51]. However for the case of higher pressure and low liquid concentration in the presence of NCG little experimental data exists. Highly complex computational models are expected to not be a reasonable approach within the time-frame of this work. Therefore a model is selected which roughly falls halfway between the two mentioned options, and which is based on the heat and mass transfer analogy [56]. Furthermore the experimental data used for evaluation of this model comes close to the conditions expected in the reactor (high pressure NCG condensation under free convection) [56].

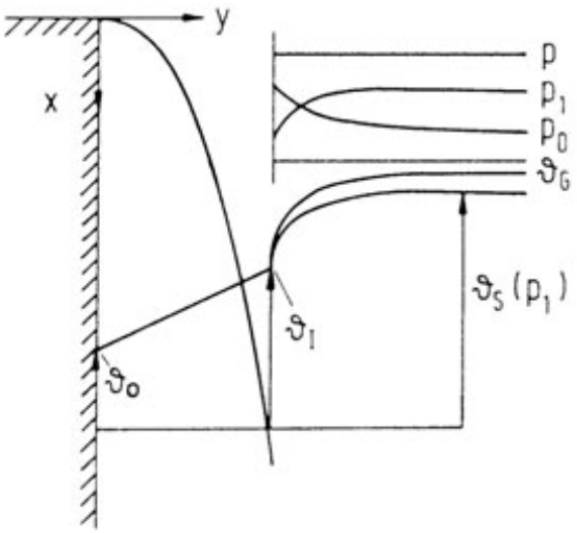

Figure 2.15: In this figure the interplay between pressure and temperature due to the VLE in condensation if the presence of NCG becomes apparent. Once can see in the top right the maintaining of pressure equilibrium as per VLE (P_0 is the NCG and P_1 the condensing species). Meanwhile the θ temperature line shows the depression of temperature over the condensing region. Figure adapted from [49]

The Kim et al Model

The conditions mentioned earlier (high pressure and condensation in the presence of NCG while using natural convective flow) are encountered in passive nuclear safety systems. As mentioned earlier data is scarce and public viewable models are validated experimentally up to 2.6 MPa [56]. An improved model taking off from the model presented here exists, but is applicable to the region in which the vapour quality (NCG concentration) value is too low for this work[60]. Extension of this work exists and into the required pressure range, but is currently not publicly available. [61]. However this work [61] as well as recent purely experimental work by Ma et al, [54] indicate the degrading effect of NCG on condensation at pressures of 5 MPa, and thus within the reactor's operational envelope.

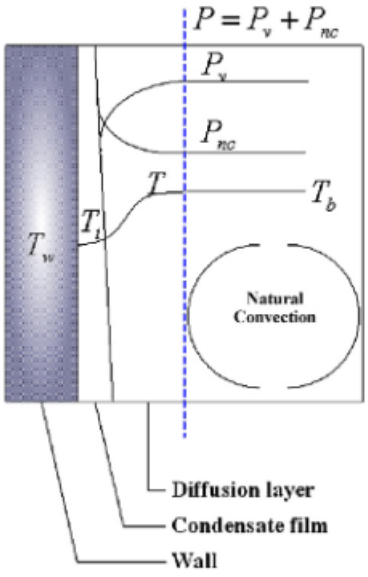

Figure 2.16: The model of the condensation film and NCG diffusion layer as used in [56].

The model presented makes use of the same assumption presented above on NCG and couples these to a heat balance over the condensation region [56]. It assumes conductive heat transfer in the fluid film h_f and in the diffusional layer a combination of convective heat transfer h_{conv} and a heat transporting mass flux h_{cond} [56]. This gives rise to the following equations in which the thermal resistance analogue is used to find the overall heat transfer coefficient[56]. The equivalent thermal circuit has been shown in figure 2.13:

$$h_f(T_i - T_w) = (h_{cond} + h_{conv})(T_{mix} - T_i) \tag{2.52}$$

$$h_{tot} = \frac{h_f(h_{cond} + h_{conv})}{h_f + h_{cond} + h_{conv}} \tag{2.53}$$

In which h_f is the fluid film heat transfer coefficient, h_{conv} the convective heat transfer coefficient in the diffusional region outside the fluid film, h_{cond} the conductive heat transfer coefficient in the diffusional region outside the fluid film, T_w the wall temperature, T_i the interface temperature between the fluid film and the diffusional region, T_{mix} the bulk temperature outside the condensing regions. The heat transfer coefficient for the fluid film is calculated using the classical Nusselt theory with a correction for waviness of the fluid film [56]:

$$h_f(L) = Re_l^{0.04} \frac{k_l}{\delta(L)} \tag{2.54}$$

$$\delta(L) = [\frac{4k_l^3 \mu_l (T_{sat} - T_w)L}{g\rho_l(\rho_l - \rho_v)h_{fg}^{'}}]^{1/4} \tag{2.55}$$

In which $h_f(L)$ is the film heat transfer coefficient, Re the film Reynolds number, k_l the fluid conductivity, $\delta(L)$ the film thickness, μ the fluid dynamic viscosity, T_{sat} the saturation temperature of the species, T_w the wall temperature, L the position along the fluid film, g the gravimetric constant, ρ_l the liquid density, ρ_g the gas density and $h_{fg}^{'}$ the enthalpy of vaporization. The convective heat transfer coefficient is found using the following formula, and note that due to the usage of the Grasshof number natural convective flow is assumed [56].

$$Nu = 0.56(GrPr)^{\frac{1}{4}}, \quad \text{laminar regime} \quad (10^4 < GrPr < 10^8) \tag{2.56}$$

$$Nu = 0.13(GrPr)^{\frac{1}{3}}, \quad \text{transitional regime} \quad (10^8 < GrPr < 10^{10}) \tag{2.57}$$

$$Nu = 0.021(GrPr)^{\frac{2}{5}}, \quad \text{turbulent regime} \quad (10^{10} < GrPr) \tag{2.58}$$

In which Nu is the Nusselt number, Gr is the Grasshoff number and Pr is the Prandtl number. The heat transfer coefficient for the heat transport mass flux is found using the heat and mass transfer analogy in combination with a mass balance over the diffusion layer. It should be noted that by using the heat and mass transfer analogy the Nusselt numbers stated above can also be used as Sherwood numbers, and the Prandtl number as the Schmidt number [56]. This gives the following set of equations[56]:

$$h_{cond} = \frac{m_{cond}^{''} h_{fg}}{T_{mix} - T_i} \tag{2.59}$$

$$m_{cond}^{''} = \Theta \frac{Sh\rho D}{L} \frac{w_{v,b} - w_{v,i}}{1 - w_{v,i}} \tag{2.60}$$

$$\Theta = \frac{X_{nc,i}}{X_{nc,avg}} \tag{2.61}$$

In which m'' is the mass flux as the condensate gas-fluid interface, $\mathrm{h_{fg}}$ the latent heat of vaporization, Sh the Sherwood number, ρ the density of the fluid, D the diffusion coefficient, L the condensation length, $\mathrm{w_{v,b}}$ the mass fraction of NCG in the bulk, $\mathrm{w_{v,b}}$ the mass fraction at the fluid-vapour interface, $\mathrm{X_{nc,avg}}$ the average NCG mass fraction and $\mathrm{X_{nc,i}}$ the NCG mass fraction at the fluid-vapour interface. In the paper where the model is presented the diffusion coefficients are found using a correlation and property tables for the fluid properties [56]. In this work values taken from CHERIC data and COCO will be used, since these allow for the specification of multi-component mixtures as will be the case for condensation in the ZEF reactor.

To be able to evaluate properties at the gas-fluid interface the interface temperature T_i has to be found. To his end an iterative method is applied [56]:

$$\mathrm{T_i^*} = \frac{\mathrm{h_f T_w} + (\mathrm{h_{cond}} + \mathrm{h_{conv}})\mathrm{T_{mix}}}{\mathrm{h_f} + \mathrm{h_{cond}} + \mathrm{h_{conv}}} \tag{2.62}$$

As indicated earlier this model has not been validated for the pressure of 5 MPa at which the reactor will operate, and there is no access to models which have been validated at this pressure. However when observing reported experimental results in [56] for 0.1-2.6 MPa and [62] for 0.214-4.12 MPa one can see that at increasing NCG concentrations the heat transfer coefficient seem to converge to a relatively low value for indicated pressures. Recent experimental work of Ma et al, [62] at pressures of 0.516 - 5.10 MPa seems to confirm this tendency for 5 MPa although no model is presented. Due to this converging tendency at high levels of NCG it is expected that the Kim et al [56], model is applicable for ZEF reactor modelling, and deviations will be relatively low when using this model. Especially since the concentrations of NCG are high within the reactor. Furthermore the model used is based around a set of correlations and mass balances, and is expected to therefore show some rigidity when extrapolated to 5 MPa. Therefore extrapolation is deemed possible due to the model having a theoretical bases although not as stringent as other possible more complex models as in [51]. Lastly it is assumed these models hold for mixtures of water and methanol. To this end weighted interpolations based on the fraction of these species present will be used. As well as the usage of an EOS applicable for these species as will be shown in chapter 3.

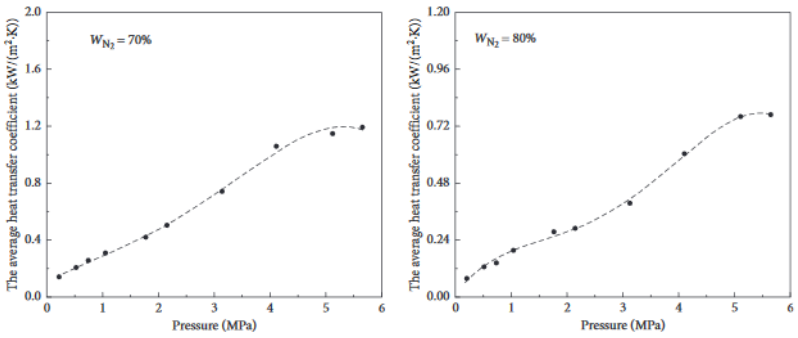

Figure 2.17: The trend in the condensation heat transfer coefficient for a pressure range which includes 5 MPa and a NCG concentration of 70 and 80 % mass fraction. The converging tendency of the heat transfer coefficient by increasing NCG fraction at all pressures can be seen [62].

3

Reactor development: models and apparatus

To be able to perform the next iteration of the methanol synthesis reactor a combined modelling and experimental strategy is employed. Within this chapter the new additions to the overall nodal model are shown as well as the new reactor design for the experimental validation of the developed models. The chapter will make use of a structure in which the model and design of a specific part of the reactor are discussed. At the end of the chapter a short summary is given with the expected performance bandwidth of the reactor design.

3.1. Design philosophy : preventing paradoxes

Due to the many processes occurring in the reactor and their co-dependencies it is difficult to change an aspect of the reactor without affecting other parts. It is however important to somehow create an overview to effectively design the reactor. To this end first the underlying design philosophy and method to evaluate the design is developed. The fundamental process of the reactor is the methanol synthesis reaction taking place within the reactor bed section. The typical range of this reaction is 180-270 $^{\circ}\mathrm{C}$ at 50 Bar according to results from kinetic models and past experimental results of ZEF. The generated products are condensed in the condenser to prevent the occurrence of chemical equilibrium between the reactant and products. The dew temperature in the case of the ZEF reactor typically lies below 150 $^{\circ}\mathrm{C}$ at 50 Bar. To retain a high overall energy efficiency a heat exchange is established between hot reactor section and cold condenser section.

The fluid flow within the reactor is caused by natural convection. The density of the most abundant components of the reactor $\mathrm{H_2}$, $\mathrm{CO_2}$, and CO decreases with increasing temperature. These differences in density will cause a pressure differential generating fluid flow since the volume of the reactor is fixed.

1. Increasing the mass flow rate will allow more mass of reactants to pass through the reactor bed. Assuming this occurs in the kinetically limited region of the reactions occurring the result would be an increase in production. In the eventual experimental results it will be checked whether this occurs.
2. Increasing mass flow rate has effects on the heat transfer coefficients. First of all it could cause a shift from laminar to turbulent flow giving an increase in heat transfer. It is assumed this also applies to the transitional regime due to the interpolation method employed which is equal to the method mentioned in [1].

The two effects shown above show a paradoxical behaviour typical of the reactor design of this type (natural convection reactor): when increasing the mass flow rate more production of methanol occurs and therefore more heat is generated within the reactor bed. However due to the increased heat transfer coefficients this heat will be exchanged more effectively. Due to more heat being lost the reactor bed looses more heat to heating the reactants which decreases methanol production. However for reactor design this paradox is easily resolved using KPI's: the lowering of methanol production is undesirable. There are more of these paradoxes to be found within the reactor, and therefore the design is guided by a set of KPI's. To evaluate whether the performance is reached a model is used which can account for the most relevant physical behaviour taking place in the reactor. The required KPI's of the reactor are:

1. The reactor has a minimum production of 142.5 grams of methanol per hour as required by the current developmental goals of ZEF. This production number should be reached while using natural convective cooling at the condenser section.
2. The reactor bed will not require additional heating after start-up. This behaviour is called autothermal operation in this thesis. The start-up period is defined as the point of when the heaters are first switched on to the point of a steady temperature at the condenser section.
3. The condenser section temperature is as low as possible. This will affect performance of the reactor in three ways. At a lower temperature more methanol will condense from the mixture entering the condenser section:
   (a) More product is condensed (and thus evacuated from the reactor) per pass.
   (b) The lower methanol concentration at entrance of the reactor bed means more methanol can be produced per pass.
   (c) A lower condenser temperature means less heat will be lost to the environment due to the lower driving force.
4. The STY (Space Time Yield) should be as high as possible. As set out in chapter 2 this can be achieved by setting the following KPI's:
   (a) The temperature profile of the reactor bed should be homogeneous and have a derivative of near 0 at the exit of the bed. The effect of the homogeneous temperature profile has been shown in chapter 2. The derivative of 0 refers to the reactor bed reaching chemical equilibrium at the exit of the reactor bed, and thereby optimal utilisation of the reactor bed.
   (b) The effectiveness factor should be as high as possible to mitigate the effects of diffusion transport limitations in the reactor bed.
5. The reactor should exhibit dynamic behaviour in starting up. The time frame for start-up to production is currently set at 15 minutes, but reduction of this time is preferable. A shorter start-up time should allow the reactor to better anticipate changes in input of other subsystems and climate. Shutdown currently has no dynamic requirement.

Furthermore great emphasis will be placed on the mass producibility of the design. Due to the numbering up strategy of ZEF this requirement is seen as vital. This requirement has as a consequence that in the case of two possible options for the reactor both fitting the requirements the more mass producible option will be selected. This mass producibility will generally manifest itself as the simpler, more conventional, and/or long term available option.

The emphasis on KPI's can be seen as the design philosophy for the reactor. The underlying aim of this philosophy is to arrive at a reactor which is as efficient as possible in terms of energy and production while retaining a simple mass producible design. This should give ZEF the most effective reactor design within the overall concept of the microplant. Furthermore it also furthers the understanding in general of possible designs (strategies) for numbering up: a design of this kind used within a conventional methanol synthesis plant could allow the plant to be resilient from intermittency in energy. The specifics for such a case will not be further discussed in this work, but a design from the philosophy shown above holds potential beyond the microplant of ZEF or merely methanol production.

3.2. The overall reactor design

The previous reactor designed by Vroegindeweij as shown in figure 3.1 is the starting off point for the new design. The Vroegindeweij reactor has shown a very high degree of energy integration [1]. he mass flow rate control given by this design is seen as vital due to its effect on the heat transfer coefficients and residence time in the reactor bed. Is is therefore evident that the Vroegindeweij design should be the starting point, and shows great maturity in terms of thermal design.

Figure 3.1: The reactor of Vroegindeweij. It has been shown that this reactor achieves near autothermal operation, and is thermally highly efficient. Image adapted from [1].

3.2.1. Global model

Due to the earlier indicated synergy between the many processes taking place a model describing their interactions is vital. This model will be referred to as the integrated and/or nodal model. With the term integrated it is meant that all processes modelled are placed within one model to best simulate the synergy between them. The basis of the nodal model is the previous nodal model developed by Vroegindeweij, and the correlations reused can be found in the appendix as indicated in chapter 2 [1]. The underlying principle of the nodal model is as follows: the model makes use of the electric circuit analogy for heat and fluid transfer[1]. The model consists of a group of nodes (hence the name nodal model) which are interconnected by elements. The nodes hold information on driving forces such as pressure, temperature and position in the xy-plane, and the elements indicate the resistances/influenced parameters of these driving forces[1]. The main constituents of these elements and nodes are shown in figure 3.2.

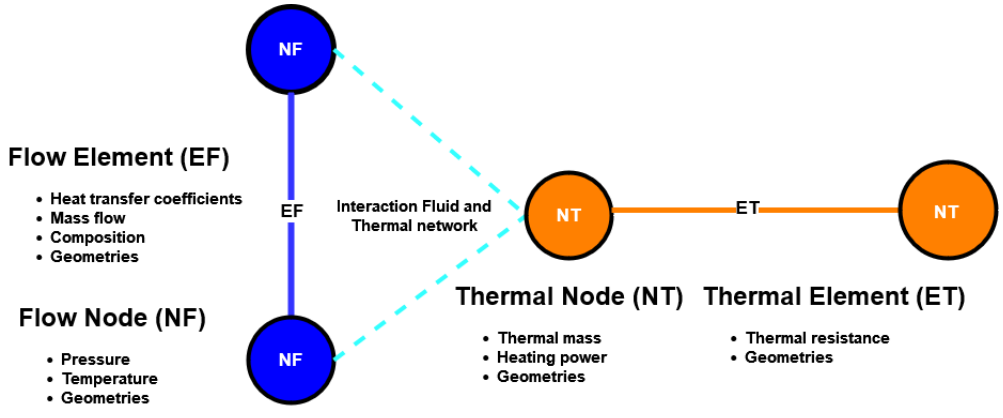

Figure 3.2: The 4 data structures used in the nodal model, main info within these structures, and their interactions.

Table 3.1: The circuit analogy equations for heat exchange within the thermal network, heat exchange between the thermal and fluid network, and fluid flow velocity within the fluid network.

Circuit analogy	Equation	Identifier
NT →ET	$\dot{Q}_{ET} = K_{ET}/x_{ET}(T_{NT,i} - T_{NT,j})$	E-I
NT →EF	$\dot{Q}_{ET-EF} = h_{EF}A_{EF}(T_{EF,avg} - T_{NT})$	E-II
NF →EF	$\dot{m}_{EF}$=$Kf_{EF}(P_{NF,i} - P_{NF,j})$	E-III

The nodal model only tracks the transient thermal behaviour. The underlying assumption is that the thermal inertia of the fluids involved is negligible compared to that the steel tubing. This can be especially made evident when comparing the heat capacity of gas vs steel. A steel tube of 60x3 mm with the length of 0.5 m weights 2140 g (density 8000kg/m^3), and if it contains 4 g of H_2 when assuming the ideal gas law, 50 Bar, and 293 K [63]. The heat capacities are respectively 468 J/kgK and 14.3 J/kgK meaning 1000 J/k for the steel and 0.05 J/k for the gas indicating that the gas has a very low thermal inertia [64][65]. Therefore it is assumed that any change to the fluid such as flow velocity or temperature is instantaneous within the time-step of the thermal transient of the wall. The solver structure as shown in 3.4 of the model therefore contains and inner and an outer loop.

Figure 3.3: The nodal model used for the modelling of the reactor designed in this work. Note the axis indicated the size of the reactor in m.

The inner loop as shown in figure 3.4 is used for solving the fluid network and is solved until equilibrium is reached. It contains a nested loop known as the fluid-network solver. This solver determines for current pressures what the fluid velocity is using a standard matrix substitution solver based on the equation E-I given in table 3.1. The given fluid velocity is returned to the inner loop to evaluate the heat transfer with the walls (assumed constant within the timestep) to the fluid based on the equation E-II given in table 3.1. The resulting new temperature field is found using an analytical solution of the first law of thermodynamics for open systems to obtain the outlet temperature $T_{NF,j}$, and average temperature of the fluid element $T_{avg,EF,i}$ via the equations given in 3.1. The thermophysical properties (such as density and viscosity) are updated using the Cheric's based correlations and the $T_{avg,EF,i}$ as input temperature. Based on these new properties the fluid node pressures are re-evaluated (density is temperature sensitive and therefore the pressure changes) and the inner loop restarts. This process is repeated until convergence is reached using successive substitution. Convergence is reached when an error smaller than 10^{-4} between inlet and outlet of each node is achieved.

$$T_{NF,j} = (T_{NF,i} - T_{NT,i})e^{\frac{-h_{EF,i}A_{EF,i}}{\dot{m}_i C_{p,EF,i}}} + T_{NT,i} \tag{3.1}$$

$$T_{avg,EF,i} = \frac{1}{L}\int T_{NF(A(x)),j}dx \tag{3.2}$$

With the fluid network solved a time step in the outer loop can be performed. If a thermal node is connected to a fluid element it receives information on whether its being heated or cooled. Furthermore thermal nodes can contain info on if they are being heated by external heaters. Following this info the thermal flux balance between the thermal nodes and thermal and fluid elements is made. Using the transient heat equation the rise of temperature of the thermal nodes is calculated:

$$\dot{Q}_{\sum ET,NT} = m_{NT} C_p \frac{dT_{NT}}{dt} \tag{3.3}$$

The time step of this group of ODE's representing the thermal transient of the thermal nodes is determined the internal solver architecture of the used ODE113 solver proprietary of Matlab. This gives the new temperature at which the fluid network must be evaluated and closes the iterative loop. By doing so the nodal model tracks fluid and thermal transport throughout the reactor by solving its equivalent thermo-fluid circuit. For this work an additional dimension is added being species transport to account for condensation behaviour, methanol synthesis reaction equations, and their synergies. Due to the many models which are required for these additional synergies within the nodal model it is key to keep the computational load of each model to a minimum. This will lead to the usage of the following strategies:

1. If possible, a process will be modelled in a separate model and a correlation is derived for use in the global model. This is the preferred method since it offers a minimal increase in computational load, while giving relative accurate results compared to the use of nested models. If this is not possible the second (nested) method is used.
2. The sub-model is included within the global modelled but care is taken to make it as simple, and computationally fast as possible. This will inevitably lead to a decrease in accuracy and/or abilities of the model, and this decrease should be such as to have a minimal negative impact on the overall results.

3.2.2. Composition tracking

In order to be able to track condensation and reaction the nodal model needs some form of a species transport model, and is computationally situated in the inner loop. A simple sink and source model is used while also assuming fluid flow to be instantaneous alike the flow network shown earlier in this text. Therefore the transport model is nothing more than a before and after black box model: the composition is equal for all elements after a sink/source as can be seen in figure 3.5. The source is modelled by the reaction equations, and can be seen as the set of equations that give the composition at which condensation is evaluated. The sink is effectively due to condensate leaving the reactor. Using the PT-flash plug-in *CapeOpenEquilibrium* for Matlab from COCO & ChemSep it is possible to evaluate for an element: if a fluid phase exists, the liquid fraction, and its composition [66][67]. The underlying thermodynamic models used throughout are discussed in the section on the global condensation model.

Using a simple molar balance the total amount of condensation for an element can be found. In the current model the PT-flash used to model condensation is only performed at the element signifying the condensate collection tank, which also has the point of lowest temperature in the reactor. The underlying reason is mainly computational expense, since a PT-flash at each element showed an unacceptable increase in overall computational time. At the PT-flash element the molar balance is used to evaluate:

1. The amount of methanol produced
2. Pressure decrease due the formation of condensation (EOS in figure 3.5)
3. Entrance composition of the reactor bed

It is important to note that it is assumed that the liquid phase does not evaporate from the catch tank (the collection basin for condensate before being evacuated from the reactor). The underlying reasoning is that fluid is regularly purged from the reactor and the inlet of the colder feed gasses is situated close by suppressing evaporation to an extent. The EOS evaluation is used to evaluate the change in pressure according to changes in total number of moles and temperature in the reactor.

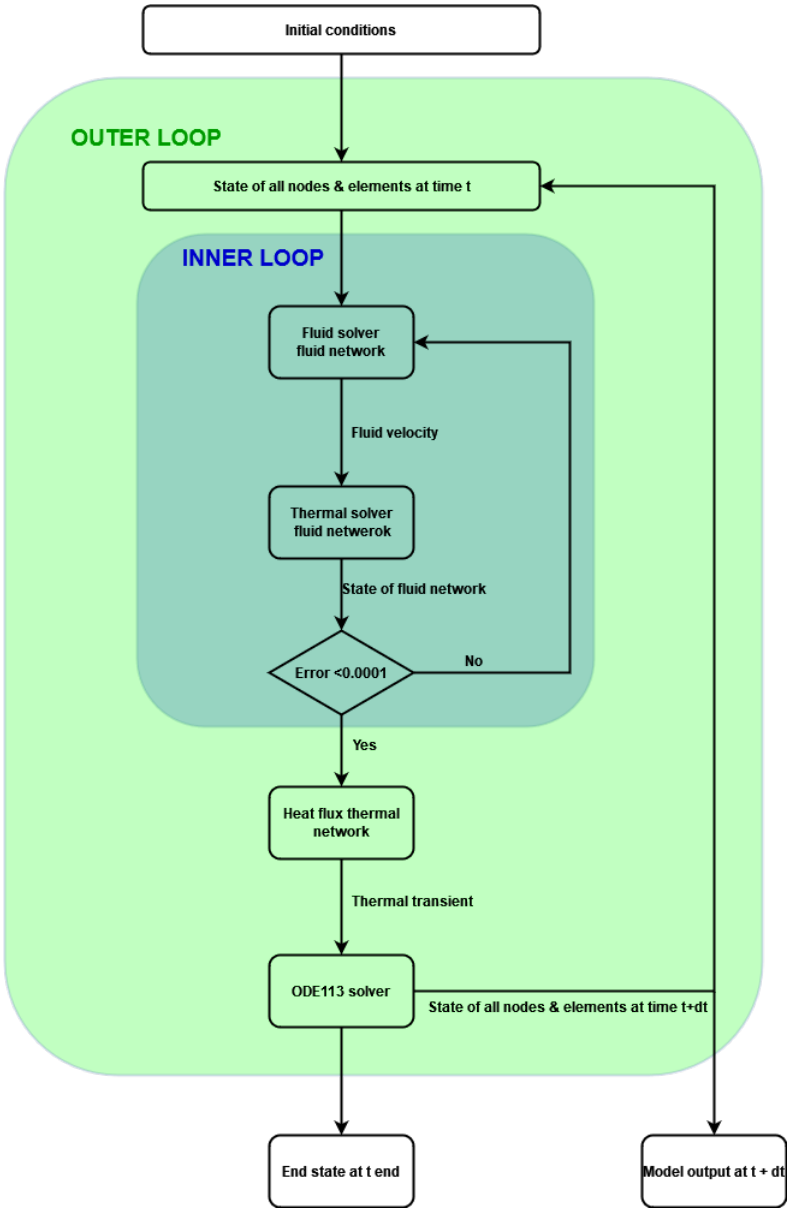

Figure 3.4: A high level view of the logic of the nodal model, and the inter-dependencies of the multiple solver structures used.

If the pressure drops below the pressure set-point a certain amount of feed-gas is injected being a certain ratio of CO_2&H_2. The ratio used determined by the feed model which is discussed in a separate section. The removal of condensate in the reactor is currently modelled as a continuous process. This is deemed acceptable since the liquid condensate cannot re-enter the reactor since the condensate holding tank is before the entrance of the heat exchanger (the start of the reactor). The model tracks the amount of condensate removed at every time-step and adjusts the pressure accordingly. Due to this approach the model is currently unable to imitate the sudden emptying of the condensate tank as in the physical design.

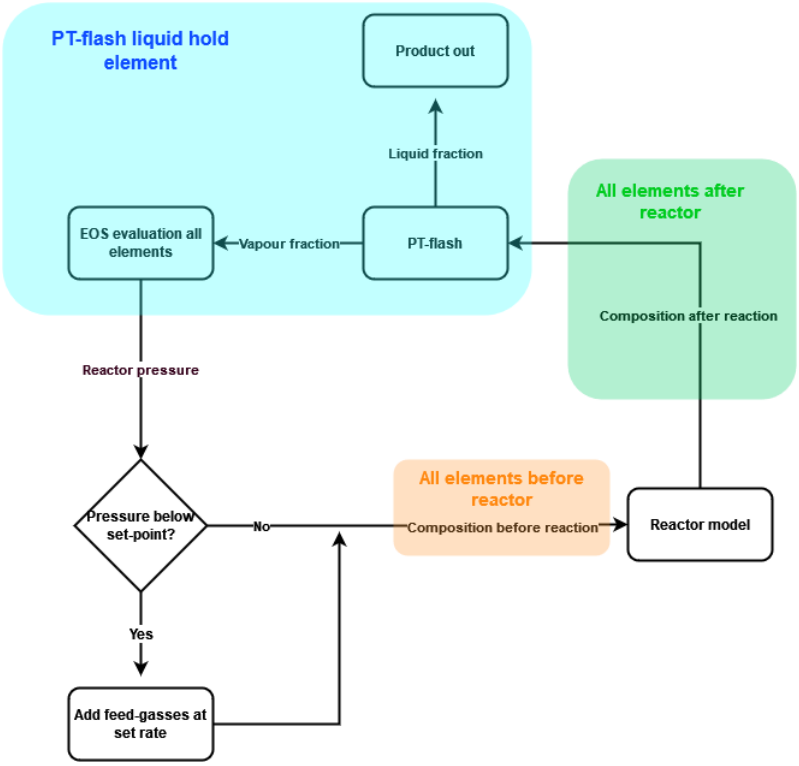

Figure 3.5: A graphical representation of the logic employed for the modelling of species transport/composition tracking.

3.2.3. Global condensation model

The tracking of the condensing behaviour of species throughout the reactor geometry is achieved with the condensation modelling strategy of Ir. Jan van Kranendonk. The core principle is to capture the latent heat release of condensing species in a single temperature dependent variable. By using this approach an iterative approach is prevented and it can be implemented in the existing nodal model architecture. The variable selected for this approach is the C_p which is generally defined as follows:

$$C_p = (\frac{dH}{dT})_p \tag{3.4}$$

The species which are able to condense at the operating temperature of the reactor are water and methanol, and their dew temperatures are in relative close proximity of one-another. Due to the low conversion per pass of the reactor bed the fraction of non condensing species (H_2, CO_2 and CO) is relatively high. Due to the presence of these gasses condensation will not be an isothermal process, and thus the enthalpy-diagram will show a slope between 0-1 in the condensing region as can be seen in 3.6. The temperature will vary during this phase change, and if one assumes Vapour Liquid Equilibrium (VLE) the composition of the mixture can be found at a given temperature and pressure.

By exploiting this behaviour a curve fit is made to this enthalpy-temperature diagram in the condensing region. This gives giving a temperature dependent C_p signifying latent heat release due to condensation, and is called the pseudo C_p method. Normally C_p is defined as in equation 3.4 with the dH referring to the change in sensible heat, and is already used throughout the model. In the case of the method of the pseudo C_p the latent heat change is also incorporated into the dH term. This allows for the description of the heat effects of condensation into a single variable already in use in the nodal model. This prevents the use of a heat balance over every fluid element in the reactor and therefore keeps the added computational work to a minimum.

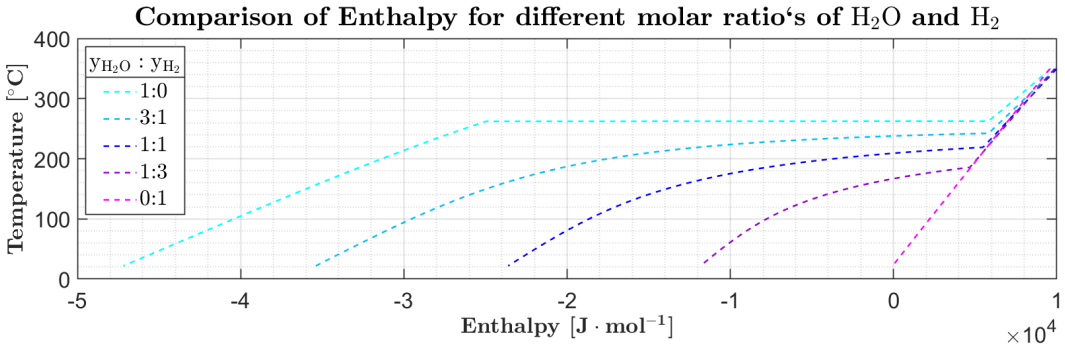

Figure 3.6: Enthalpy plots for different compositions of water and hydrogen at 50 Bar in the condensing region for water. Note the dramatic effect on the Entahlpy curve of in case of only water (a molar fraction of 1:0), a mixture containing hydrogen and water, and only hydrogen (a molar fraction of 0:1). Note that in the case of a molar fraction of 1 for water the condensing region is isothermal, and therefore it is impossible to define a correlation due to the slope being 0.

In order to develop this pseudo-C_p the difference in enthalpy between two temperature states of the mixture while being at the gaseous and liquid state for a certain composition, mass, and temperature have to be known. To this end the MatLab plug-in *capeOpenEquillibriumProp* of COCO will be used which is able to find enthalpy of a mixture at VLE for the earlier indicated inputs [67]. The COCO MatLab plug-in uses the software ChemSep to make the necessary thermodynamic VLE calculations [66][67]. The main VLE balance equation and the underlying thermodynamic methods in the case of this thesis are the following [68] [69]:

$$\frac{y_i}{x_i} = \frac{\gamma_i \phi_i^{\circ} P_i^{\circ} (PF)_i}{\phi_{i,v} P} \tag{3.5}$$

1. **VLE method :** The modelling approach used for evaluation of the equilibrium between the gas-liquid phases is the $\gamma - \phi$ method. This is a modelling approach which is used oftenly for gas-liquid phase equilibria. It effectively shows at the given state (pressure and temperature) below the dew point what fraction of a species is in which phase.

2. **Equation of State :** The **Predictive SRK** EOS is used to know the underlying interactions between state variable as well as the calculation of properties such as Enthalpy.

3. **Vapour pressure :** Is the pressure the liquid phase of the species is on the verge of evaporating at a certain state. Its a required model input for the $\gamma - \phi$ method and in this case the **Antoine equation** will be used.

4. **Activity coefficient :** Shows the deviations caused by species interaction and non-ideal behaviour of the species which aren't captured by the ideal formulation of the $\gamma - \phi$ method. In this case the **NRTL** model for the activity coefficients is used.

The selection of the thermodynamics models is based on the following strategy: the group of applicable thermodynamics models for conditions of the reactor are identified, with the fastest in terms of computational time being the preferred option. This means that if a certain model has a slightly better fit, but a significantly higher computational run time it will not be used. The leading selection method for the thermodynamics models is the paper of Carlson, and can be seen as equivalent to commonly used selection trees available in software such as Aspen [70]. The selection of these models is based on the typical conditions which are expected to occur within the reactor: the reactor contains a mixture of predominantly the gasses H_2, CO_2, and CO which will have a combined molar fraction in the region of 0.85-0.99 depending on temperature, pressure, and the extent of reaction occurring. The two condensing species H_2O and CH_3OH will generally be present at molar fraction of around 0-0.06 due to the relativey low generation of these species at the temperatures and pressures present.

The pressure is generally 50 Bar with the maximum expected range being 30-65 Bar, which is based on Vroegindeweij's work and preliminary calculations [1]. The dew temperature for these mixture specifications is generally within the 150-90 °C bandwidth according to preliminary calculations in COCO and previous experimental results at ZEF[1][32][33][24].

The mixture is thus predominantly composed of gasses which do not condense, and are at elevated pressure and temperatures. However $\mathrm{H_2O}$ and $\mathrm{CH_3OH}$ are polar components, and they can be present in their liquid state. This is important for two reasons: 1) the liquid phase has great effect on thermodynamics due significant interaction of the liquid phase molecules [70] 2) the $\mathrm{C_p}$-pseudo model revolves around accurately tracking the enthalpy of the condensing species making accurate modelling of the liquid phase imperative[70]. Therefore the following choices in the flow-chart of Carlson shown in the appendix are made[70]: polar components, non-electrolytes, P>10 bar, no interaction parameters available. This leads to the EOS selection of Predictive SRK (PSRK), and for the activity coefficients a host of options were available. The NRTL coefficient were evaluated and gave results during preliminary testing comparable with experimental results of Vroegindeweij, while retaining relatively low computational times [1]. The same line of reasoning was used for the selection of the Antoine equation. It should be noted that this set of models is partially forced due to the initial selection of using the Gamma-Phi model. Which is an often selected method for VLE calculations involving a liquid and fluid phase. Lastly it should also be noted that the enthalpy is found through the use of the PRSK EOS [69]. The line of reasoning being that the EOS is found to be sufficient for VLE, and therefore sufficient to track the enthalpy changes. It also reduces the computational load with the EOS being used for multiple parameters in the computations. For a more exact description of the inner workings of the ChemSep software, and models used by Chemsep the reader is referred to the ChemSep website [66][69].

The result from the discussion above is that there now exists a single adjusted value, the pseudo $\mathrm{C_p}$, which can describe the latent heat released by condensation within the reactor. Due to it being based on a VLE evaluation the fraction of condensed methanol (the production) can be evaluated at the same time. Therefore the effect of condensation on species transport can also be evaluated without requiring more complex model strategies or changing the fundamental workings of the nodal model to for example Finite Volume techniques.

Model implementation

In order to obtain the Enthalpy-temperature correlation for the condensing region a linear fit is made using Chemsep [66]. Composition and pressure are only updated every time-step and therefore constant within the iteration cycles. Therefore the correlation only has to be determined once per time step. The dew temperature and the enthalpy are found using the Chemsep-Matlab interface. In case of the enthalpy a set of 1000 points between the dew temperature and the ambient temperature are calculated to which a linear fit is made. The linear fit is selected due to it giving a relative good fit while maintaining a linear equation for the nodal model. Higher order fits can be used, but would require linearisation at the inner loop fluid network evaluations. For now the linear method is judged to be appropriate, but if large deviations are seen during experiments higher order fitting might be required. An example of these pseudo-C_p correlations are shown in figure 3.7.

The model checks at every element if the temperature will go below the dew-temperature signifying condensation. If this occurs the C_p is substituted for the C_p-pseudo value which is a function of temperature. The end temperature of the element is used as the start temperature of the next element downstream. Thereby it is possible to continuously track condensation over the fluid elements. The used fit for the C_p-pseudo is updated at the end of each outer loop of the nodal model using the new composition and pressure of the reactor. The modellings strategy has a low impact on the overall computational time, and makes the model acceptably slow. A single time-step takes in the order of tenths of seconds instead of multiple minutes when using an earlier iterative scheme (initially attempted within this work). Despite the low computational time increase it is possible to track condensation throughout the reactor with a high degree of fidelity.

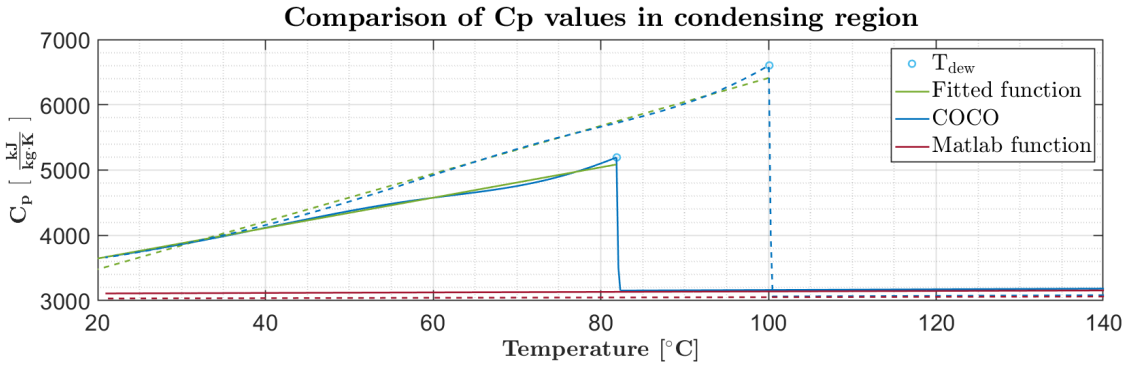

Figure 3.7: Pseudo heat capacity curves and the resulting linear fits used by the nodal model. Both cases assumes a 1:1 molar ratio of water and methanol. The solid lines are in case of a total condensable molar fraction of 0.02 and the dashed lines for a total molar fraction of 0.04. The rest of the composition in both cases is made up of $H2$, CO_2 and CO for SN=2. Note that the term 'Matlab function' is the normal C_p value based on Cheric data for the particular composition. Comparing to the fitted function the added latent heat release is clearly visible.

3.2.4. Feed model

The model is able to track the amount of methanol production in the reactor, and the accompanying decrease in pressure. Therefore a feed of reactants CO_2 and H_2 has to be included in the model to keep the reactor at a certain specified pressure (generally 50 bar). Furthermore as shown in the work of Vroegindeweij composition drift will occur due to unequal adsorption of reactants in the condensate taken from the reactor [1]. These dissolve into the condensate at unequal rates thereby giving an increasing excess of H_2 in the reactor due to it dissolving less readily in the condensate. The feed system is also used to keep the composition entering the reactor bed as close to optimal as possible, with the optimal being defined by the stoichiometric number (SN). Literature indicates that the ideal number is 2 although industry generally uses slightly higher numbers (see chapter 2). The control scheme is based around a set SN, the sum of the molar fractions within the reactor, and the fact only H_2 and CO_2 are injected.

$$SN = \frac{H_2^i - CO_2^i}{CO + CO_2^i} \tag{3.6}$$

$$1 = y_{CH_3OH} + y_{H_2O} + y_{H_2}^i + y_{CO_2}^i + y_{CO} \tag{3.7}$$

The fractions of CH_3OH, H_2O, CO cannot be controlled and are therefore equal to the measured values. The feed system, and thereby control, can change the fractions of H_2, CO_2 by injection of these gasses. By using the SN and the measured values of CH_3OH, H_2O, CO the ideal values of H_2, CO_2 can be found which are annotated as y^i. Using the actual measured molar fractions of H_2 and CO_2 this is combined into a proportional feed algorithm. This allows for tuning of the gains for each feed separately which is needed since the species absorb in the condensate at different rates. This gives the following simple feed algorithm:

$$y_{CO_2}^{in} = K_{CO_2}(y_{CO_2}^i - y_{CO_2}) \tag{3.8}$$

$$y_{H_2}^{in} = K_{H_2}(y_{H_2}^i - y_{H_2}) \tag{3.9}$$

$$n_{in,species} = K_p * (P_{set} - P) * n_{species}^{feed} \tag{3.10}$$

Due to the algorithm contains multiple gains (K_i) the effect of the cascaded-PID used in the eventual controlling software for the experimental apparatus is mimicked. Lastly a hard coded if statement is used for each species molar fraction to prevent negative molar fractions which are nonphysical. The resulting feed algorithm is able to keep the reactor within 10 % of the specified stoichiometric value. Generally a positive deviation is observed which is attributed to the composition drift which favours an

excess in hydrogen. However the feed system currently is of the proportional type and therefore will by definition never reach a steady state. For now this is deemed as acceptable since this is not the major focus of this work, and it is able to keep the composition within close proximity of the required SN. However in the eventual final reactor system a proportional-integrator-derivative (PID) control will be used to ensure a steady state composition. The result is that the reactor model is able to be kept at a certain (advantageous) composition, and the effects of certain Stoichiometric Numbers evaluated should this be necessary.

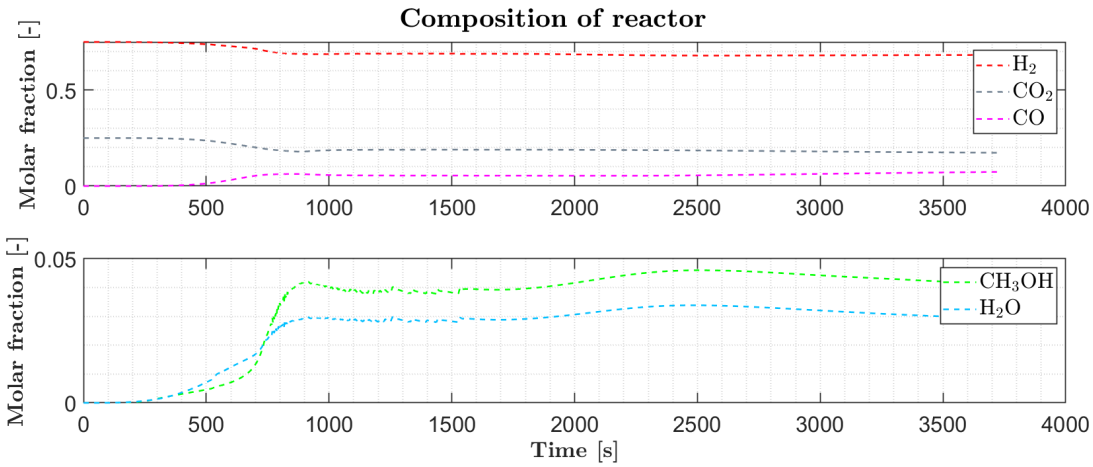

Figure 3.8: An example of the composition in the reactor while utilising the control scheme. It can be seen that the reactor is kept within 10 % of the SN = 2 requirement as is evident from the relative molar fractions of H_2, CO_2, and CO. The methanol water ratio of approximately 4:6 instead of 1:1 is attributed to the effectiveness factors being unequal for the two reactions in the reactor sub model.

3.2.5. 5X reactor

The overall design of the reactor will now be introduced, but its important to note that the final design also depends on results from the sections further in this chapter. The reason for already introducing the overall design here is that information of the overall design is vital for understanding of later sections within this chapter. The overall design is effectively a continuation of the Vroegindeweij reactor, and thus makes use of the same geometry.

Material selection

The basic material for the pressure bearing and internal structures of the reactor are made from 316L or 304L stainless steel. These steel types are able to resist corrosion from the species within the reactor at the elevated temperatures and pressure. The L type of these materials is selected due to their better weld-ability than non L type [71]. All the main piping material will be made from 316L seamless tubing since this has the most optimal resistance against corrosion [71]. The seamless version is selected due to their slightly higher performance with respect to bursting pressure, and more importantly these have higher degree of roundness compared to welded tubing [72]. This is vital since for example the heat exchanger baffles need good contact with the inner walls of the tube to prevent significant bypass flows. With this selection coupled with the evaluation of the safe pressure at elevated temperature and pressures the possible diameters for the reactor are specified by the piping available. The pressure calculations are based on the method introduced by Vroegindeweij combined with the calculator available through Sandvik/Alleima [1] [73]. Following iteration of possible reactor designs with the possible diameters tubing was selected: the heat exchanger, reactor bed section, and injection site section will be made from 2 inch schedule 10S ASTME 316L tubing with the dimensions 60.33x2.77 mm.

This pipe is the thinnest option available which is deemed safe at the required diameter. It is able to handle up to an excess of 70 Bar in design pressure at 300 °C, and therefore gives a comfortable safety margin. The smaller tubing for interconnection between the reactor bed and heat exchanger as well as the condenser itself is 25x1.5 mm 316L seamless tubing. This tubing is somewhat oversized in terms of design pressure with 120 Bar at 300 °C while a 1 mm version is also available. The slightly thicker option is chosen to allow for a slightly larger amount of steel at the weld interfaces to decrease the influences zone of the welds.

Heat exchanger

The heat exchanger design makes use of a triangular pitch which holds 55 stainless steel tubes of 4.2x0.2 mm with a length of 400 mm. The underlying reason for selecting a triangular pitch is that it allows for more tubes per area compared to a square arrangement at equal pitch. The reduction of total reactor volume gives a reduction in total volume of hydrogen. This is allows 1) for a great margin of safety and 2) allows for a higher recycle rate of gas compared to a larger heat exchanger at equal mass rates. The downside is that a triangular pitch will cause a higher pressure drop and is more susceptible to fouling. The issue of fouling is seen as minute as shown by Vroegindeweij [1], and the tubes are from stainless steel who themselves are not very susceptible to corrosion. The increased pressure drop is also not seen as an issue, since the mass rate can be tuned by the reactor bed design with minimal increase in internal volume. The baffles are constructed from 0.5 mm thick 316 stainless steel. The required holes and circumference is made through laser-cutting and the tubes are held by friction. Ideally one would like to use a punched baffle structure due to the resulting interference fit (which is nearly leak tight), however the tolerances for the laser-cutting are of such low order (0.5 mm) that these are seen as acceptable [74]. The 15 baffles are of a 35 % cut design, and are placed in the same pattern as Vroegindeweij (alternating left-right) to allow for the passage of condensate between baffle sections [1]. The endplate baffles are welded to the sides of the heat exchanger tube to allow for maximum sealing of the shell side. On the outside of the shell of the heat exchanger a group of 4 NTC are mounted with a pitch of 1 per 2 baffles starting at the shell outlet point. Furthermore a differential pressure sensor is placed on the heat exchanger pipe side entrance/exit to be able to evaluate the mass rate during experiments.

Figure 3.9: The used heat exchanger design.

Injection assembly

The injection section of the reactor (sometimes called the catch tank) also serves as an interconnection, and holds the condensate before being sluiced from the reactor. It is constructed from the 60.33x2.77 mm pipe and its proprietary endcaps. The feed injection sides are placed high up in the assembly with a 45 degree angle in the horizontal plane between these ports. On the inside these assemblies point to a piece of stainless steel inner tubing which creates a gas trap. The underlying idea is that the injection gasses of H_2 and CO_2 will mix upon injection and can only escape downwards with the rest of the gas flow as shown in case II of figure 3.10 and figure 3.11. This should prevent the problem of flow stall in which the light gas H_2 will travel up into the condenser against the flow which can cause the flow stall phenomena experienced by Vroegindeweij shown as case I in figure 3.10 [1]. At the end of this piece a stainless steel gauze is tac-welded to allow for the condensate to drop down, while the gasses can enter the heat exchanger. A separate injection site on the condenser was made at the exit of the heat exchanger for H_2 in case the earlier mentioned injection system proves unsatisfactory which is shown as case III in figure 3.10 and figure 3.15.

Figure 3.10: Blue arrows indicate the direction of normal flow, grey the flow of CO_2 and red H_2. Case I show the occurrence of flow stall. Case II is the mixing chamber injection design, Case III the injection of H_2 on the exit side of the heat exchanger.

The bottom of the assembly serves as the collection basin for the condensate and is equipped with two level sensors. When the top level sensors indicates that there is liquid at that level the basin needs to be emptied. The bottom level sensors on the other hand should keep wet, and is thus the point at when the emptying of the basin should stop. This approach is chosen to have a minimal release of gasses from the reactor since the condensate will act in the same manner as a water seal. The exact working of these level sensors are explained in the work of Vroegindeweij, but essentially it measures if there is a short between the isolated pin of the sensor and the reactor body due to the presence of liquid between the two [1]. Furthermore the assembly holds connections for thermal senors, pressure sensors, and valves (manual and electronic) called the control tree in figure 3.11.

Figure 3.11: The injection assembly including the catch tank. The coloured arrow indicates the direction of flow, with the colour cyan meaning condensate and blue cold gas. Also note the differential pressure sensor port for mass rate measurements.

Insulation

Insulation of the reactor is seen as vital. In theory the reactor should be able to perform in an autothermal manner, and one of the main contributing factor towards this manner is effective insulation. The previous reactor design made use of off-the-shelf pipe insulation sections. It was found during experiments that these sections insulated the reactor below expectations, and the main cause is suspected to be gaps in the insulation [1]. These gaps are attributed to the complex geometry of the previous reactor which required multiple separate insulation pieces. In an attempt to negate this effect and improve insulation of the reactor a custom insulation design was developed with special attention to the prevention of gaps. The developed solution was to make a single large plastic casing in which the reactor sits. This casing is then filled with loose stonewool which will form to the shape of the reactor preventing gaps, and also should speed up the time consuming work of insulating a complex geometry. The produced casing was made by vacuum forming Vikon 3mm plastic over a foam mould made using CNC. This mould is based of the geometry of the reactor, and designed such that any part of the reactor is covered by 60 mm of insulation. The casing is made from multiple interlocking pieces to allow installation in parts, and these are sealed by the use of Kapton tape, PVC beams, and aluminium foil. The interior of the plastic shell is covered in aluminium foil to reflect as much thermal radiation as possible back towards the reactor. The outer casing has been painted honey yellow to allow evaluation of the insulation's performance through FLIR imaging.

Figure 3.12: The issolation casing overall shape can be seen in the left image. The right image shows the interior of the casing during the filling with stonewool. Note the usage of aluminium foil and the close fitting nature of using loose stonewool isolation material.

3.3. Condenser design

The condenser has a twofold function within the reactor; it facilitates the condensation of the products, and acts as the cold sink for the natural convective flow. In general it can be stated that the lower the temperature of the condenser the higher the mass flow rate when assuming that the reactor bed temperature remains the same. Furthermore it can be shown by a sensitivity study in COCO of the PT-flash for the mixtures present in the reactor, that a lower temperature means more methanol and water will be on the liquid side of the resulting VLE as seen in figure 3.13. Generally a condenser temperature of below 70 degrees $^{\circ}C$ is desirable due to the relative large amount of methanol and water on the liquid side of the VLE.

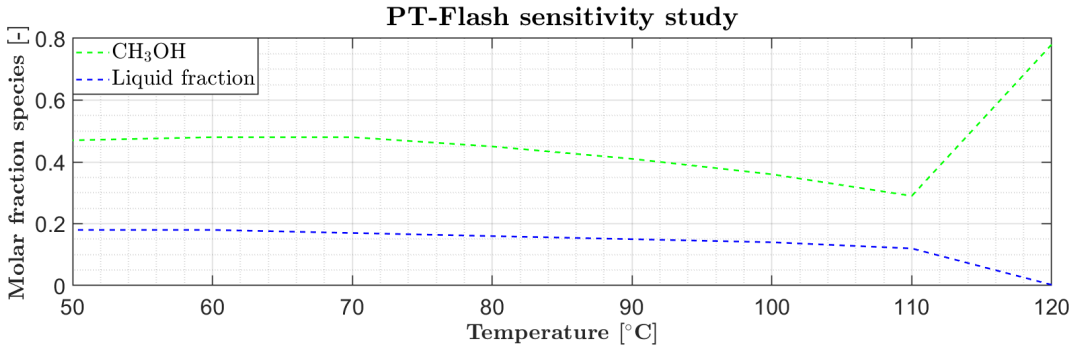

Figure 3.13: The total liquid fraction and partial methanol liquid fraction evaluated at different VLE temperatures for a typical reactor composition (5 % CH_3OH, 4 % H_2O and SN = 2 of H_2, CO, and CO_2) and a pressure of 50 Bar. Note that the initial high liquid fraction is due to the earlier onset of methanol condensation compared to water.

As shown in chapter 2 the condenser will likely have a lower heat transfer coefficient at the inside of the tube for the condensation than initially expected according to Nusselt film theory due to the presence of Non Condensable Gasses (NCG). The performance of the condenser has a big effect on the performance of the reactor. Its temperatures have a direct impact of methanol production through the amount of condensation, and mass flow rate as indicated above. Therefore its decided to have a condensation model for the condenser that can take the NCG effect into account. The model used in this work is an iteration upon the work of kim et al [56] with support from the work of [60] for the modelling of condensation in the presence of non-condensable gasses.

3.3.1. Wall condensation model

The original Kim model is presented in chapter 2, and the discussion held here is to indicated where the model used deviates from the original model [56]. For an overview of the original model the reader is referred to chapter 2. The heat transfer coefficients in the Kim model are for the case of natural convection, and although the mass flow of the reactor is due to natural convection this correlation is not used [56]. It is deemed that locally at the condenser wall the flow regime should be viewed as that of forced convection. It is known from the Vroegindeweij reactor that the fluid flow is in a downwards motion past the condenser surface, and the bottom of the condenser is colder than the top [1]. This temperature field would mean no fluid flow/circulation would be present in the condenser since the gas densities would remain in hydro-static equilibrium. The fluid circulation in the condenser is thus the consequence of the natural convection of the whole reactor, and not a local natural convection at the condenser wall. Therefore it is judged that the fluid movement over the condenser wall must be seen as forced convection when modelling wall heat transfer effects. The natural convective heat transfer coefficients in the Kim model are substituted for the forced convection heat transfer coefficients already in use in the nodal model [56]. For the fluid properties the following correlations/methods are used:

Table 3.2: The used sources for thermal and fluid properties for the NCG modelling.

Phase and molar fractions	COCO PT-flash [67]
Mixture Enthalpy values	COCO/chemsep [67] [69]
Viscosity liquid water	correlation [75]
Viscosity liquid methanol	correlation based of tabulated data [76]
Viscosity gasses	nodal model correlation [1]
Heat capacity gas	nodal model correlation [1]
Conductivity gas	nodal model correlation [1]

The COCO/ChemSep-MatLab interface is identical to the one used in the global condensation model, and therefore makes used of the same underlying models. The usage of the PT-flash and the assumption of VLE is assumed to be applicable since the Nusselt film condensation model assumes a constant gas temperature. With the use of the COCO-MatLab interface the model is able to account for interactions between species within the mixture, and effects of pressure and temperature. In the original Kim et Al model look-up tables where used for this purpose, while the work of Wu [60] made use of an EOS alike the COCO-MatLab interface used here. The other correlations listed are selected due to their application range falling within the conditions expected to occur within the condenser.

Due to the changes between the Kim et Al model and the newly developed condensation in the presence of NCG a direct validation was found to be impossible. However qualitatively the new NCG model shows the same physical behaviour:

1. The higher the NCG content the lower the heat transfer coefficient
2. The decrease shows the same exponentially trend of heat transfer coefficient vs NCG content
3. A decrease in pressure decreases the overall heat transfer coefficient at the same fraction of NCG content
4. Furthermore the results are also in the ballpark of other sources on NCG effects such as Sinnott and Towler [50]

This information is deemed sufficient to allow use within the model and is expected to be able to show the effect of NCG within a reasonable margin of error, but experimental refitting is expected to occur.

Initially it was intended to have the model evaluate the condensation in the presence of NCG at every element for every outer loop step. It was found this was not a realistic approach due to convergence issues with the PT-flash at gas molar fractions above 99 %, and significant computational time increase. The convergence issue is attributed to the Kim model using an iteration cycle to find the interface temperature between the fluid and liquid layer [56]. Due to the low amount of methanol and water in some of the PT-flashes the COCO-MatLab plugin could experience non-convergence. This gives unrealistic values which in turn would crash the nodal model. In analogue to the method of the pseudo C_p a curve fit was developed for use in the nodal model.

Two fitting parameters are required for the adjusted Kim model: temperature difference between the gas and wall temperatures, and the fraction of non condensables present. The initial temperatures given as input are $\mathrm{T_{wall}} = \mathrm{T_{dew}} - \frac{1}{2}\Delta\mathrm{T}$, $\mathrm{T_{interface}} = \frac{1}{2}\Delta\mathrm{T}$ and $\Delta\mathrm{T} = \mathrm{T_{gas}} - \mathrm{T_{wall}}$. The interface temperature is then iterated upon to ensure the heat balance over the combined wall and condensation layer is maintained. Implicitly this information will be fed back into the nodal model due to is iterative nature, and therefore its expected that effects such as wall sub-cooling can be captured to some degree. In general its expected that this modelling behaviour specifically needs to be refitted to the case of ZEF, due to the many variables involved and the simplicity of the model. However it is expected that the model before fitting will show valuable qualitative data, and will be quantitatively within the ballpark which is deemed sufficient for prototype reactor design.

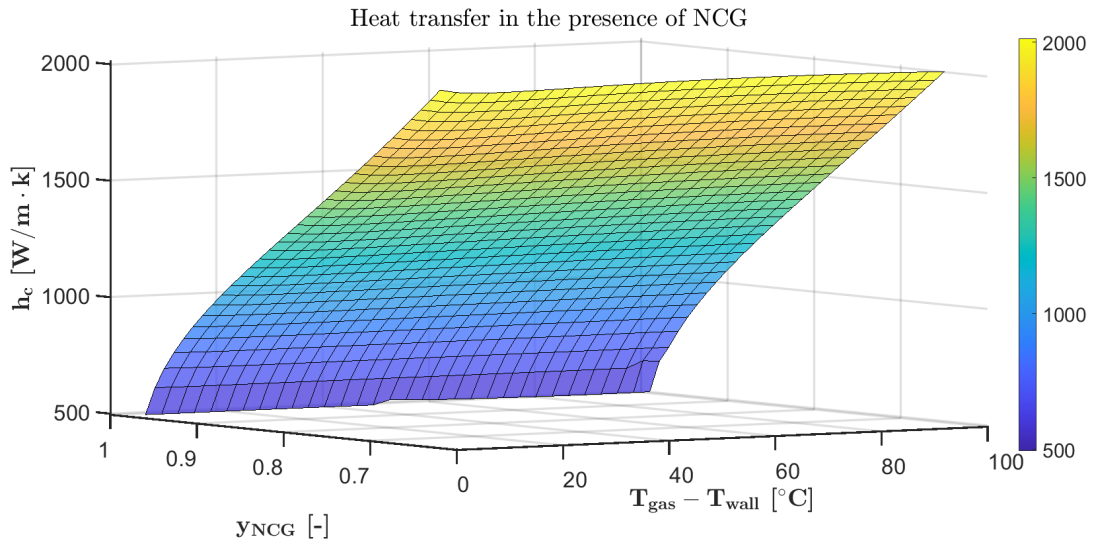

Figure 3.14: A surface plot of the modelled heat transfer coefficients at different molar fractions of NCG and difference in gas and wall temperature. These results were obtained for a typical steady state composition and mass flow rate of the reactor at 50 bars. The fraction cannot be increased beyond 0.98 due to PT-flash convergence issues. The $|\mathrm{deltaT}$ lies within the range of 110 - 130 degree °C. Note that although there seems no effect of the difference between gas and wall temperatures this does exits, but has a significantly lower impact on the overall heat transfer coefficient.

With the nodal model able to predict the condensation behaviour in the presence of NCG the possible limiting effects can be accounted for. In case of limitation caused by NCG presence multiple options are presented in literature. Due to the numbering up strategy of ZEF only solutions with a simple (non-mechanical) nature are available.
This leads to the use of the low finned tube as a method of minimising the degrading effects of NCG presence on condensation [57]. Low finned tube as their name suggests makes use of fins which are relatively short (in the order of a millimetre in height and width) and generally also with a relatively low pitch (again in the order of millimetres)[57]. This increases the surface area where condensation can occur, and causes hydrodynamic effects of the condensate which both increase the heat transfer [57]. Looking at presented literature data [57] one can make a rough prediction of the improvement on the heat transfer coefficient, and is deemed to be at least a 2x improvement by the author.

If limitations occur due to NCG presence it would manifest as a condenser which cannot condense all products. This would increase the methanol fraction at the inlet of the reactor bed, and thereby lower the overall possible synthesis in the reactor bed. Furthermore the presence of condensate in the tube-side of the heat exchanger could cause clogging causing blockage of the flow. Therefore a low finned heat exchanger is to be produced and kept on standby. In the case experiments/numerical simulations indicate this effect occurs it can be countered.

3.3.2. Condenser design

The condenser design as can be seen in figure 3.15 is made from 25x1.5 mm seamless 316L stainless steel tubing. At the two ends of the condenser 25 mm Swagelok male connectors are placed to allow relatively easy swapping between multiple condenser designs. In this work its expected that this feature will be of minute significance, but it will make the developed design more future proof for additional experiments. If only the condenser performance proofs unsatisfactory it can be reworked without requiring significant overhaul of the entire reactor.

The condenser section itself is made of a circular finned section using aluminium fins, 54x25x0.5 mm fin disk size, a pitch of 1.5 mm and an overall length of 250 mm. This gives an outside area of 0.28 m^2 and when assuming a natural convective heat transfer coefficient of 15 W/m^2k gives a value of 4.2 W/k. Assuming a typical difference between condenser and ambient temperature of 60 K (based on experimental results of [1]) it gives a heat duty of 250 W. In case forced convection is used (a fan) on the condenser the maximum possible heat duty assuming no NCG limitations is 400 W (convective heat transfer coefficient of 25 W/m^2k based on [1]). In case one assumes a heat transfer of 1000 w/m^2k at the tube side due to NCG effects its clear the air side should be limiting. In case of a lower heat flux is found this could be attributed to the presence of NCG. The results do seem to suggest that NCG presence at the condenser will not hamper its functioning. Furthermore the fin efficiency is relatively high meaning that in the case of the fan not being used the condenser should retain a high cooling performance. Next to the thermowells also a set of 4 NTC's will be mounted to the surface of the fins to accurately track the temperature over the surface of the condenser. Using this temperature data the performance of the condenser and the validity of the models can be evaluated.

Figure 3.15: The condenser design and major parts. Note the red/blue arrow indicates direction of flow and qualitative temperature distribution through the condenser. Furthermore note the two types of H_2 injection sites as discussed in the injection assembly segment and in figure 3.10.

3.4. Reactor bed design

The reactor bed design, and major models are discussed in appendix D.

3.5. Apparatus overview

Using an iterative design cycle based on the presented models and KPI's presented in this chapter the overall reactor was designed. All major sub-assemblies (reactor bed, condenser, injection assembly, and condenser) have already been introduced and are not explained further. Together these make up the total reactor as can be seen in figure 3.16.

Figure 3.16: The experimental apparatus as constructed with the major sub-assemblies visible as well as the high number of NTC sensors and their placement.

Two typical outputs are given in figures 3.17 and 3.18. On average the numerical runs performed in the final design indicate that the reactor should be able to perform at or above the set KPI's. However it is observed that the reactor bed has a tendency to overheat when experiencing higher bed inlet temperatures. With overheating it is meant that the reactor bed achieves a temperature at which thermal sintering is expected to occur (T > 280 °C. Furthermore this high temperature is seen as undesirable since it the maximal possible methanol fraction according to the chemical equilibrium is very low meaning a low STY. It was checked whether this was due to a numerical artefact in the reactor bed solver, but it was found not to be the case. Later it has been realised that it is very likely the overheating effect is due to the bed being modelled by a homogeneous model while the bed is very thin in width (25 mm). Therefore thermal effects of openings, the thermal mass of the reactor bed, and individual catalyst pellets has not been taken into account which are suspected to lower the overall temperature. A further discussion on this aspect will be held in chapter 5. However at lower bed inlet temperatures the reactor does not experience the overheating effect. Using COCO simulations, historical experimental evidence of ZEF, and preliminary modelling using the Vroegindeweij as checks for the new model the results are trusted enough to realise the design as experimental apparatus [1]. The expected performance is:

Table 3.3: The evaluated KPI's of the reactor according to the model. Note that the values in which the model indicates that overheating would occur are distrusted, and therefore shown separately.

Optimal bed inlet temperature (no overheating)	210 °C
Condenser temperature (Optimal case	84 °C
Start up time	930 s
Chemical equilibrium in bed	No
Autothermall operation	Yes
Mass flow rate	0.9 g/s
Max. production methanol (no overheating)	205.2 g/h
Optimal bed inlet temperature (overheating)	215 °C
Max. production methanol (overheating)	274 g/h
Max. production methanol (adiabatic bed)	274 g/h

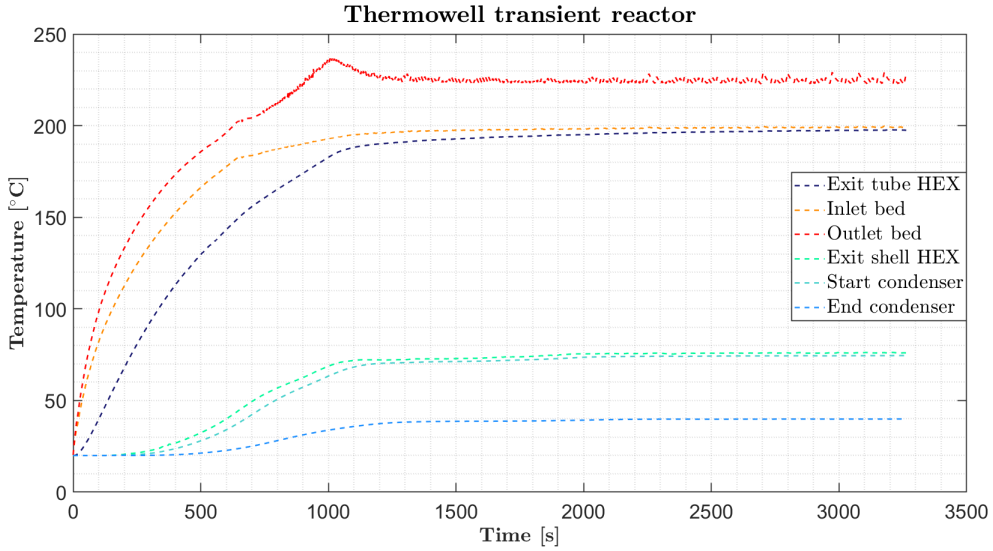

Figure 3.17: The thermal transient of the thermowell positions of the numerical model. Note that the instability of the reactor bed outlet is due to the effects of the solely proportional feed algorithm.

Figure 3.18: The thermal heat map of the reactor geometry. Note that this is an exact overlay of the nodal model earlier shown in this chapter in figure 3.3.

The experimental apparatus was constructed based in synergy with the design above. For example if a certain item was unattainable or extremely expensive it holds no merit for a numbering up design. The model was continuously updated and rerun to ascertain whether certain options did not cause a negative impact in the performance of the reactor. The data acquisition system used is shown in the appendix (based on a custom pcb) and is based around the same principles as Vroegindeweij [1]: an Arduino microcontroller for control, command, and aquisition coupled to a custom PCB with actuator control and sensor readout breakout boards. The final experimental apparatus without insulation was already shown in figure 3.16. In figure 3.19 the reactor can be seen with insulation as it would appeared to the viewer during experiments.

Figure 3.19: The reactor during experiments with the insulation casing closed.

4

Discussion: Experiments & Model

The only method to validate the model and design presented in the previous chapter is through experimental work. The main developmental effort of this work is the nodal model and the redesign of the reactor bed. Due to this the experimental sets are mainly aimed at understanding the performance of the reactor bed, and validation of the nodal model. However due to all processes having a high degree of synergy (effectively meaning that the sum of the processes is greater than its parts [23]) in the reactor the experiments should be sufficient to study the impacts of the new injection system, heat exchanger design, and the isolation casing.

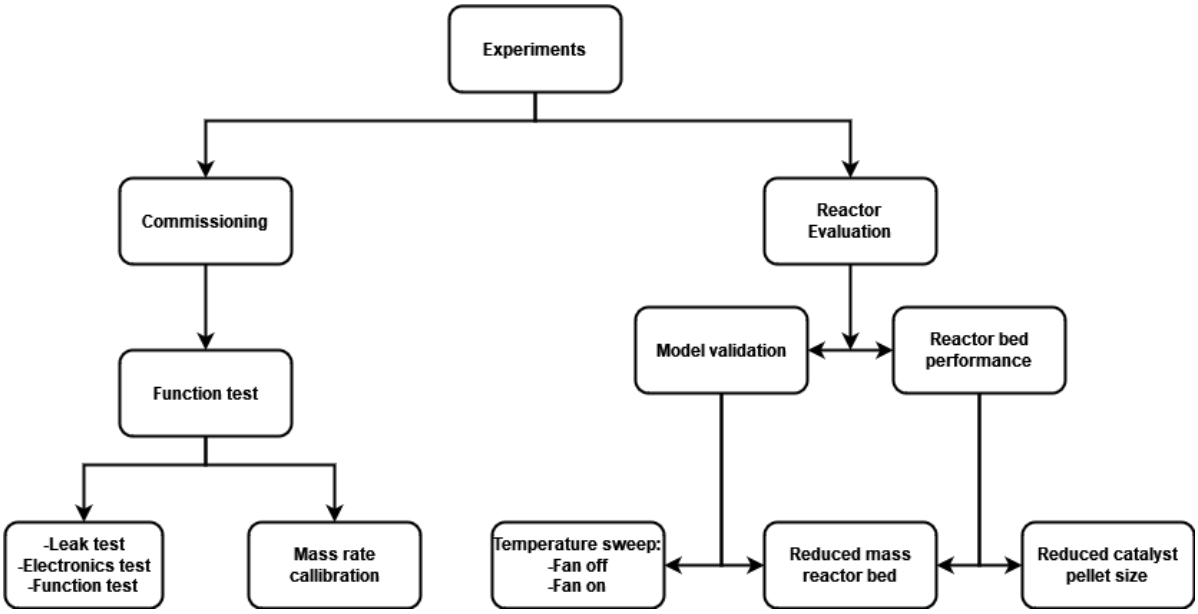

Figure 4.1: The used experimental approach in the reactor experiments. Note the strong interconnections between the model fitting and reactor bed characterisation.

Initial experiments at the left part of figure 4.1 are performed using N_2 to verify that the reactor is able to establish flow, to perform function tests of all electronics, to check for leaks and other mechanical faults, and initial understanding of the thermal behaviour of the reactor. These experiments are performed for a number of hours, with at least 1 hour at steady state conditions. The characterisation experiments (temperature sweep with and without a fan in figure 4.1) were performed using H_2 and CO_2 with the composition controlled by the composition tracking system described by Vroegindeweij [1] and Deli [35].

The control algorithm of chapter 3 was adjusted in the sense that it makes use of a cascaded PID as shown in figure 4.2. Experiments generally take between 4-5 hours if no major issues arise during operation of which at least 2 hours are at steady state conditions.

Figure 4.2: The cascaded PID control scheme used during the reactor experiments.

In order to determine the behaviour of adverse flow fields in the reactor bed a set of experiments was performed with reduced catalyst mass (reduced mass reactor bed in figure 4.1). To evaluate the effect of catalyst effectiveness a group of experiments using smaller catalyst pellets was also performed (reduced catalyst pellet size in figure 4.1). In the cases of the reduced mass reactor bed and the reduced catalyst pellet size experiments two separate use cases are tested during a single experiment: the Fan off and Fan on case. This means that the condenser section is cooled by a fan (Fan on) or cooled by ambient air (Fan off). This allows for a reduction in the total amount of experiments required since the effects between these two cases is known through the temperature sweep experiments. Also in these experiments the composition control algorithm described above and in figure 4.2 will be used.

Heating during experiments

The reactor was designed to be heated solely by the preheater with a heating power of 800 Watt. During initial experiments using N_2, and the first experiments using H_2 and CO_2 it was found that the time required to heat the reactor bed to a sufficient level for the reactions to start to occur far exceeded acceptable limits. Generally the exothermicity of the reactions takes over the heating duty of the heaters, but only if a sufficiently high methanol synthesis is reached. The underlying reasoning is discussed in detail in the sections on thermal behaviour, but for now it suffices to say that the thermal modelling of the thermal inertia and heat transfer to the reactor bed proved to be erroneous.

Next to the pre-heater also 3 wall heaters were installed with a combined power of 450 Watt. These were initially meant for potentially creating a uniform wall temperature at the reactor bed surface. When using these heaters combined with the pre-heaters a sufficiently high reactor bed temperature could be achieved to start the methanol synthesis. However two issues arose with the preheater:

1. The power demand of 800 W proved to be beyond the thermal capacity of a single powerFET used on the PCB. Therefore the pre-heater power has since been capped at 400 W.
2. Undesirable flow phenomena occurred when using the wall and pre-heater in unison during the start-up phase of the reactor. The outlet of the condenser had a higher temperature than the inlet of the condenser indicating the reactor flowed in reverse. If the pre-heater has a higher temperature than the walls (attributed to the pre-heater having a lower thermal inertia) gas might start flowing up the connection tube. This will cause the reactor to flow in reverse, and hamper the functioning of the reactor. Therefore a new start-up procedure was developed and was used for all experimental data.

The heating of the reactor was found to be significantly different from what was initially predicted. The underlying reason is likely inadequate modelling of the thermal-fluid behaviour of the reactor bed, and will be discussed in the section on the reactor bed. Due to system limitations discussed above the following start-up sequence was used during experiments:

1. After filling the reactor to a composition of 3:1 molar fraction H_2:CO_2 (SN=2) with a total pressure of 50 Bar the wall heaters are set to a temperature of 230 °C.
2. When the temperature of the top part of the cooler is 10 °C above the tube side entrance of the heat exchanger (the thermowell in figure 3.11) the preheater is set to the desired inlet temperature.
3. The wall heaters are set to a temperature 20-25 °C below the set-point of the preheater. Initially 20 °C is used, an if undesired overheating of the reactor bed is obsererved the value is increased to 25 °C.

Do note that the model has also been adjusted to this new heating-up procedure and therefore is different from the heating up sequence assumed in chapter 3. This is not adjust in chapter 3 since the design is based around the older start up sequence.

Findings - initial experiments

1. **The pre-heater was shown to be insufficient to heat the reactor bed to a temperature to start the exothermic methanol forming reactions. To be able to reach this temperature, wall heaters placed at the reactor bed aid in heating the reactor bed.**
2. **A specific start-up sequence is required since otherwise the reactor could enter a flow regime with the potential hampering reactor functioning. The underlying method is to first establish flow using only wall heaters after which the pre-heater is used for the largest part of the heating duty.**

4.1. Flow - Control Domain

The flow in the reactor is key in understanding how the reactor performs. First of all it indicates what the regime is in which the reactor operates, and it can be evaluated how well the model is able to predict the mass flow rate. This information is crucial when the heat transport aspects and production characteristics of the reactor are evaluated/modelled. Therefore the flow evaluation is presented before the other sections due to their dependence of their evaluations on flow data. Furthermore flow phenomena uncaptured by the model can elucidated and their possible effects on the reactor operation evaluated.

4.1.1. Mass rate - Measurement methods

Most of the correlations within the model make use of a gas velocity, and indicates whether the reactions are kinetically or mass transport limited. Generally the mass flow rate will be reported but this can be easily converted to a gas velocity if required. Accurately measuring the gas velocity is therefore imperative, and three methods are employed to this end.

Differential pressure

The first and foremost method of flow rate measurement is through the evaluation of the pressure drop over the heat exchanger tubes. This is seen as essential since the preheater thermal methods used in previous reactor design are unusable during autothermal operation. Also when the heating power required is relatively low the pre-heater based mass rate evaluation methods become increasingly susceptible to small deviations in temperature, correlations, and constants degrading the accuracy of these methods. Furthermore the pressure drop due to flow through tubes is a well studied phenomenon, and the correlations are known to be reliable. In this work the same correlations are used as in the nodal model to evaluate this pressure drop: the Darcy-Weisbach equation with the Churchil friction factor shown in Appendix A and shown in [1].

While comparing these relations with the experimental data care is taken to accurately model the viscosity, and density. To this end the nodal model correlations of CHERIC shown in Appendix A are used with the experimental data: the composition, and average temperature between inlet and outlet of the heat exchanger tubes are taken as input for these correlations.

The sensor itself is a Honyewell 26PC A6D differential pressure sensor with a Adafruit LTC4311 I2C extender. On first glance this is an odd choice due to pressure rating of the sensor being nowhere near 50 Bar of static pressure. However, the accuracy of the sensor is sufficient, and there is already in-house experience in using this sensor making it the preferred option. To adopt the sensor for usage at higher pressures it is placed within a 1.5 inch 304 stainless steel StillDragon tube, and entombed using very thin epoxy resin. By doing so the sensor can take the static pressure of 50 Bar while measuring the differential pressure (which is in the Pa-range) between the tube outlet and inlet.

Figure 4.3: On the left hand side of the image the differential pressure sensor before entombment. On the right hand side the StillDragon casing of the sensor is circled in green.

The differential pressure sensor is known to have a rather noisy output as well as an offset. The offset has been identified to be 80 Pa using data of when the reactor is off (cold and at 20 Bar of pure H_2). In order to decrease the noise level in the data a moving average filter is used. It was found that by using a moving average of a 100 samples with equal weight for all points (which translates to around 100 seconds in experimental time) gave sufficient noise reduction without losing too much fidelity. The resulting averaged pressure data is then evaluated using the earlier mentoined Darcy-Weisbach method. The resulting velocity data is converted to mass rate using the temperature, and composition experimental data. Evaluation compared to the model, and other measurements methods is done in the separate result subsection. For now it is sufficient to state that the values based on this differential pressure method (DP-method) are within the expected range and show a high degree of stability and repeatability.

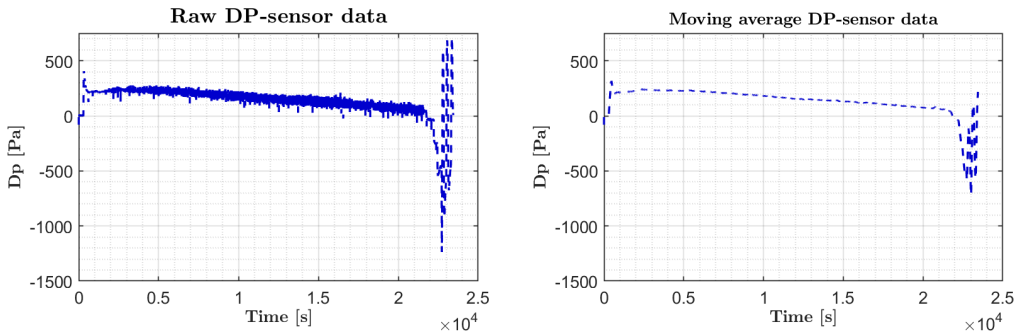

Figure 4.4: On the left hand side the differential pressure sensor data as collected during experiments. The rather noisy nature of the signal is evident. On the right hand side the data after using the indicated moving average filter. The artefact on the right is due to shutdown procedure of the reactor which involves multiple pressure cycles.

During experiments it was found that the casing of the differential pressure sensor increased on average 10 °C from ambient temperatures. It was established that this is mainly due to conduction through the stainless steel connecting tubing since gas conductivity is significantly lower. Therefore it is unlikely that the sensor itself experienced higher temperatures, and furthermore it falls well within the temperature compensated range of the sensors which is 0-50 °C.

Pre-heater transient

Historically within ZEF the main source of mass flow rate measurements for the reactors was based on thermal evaluation of heating power input and temperature response. This method is also applied in this work with the aim of increasing the confidence in the mass rate measurements. Due to how the pre-heater section has been designed the open systems approach of Vroegindeweij [1] is only partially possible. Therefore a different method is used for continuous measurements in which the cooling response of the heaters in the pre-heater themselves are used for mass flow rate evaluation.

Figure 4.5: The pre-heater section, showing how fluid moves through the section, and the expected temperature profile in case the heaters are on (red signifies a higher temperature than blue).

The underlying method is the lumped capacity model which is effectively the analytical solution of the 1-D heat equation when assuming only convective heat transport. In general for this method the Biot number has to be below 0.1 and in the case of the heaters has been evaluated to be around 0.04 allowing the usage of this method. The lumped capacitance model used is defined as follows[77]:

$$\frac{T(t) - T_\infty}{T(t=0) - T_\infty} = e^{\frac{Ah_c t}{mC_p}} \tag{4.1}$$

Evaluating a typical data output such as in figure 4.6 the transient temperature input ($T(t)$) will be the heater input, and the fluid temperature (T_∞) is selected as the thermowell temperature. The underlying reasoning is that the heaters show a significantly greater transient in the cooling region. The heating region cannot be used since the lumped thermal capacitance model assumes no heat generation in the solid (the heaters). The relevant temperature data (heater temperature and bulk fluid temperature) as well as the all constants except h_c can be derived from models, design, and experimental data. The major unknown h_c implicitly holds the flow velocity through the Reynolds number. Using the relevant Nusselt correlation (the Kern correlations taken from Vroegindeweij [1]) and constant taken from the nodal model this flow velocity is found and recalculated to a mass flow.

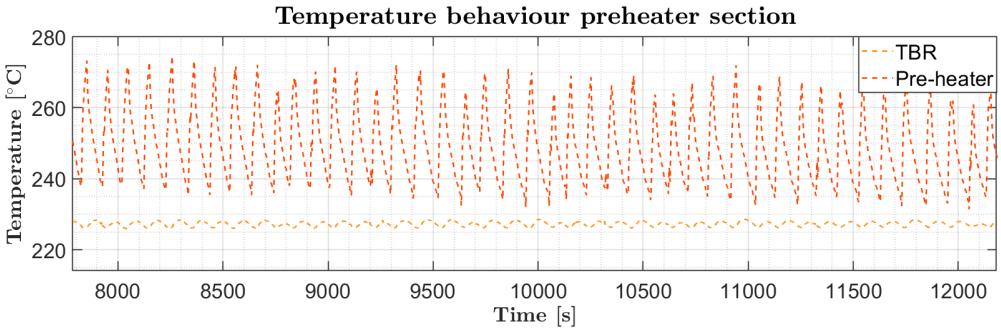

Figure 4.6: The strongly varying temperature profile of the heater can be seen as a function of time as well as the the smaller amount of oscillation in the thermowell. Based on their temperature responses the mass flow rate can be determined through the lumped thermal capacitance model.

Although theoretically this method should hold for any instance, the heater is heated/cooled passively (the heater itself then generates no heat) it is found during data analysis that this does not hold for the start-up period of the reactor. The underlying reason is suspected to be that next to the heaters the walls of the reactor are also warming up distorting the signal of the bulk gas temperature. During steady state (when the pre-heater itself is also in use) the walls of the reactor are assumed to be at relative by constant temperature: these have a significantly slower thermal transient compared to the heaters cooling significantly slower, and thereby distorting the data less.
It appears that during the cycling behaviour of the pre-heater this effect seems to hold and the wall heater cooling effect is sufficiently small to obtain relevant data. The cycling behaviour referred to here is when the heater switches on and off to keep the inlet bed temperature at a certain point as shown in figure 4.6. This on and off behaviour has a rather constant frequency with such a period that heating and cooling of the heaters can be observed well.

The resulting mass flow rate results (which will be shown in the result sections) show to be within the range expected. However the data is significantly more ambiguous than the differential pressure calculated mass rate. This is due to the many more unknowns taking part in the evaluation (temperature, correlations, and relevant surfaces). Also due to the oscillating nature of the measurements there exist a lower and upper bound value to the average mass rate. Nonetheless it aids in identifying the possible mass flow rate values. Furthermore with additional calibration this method could significantly increase in reliability, and allows for measurements in the eventual reactors in the field without the usage of a differential pressure sensor.

Pre-heater steady state

The third method for mass rate analysis in this work is the same as the one presented by Vroegindeweij [1]. This method is based on measuring the inlet and outlet temperature of the pre-heater section while also acounting for losses and added heat. This information together with the correlations describing the heat capacity of the fluid leads to the mass flow rate as shown in 4.2[77]:

$$\dot{m} = \frac{\dot{Q}_{heaters} - \dot{Q}_{losses}}{C_p(T_{pre-heater,out} - T_{pre-heater,in})} \tag{4.2}$$

The current design is unable to do this measurement continuously due to the lacking of a permanent thermowell at the entrance of the pre-heater. By using the moveable internal thermowell of the reactor this thermowell can be mimicked allowing for this method to be used. Not every experiment has made use of this method due to other temperature measurements taking higher priority, and the relatively late attempt at making use of this method. However by making use of this method the results that are obtained can be compared one-to-one with the work of Vroegindeweij since the methodology is identical. This also allows for the evaluation amongst the other two methods and indirectly to the work of Vroegindewij. The thermal losses of this section are assumed to 1/3 of those indicated for section 2 in figure 4.23.

4.1.2. Mass rate - Results

Evaluating the mass flow rate of the experiments the same qualitative behaviour is observed for all: the initial mass flow rate which is about a factor 2 higher than the mass flow rate at the end of an experiment as can be seen in figure 4.7. This initially high mass flow rate is attributed to the driving forces within the reactor being at their highest point during start-up of the reactor. The condenser and heat exchanger are still completely cold while the reactor bed wall heaters are already at their set temperature which lies in the range of 190-230 °C. Due to the heating of first the heat exchanger and later the condenser the driving force gradually decreases and thereby the mass flow rate. When steady state has been reached (evident by near constant temperatures) the mass flow rate keeps showing a decrease in mass flow rate albeit at a much slower rate than during start-up as can be seen in figure 4.7.

This decreasing effect is attributed due to heating of unmeasured sections of the reactor which are known to heat up slowly. These are identified as the closure system for the reactor bed, and the 25 mm Swagelok connectors at the condenser section. This behaviour is best visible in the differential pressure sensor data, but the trend is also somewhat visible in the mass flow rate results based on the lumped pre-heater method. This is not visible in the pre-heater results based on the open systems approach due to the non-continuous nature of the measurements.

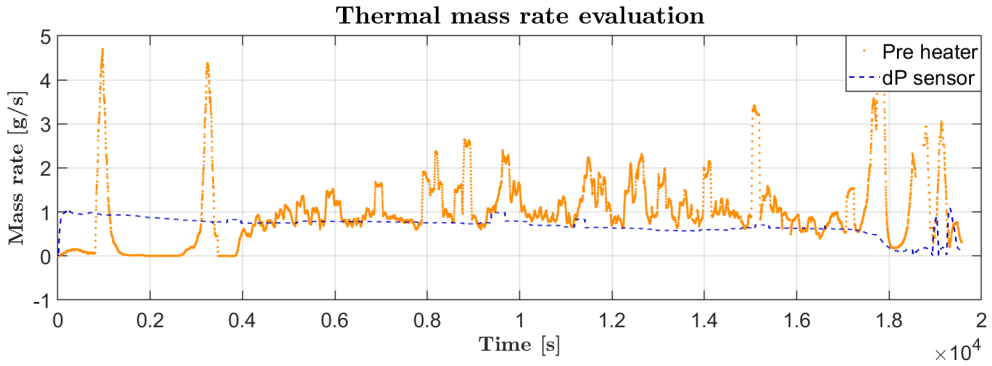

Figure 4.7: A typical output for the mass rate evaluations.The decreasing nature of the mass flow rate can be seen in both evaluation methods. Note that until t=4000 s the pre-heater is not being used, and therefore the mass flow rate before that point may be ignored. At t=15000s shutdown is initiated and events beyond that point should therefore also be ignored.

Results Evaluation

In general mass flow rate calculated through the differential pressure route has a more steady signal and has a lower value compared to the pre-heater based mass flow rate. Both signals generally lie within a factor of 3-0.1 each other and thereby also give the possible range in which the mass flow rate value might actually lie. Which is confirmed by the spot checks using the Vroegindeweij method. The pre-heater method is discontinuous due to the heaters cycling between heating and cooling. Likely this causes the observed oscillations in the signal. The mass flow rate of the differential pressure method is generally more trusted due to its continuous nature, giving seemingly reliable data over the entire operation regime of the reactor, and being based on very thoroughly evaluated correlations. The thermal correlations of the pre-heater are suspected to be somewhat inaccurate due to these being based on Kern's method as also discussed by Vroegindeweij [1]. This method is based on much larger heat exchanger designs possibly giving inaccuracies for the in comparison relatively smaller pre-heater. Furthermore the positioning of the inlet to the pre-heater can change when the reactor closure system is opened during a catalyst bed change. This likely also alters the heat transfer behaviour slightly compared to the correlations, and causes a measuring error in the mass flow rate. Therefore the mass flow rate of the differential pressure sensor is judged to be the most accurate, and will be used for the thermal and production evaluations in this work. The average mass rate between start and end of steady state is used for evaluations where only a single value is given such as point evaluation and bar charts. These average values can be found in table 4.1

Table 4.1: The experimentally found mass rates, and mass rate according to the simulation. The mass flow rate generally exhibits a decreasing behaviour, therefore the + indicates the mass flow rate at steady state and the - at the end of the specific experiment. It should be noted furthermore that due to the strongly oscillating nature of the pre-heater based values that these are local averages taking at the evaluation points.

Setpoint pre-heater [°C]	**Fan** [-]	**Catalyst size [mm]**	$+\dot{m}_{dP-sensor}$ $[g \cdot s^{-1}]$	$-\dot{m}_{dP-sensor}$ $[g \cdot s^{-1}]$	$+\dot{m}_{pre-heater}$ $[g \cdot s^{-1}]$	$-\dot{m}_{pre-heater}$ $[g \cdot s^{-1}]$	$\dot{m}_{sim}$ $[g \cdot s^{-1}]$
215	No	6x5	1.0	0.49	1.9	0.55	0.98
220	No	6x5	0.79	0.58	2.3	0.64	1.03
230	No	6x5	0.83	0.31	0.61	2.2	1.12
215	Yes	6x5	0.81	0.84	0.75	1.5	1.08
220	Yes	6x5	0.87	0.44	0.54	1.4	1.09
230	Yes	6x5	0.82	0.47	0.5	1.5	1.11
215	No	6x2.5	0.87	0.80	1.4	1.6	0.98
220	No	6x2.5	0.87	0.80	1.6	1.9	1.01
230	No	6x2.5	0.88	0.72	1.7	1.6	1.02
215	Yes	6x2.5	0.79	0.67	1.6	1.5	0.99
220	Yes	6x2.5	0.89	0.67	1.6	1.1	1.00
230	Yes	6x2.5	0.73	0.68	1.6	1.8	1.02

One possible explanation for the overestimation of mass flow rate using the lumped pre-heater method could be that the heaters are not uniform in temperature as can be seen in figure 4.8. During the shutdown of an experiment the pre-heater was accidentally left in the power on mode. This caused significant overheating of the pre-heater to the point where the metal tubes housing the heaters discoloured. Due to the discolouring being non-uniform it can be stated that it is likely that the heaters present a non-uniform temperature field. This could be a reason why the pre-heater based mass flow rates deviate since the heater area has a non-uniform temperature violating an essential assumption in the lumped thermal capacitance model.

Figure 4.8: The preheater after the overheating incident in which the heater attained an indicated temperature of 600 °C. Note that the yellowish discolouring of the steel indicates where the heaters have reached very high temperatures. Since this is non-uniform it can be stated that the heaters are not uniform in heating.

When assuming the dP-sensor based mass flow rates as the most accurate experimental results withs a typical range of 1-0.73 g/s at the start of an experiment and 0.31-0.67 g/s at the end of an experiment. It should be noted that the mass rate measurements of the 6x2.5 mm cat size are combined experiments meaning the fan was off and on during one experiment with the fan off during the first leg of the experimental run. Therefore the decreasing effect is possibly part of the mass flow rate results, and the starting values of the fanned results might actually be higher. Nonetheless all experiments show a decreasing nature with the final mass flow rate being a factor of 0.9-3.2 lower. This decrease is attributed to residual heating of large steel masses in the reactor (condenser coupling and reactor sealing system) which destroy the temperature driving force. The most interesting observation to make here is that regardless of using a fan or smaller catalyst the mass flow rate remains nearly the same for most experiments. This seems to indicate that the determining factors of the mass flow rate are of such magnitude or nature that these experience little effect of a colder condenser or smaller catalyst. The condenser will be treated more in depth in its own section, but it can be stated that it is always able to release all heat present.

Therefore the condenser functions at a nearly constant low temperature for all experiments giving a constant cold sink temperature and thereby little variation in mass flow rate . Due to the decreasing of the catalyst size having little effect it can be stated that using a smaller catalyst makes no difference for the reactor in terms of mass flow rate. This is an important result since generally a smaller catalyst has a higher effectiveness boosting STY.

Model validation - mass flow rate

Comparing the simulated and experimental mass flow rates based on the differential pressure measurements shown in table 4.1 deviation is evident. The values differ a factor of 1-1.5 with the biggest differences being seen for the mass flow rates measured at the end of the experiments. This gradual decrease in mass flow rate in the steady state region is not simulated by the model. The experiments do however show this gradual decrease, and as indicated earlier is attributed to gradual heating of high mass metal sections of the reactor. These sections are modelled in the model as a lumped mass, but the heat transfer coefficient is likely too optimistic.

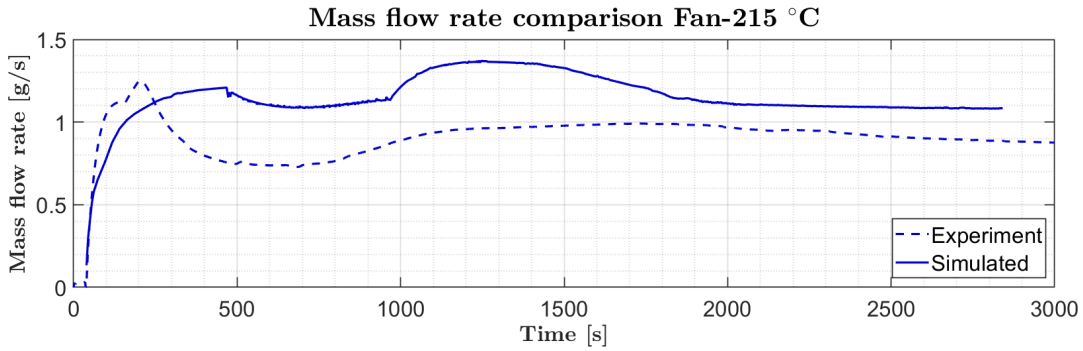

Figure 4.9: The first hump seen between 0-500 seconds is when the pre-heater has its highest power input for both cases. The second hump seen between 750-2000 seconds for the experimental and 1000-2000 seconds is due to the wall heaters being switched in temporally increasing mass flow rate. Note that the experimental heating algorithm indicated at the start of the chapter was used here.

The start-up region of the reactor is modelled relatively well in a qualitative sense as can be seen in figure 4.9. The initial peak due to the high driving force difference between a cold condenser and hot pre-heater is more evident in the experimental data. It seems to indicate that the driving force decreases faster in the experimental case. This could be due to modelling errors on how quickly certain structures heat up, or not simulated flow phenomena having adverse effects. These adverse effects could be local mixing behaviour of the flow due to uneven temperatures at for example the reactor bed surface.

The second jump in mass flow rate due to the start of the wall heaters is more prevalent in the simulated data. It seems to indicate that the heat transfer correlations for the reactor bed and the pre-heater require refitting. This is likely the case due to the correlations being used are fitted for axial flow beds and larger heat exchanger designs.

Figure 4.10: In the picture the bottom of the reactor bed can be seen, and the partial blocking of its entrances due to catalytic pellets. All of these effects cause a significant increase in pressure drop which is not modelled in the model.

The suspected core reason for the deviations in the mass flow rate between model and experiments is to be due to a misjudgement of the model of the external reactor bed pressure drops. The pressure drop correlations for the tubes are not suspected to be the cause since the Chruchil/Darcy Weisbach formula are very thoroughly developed. The correlations of the pre-heaters likely contain some deviation (Kern's method as set out earlier). However it is deemed that these deviations are not of such magnitude as to cause a halving in the mass flow rate. Vroegindeweij also noted deviations in mass flow rate between model and reality, and attributed these to be due to inaccuracies in the Kern equations but did no see differences of such significance [1]. Minor losses due to bends are evaluated to cause a pressure drop of a 1-10 Pa (on a pressure drop totalling generally in the order of 200-500 Pa) and should be added in the next generation of the nodal model. However one of the main reasons for the misjudgement in mass flow rate is suspected to be due to an inaccurate modelling of the external pressure drop of the reactor bed. The pressure drop over the reactor bed is modelled by an integration of the Ergun equation over the flow field, and this might be beyond the application range of the equation.

Besides possible errors in the Ergun equation usage for the bed also other losses in the bed are suspected to cause the deviation between model and reality. The reactor bed contains beside catalyst pellets also an inlet and outlet screen to keep the catalyst in place. Especially the inlet screen of the bed has a relatively poor porosity as can be seen in figure 4.10. It is expected that this causes a significant pressure drop which the model currently does not model. The catalyst is also observed to partially block the inlet which likely increases the pressure drop even further. Also the model assumes perfect flow which is unlikely since a partial chaotic flow is highly likely. As can be seen in figure 4.10 the catalyst is relatively coarse compared to the size of the bed, and some deviations in flow are therefore likely increasing the pressure drop over the bed in physical world. Also as shown in figure 4.10, a section of the reactor bed does not allow flow to pass. This likely causes flow instabilities due to this blockages which can further increase the pressure drop over the reactor bed. Combining this information it is highly likely that the deviation of the model is due to maldistribution of pressure drop evaluation over the reactor bed, and this should be improved.

Findings - mass flow rate

1. **The mass flow rate measurements of the differential pressure sensor and pre-heater based methods are generally within a factor of 3-0.1 of each-other.**
2. **The differential pressure method is seen as the more accurate as it is being based on fewer parameters, and the correlations used are seen as significantly more accurate.**

3. **The mass flow rate predicted by the model is an overestimation of a factor 1-2 depending on the experiments and time point. The underlying reason is wrongful prediction of the pressure drops of the pre-heater and heat exchanger (Kern's method), and the reactor bed. More advanced simulation studies are advised as well as design measures to ensure homogeneous flow through the reactor bed.**

4. **A decrease in mass flow rate is observed during experiments and is attributed to residual heating effects in the reactor.**

4.1.3. Flow stall/reversal

One of the great challenges towards autonomous operation is the effect known within ZEF as 'flow stall'. As shown in chapter 3 and the work of Vroegindeweij it is the effect when the mass flow is significantly reduced or stopped by the flow of hydrogen against the normal flow direction [1]. Flow stall behaviour in the work of Vroegindeweij could be discerned as a sharp drop in temperature and production [1]. During the first experiments the H_2 feed line was connected at the catch tank (the collection basin as shown in figure 3.11) in accordance with the case III method as shown in chapter 3 in figure 3.10. During these experiments the following was observed:

1. After initial heating the reactor pressure starts decreasing despite still heating up. With the reactor bed at a temperature where methanol synthesis is possible this effect is attributed to methanol synthesis occurring.

2. After a short period (10-20 minutes) of feed gas consumption the pressure of the reactor equalises and more feed gas consumption occurs. This indicates that the reactor bed is no longer producing methanol.

3. The condenser showed 'flipped' behaviour. With flipped it is meant that the outlet of the condenser has a significantly higher temperature than its entrance. This shows in theory that the reactor was flowing in the opposite direction of what is intended. The differential pressure sensor seems to indicate that flow was occurring the reactor, and doing so in a reverse fashion.

4. After shutdown of the reactor the reactor bed closure system was opened and a significant pool of fluid (estimated at 50-100 ml) with a foul smell was observed at the pre-heater section (before the reactor bed). The catalyst was drenched in this fluid, and was swapped since fluid can significantly damage the catalyst.

Summing up the above observations it seems that the reactor had been flowing in reverse direction. Especially the entrapment of fluids between the preheater and reactor bed, and the clogging of the heat exchanger tubes with fluid are strong indicators. Also the flipped behaviour of the condenser is a strong indicator, but can also be a sign of a still heating up reactor (start-up phase). The flow reversal was initially expected to be due to only the usage of the pre-heater and band heaters in inusion. It was hypothesised that heated gas could also escape to the tube exit of the heat exchanger through the connecting 25 mm tube to the reactor bed. After using only the wall heaters for heating it was found flow stall/reversal still occured. Since this heating method should have a much lower chance of causing such behaviour the hypothesis was assumed to be wrong

The next major suspected cause was that the mixing method of case II as can be seen in figure 3.10 was not working as intended. Since the exit of the condenser is also the wall for this mixing chamber the potential for H_2 entering this exit through the metal gauze is probable. Therefore the injection system of H_2 was switched over to method III and the normal start-up procedure was followed. No flow stall or reversal was observed and the reactor operated as was intended in terms of flow behaviour. No further stall or reversal has been encountered since, and the system shows great resilience against large volume injections of H_2.

Findings - Flow Stall

1. **Using injection design case III as can be seen in figure 3.10 it is possible to cause the reactor to flow in reverse. This is highly undesirable behaviour since it will damage the catalyst, and causes liquid to accumulate before the reactor bed and inside the heat exchanger tubes.**
2. **The clogging of the heat exchanger cannot be alleviated without overhauling the reactor bed and flushing the reactor with high pressure N_2.**
3. **Using injection design case III no flow stall or reversal were encountered during this thesis. The system also shows to be unaffected by large volume H_2 injections.**

4.1.4. Composition tracking

The used composition control method has shown it is able to keep the composition generally in relative proximity of the required set point of a molar fraction of 0.75 of H_2 at the inlet of the reactor bed. This is desirable since the reactions are known to operate most efficiently at a SN=2 which is equivalent to a 0.75 molar fraction of H_2. Changes of a fraction below 5 % are not discussed since these are within the range of the measuring error of the used set-up (based on the work of [1]). No composition runaway was encountered, and deviations of the composition usually indicated an underfeeding of H_2. This wandering behaviour of the composition can be seen, and especially in the case of the fanned 215 experiment as shown in figure 4.11. For this the following is deemed likely as the root cause:

- The geometry of the reactor bed differs between the 215(F), 215D, and 215S sets of experiments (the differences are shown in the section on the reactor bed). It is possible that the reactor geometry has influence on how the reactants are consumed. More specifics are giving in the reactor bed section, but for now it is sufficient to state that the 215D and 215S bed geometries have measures which likely make these geometries consume reactants at a more constant/predictable rate.

The trends shown here are also prevalent for the other set points, but no clear distinction can currently be made between the gas bottle and bed geometry effect. The first cause can be easily tackled by using a PID based heating system for the CO_2. If this shows to solve the drifting of the composition despite control the cause can be identified to be due to the CO_2 gas bottle pressure. However the effect of the reactor bed geometry design will be shown to affect production values and thus directly reactant consumption.

Therefore it is deemed likely by the author that at least to some degree composition control is influenced by reactor bed geometry design. In order to evaluate these effects a combined approach should be taken: a stable consuming reactor geometry is vital, and the sampling rate of the composition tracking algorithm should be significantly increased. This last advise should be exercised with caution since it means reactants are lost to the environment on a more frequent basis.

Figure 4.11: Measured composition during experiments at the set point of 215 °C. F means an experiment where the fan was on, D refers to a certain reactor bed configuration discussed in the section of the reactor bed, and S means a smaller size catalyst was used. Deep sudden drops should be ignored since these are caused by sensor malfunction and are cleared by the operator.

Findings - composition control

- **The cascaded-PID control is able to prevent composition runaway, and keeps the reactor at a relatively advantageous composition during experiments. This advantageous composition contains a molar fraction of 0.75 H_2 amounting to SN=2.**
- **Instabilities in composition are attributed to: reactor geometry, it seems to play a part in how stably reactants are consumed and thus how predictable the reactor consumption is. It is advised to take this effect into account in future reactor bed designs. Also a sampling rate increase could aid in alleviation of these effects.**

4.1.5. Additional finding - Flow phenomena

The nodal model is in essence a 1-D model and therefore unable to predict any 2 and/or 3-D flow phenomena. All sensors within the reactor are point sensors and therefore are also unable to accurately capture these 2 and/or 3-D flow phenomena. However, looking at their responses being influenced by these phenomena, it is still possible to indicate the presence of possible multidimensional effects occurring within the reactor.

Falling gasses

During the start-up phase of the reactor only the wall heaters heat the reactor bed. This causes a temperature difference between the preheater section before and the wall heaters which can be in the order of 0-150 °C. The sensors placed after the pre-heater and before the reactor bed show a gradually increasing line. However oscillations are observed in this temperature range and generally near the end of the start-up phase. These oscillations are suspected to be due to local flow phenomena in which the heated gas travels from the reactor bed past the sensor due to local instabilities. It might be the case that this is due to as section of the reactor bed being blocked.
Due to this blockage section hot gas comes to a standstill and might travel back in the reactor. No definitive answer can be given currently to the exact mechanism occurring. However it does show that local mixing effects are taking place at the reactor bed inlet, and likely local heating effects are taking place as well. An understanding of these effects could be beneficial in further understanding the performance of the reactor bed.

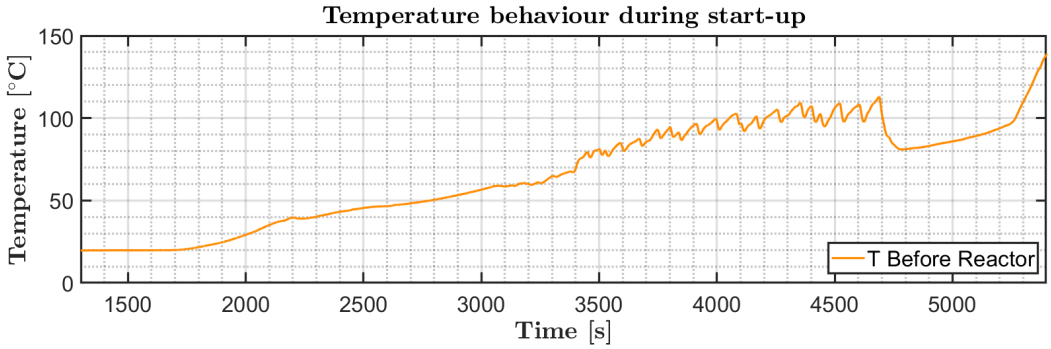

Figure 4.12: The oscillations in the thermowell before the reactor bed (TBR) during start-up. The oscillations are suspected to signify the mixing of hot and cold gasses and thereby possibly indicate multidimensional flow effects. In this case the reactor is started at around 1500 seconds and the onset of methanol synthesis is seen at 5000 seconds (based on temperature profile of the reactor bed not plotted here).

Start of flow

Start-up shows more interesting behaviour than only the possible mixing of gasses at the entrance of the reactor bed. During start-up the temperature before and after the reactor bed initially climb in unison. After a period of time the temperature before the reactor starts climbing at a slower rate than the temperature after the reactor while no exothermic reaction is occurring. It is suspected this is the point that the flow start to develop to a significant amount. It is hypothesised that before this onset no flow occurs to a significant extent and that the section before the reactor bed fills with increasingly heated gas. When the driving forces are sufficient the gas starts flowing through the reactor bed, and thereby the temperature climb of the senors before the reactor bed decreases significantly since no gas is accumulating before the reactor. This type of behaviour is currently being investigated through CFD work at ZEF, and seems to confirm this notion. Although no certainty can be given this effect actually occurs it is strongly suspected to do so. An understanding of this effects could perhaps aid in indirectly measuring the pressure drop of reactor bed designs.

Findings - Flow Phenomena

1. **It is suspected that local flow phenomena occur at the reactor bed inlet during start-up. These phenomena are seen as oscillations in the temperature sensors before the reactor bed. It is hypothesised these cause local mixing effects, but no definitive answer can be given.**

2. **During the start-up phase it is noticed that the temperature sensors before the reactor bed suddenly stops increasing in temperature at the same rate as the sensor after the reactor bed. It is suspected this is due to an initial build up of driving force before significant flow occurs through the reactor bed. No definitive answer can be given, and more research is required.**

4.2. Reactor Bed

One of the main aims of this work is the development of a more STY efficient reactor bed for the reactor. The bed should allow for:

1. A higher fraction of catalyst mass being at a certain advantageous temperature. Generally this temperature is as low as possible while maintaining relative fast kinetics.

2. An advantageous residence time vs temperature relation; positions in the bed with a higher residence time generally also have a lower temperature.

3. It allows for a smaller catalyst size for a certain pressure drop. This allows for higher catalyst effectivity and a higher limited mass flow rate.

The characterisation/evaluation of the reactor bed is done through 4 experiments witch each of these performed at three set temperatures (215, 220, 230 $^{\circ}\mathrm{C}$). The four cases are shown as the right lower leg in figure 4.1, and are the following:

1. **Base Case** The reactor is run in the configuration it was designed, and the catalyst bed is fully filled with whole JM catalyst pellets for a total catalyst mass of $\mathrm{m_{cat}} = 584$ g. These experiments are seen as the base case, and all other experiments are related to this base case as either improvement or degradation. The main aim is to evaluate the performance of the bed in terms of its design criteria and the modelling of the bed.

2. **Increased Mass Flow** During these experiments the condenser will be actively cooled by a radial fan. This causes a lower temperature of the condenser due to the increased cooling and this colder condenser will increase the mass flow rate due to the increased driving force. The aim is to evaluate how the bed performs at a different mass flow rate regime, and should yield information on which mass transfer mechanism is likely limiting in the bed.

3. **Flow Behaviour** 1/3 of the reactor tube is left blind to allow settling of the bed and accounting for reduction in catalyst size during operation as indicated by [78]. However, during the first swapping of the catalyst bed after the flow reversal incident it was found that the catalyst did not decrease in size. This caused the hypothesis that 1/3 part of the bed is filled with catalyst with no effective outlet causing the build up of product. These will travel to the opening in the bed causing flow mall distribution and also negatively influencing the chemical equilibrium in the bed. To evaluate this hypothesis 1/3 of the reactor bed was filled with inert crushed ceramic cooking beans as can be seen in figure 4.14. With a part of the bed made inactive the base case and forced convection flow regime were tested in three experiments: the set temperature was kept constant but after 2 hours of base case operation the fan was switched on for an additional 2 hours to evaluate the effect of the fan. The aim is to understand how the flow in the reactor bed behaves, and to indicate if the inner tube design needs to be altered. The total catalyst mass used was $\mathrm{m_{cat}} =$ 455 g

4. **Reduced Pellets** One method to boost the STY is to reduced the catalyst size if diffusion limitations are occurring. Since it has been shown in the previous chapter as well as the work of Vroegindeweij [1] a set of experiments is performed with reduced catalyst size. The bed design is known to have a small pressure drop, and therefore a decrease in catalyst size is expected to have a significantly lower decrease in pressure drop. The catalyst pellets were halved in size since smaller catalyst pellets could not be obtained within the time frame of this work. The main aim is to understand the significance of the diffusion limitations and what the impact of the increased bed pressure drop is on the reactor. The total catalyst mass used was $\mathrm{m_{cat}} = 359$ g, note that different catalyst was used for this experiment due to short term availability and that this type of catalyst allowed for more uniform reduction in size. It is known that this catalyst has an STY performance about 5-10 % lower and this should be held in mind when reviewing the experimental results.

Figure 4.13: The reactor bed during production. Note the long thin thermowell probe running though the centre. Furthermore note the partially blockage at the left to account for catalyst shrinkage

Figure 4.14: In the left image the catalyst and ceramic pellets can be seen after experiments, note the slight reddish colour to the some of the catalyst still being in its reduced state. In the right image the reactor bed as used can be seen. Note that first section of the bed being filled with the white colour ceramics which corresponds to the section of blockage as can be seen in figure 4.13.

4.2.1. Sensors

The temperature sensors (Tegg NTC 3950 100K ($\pm$ 1 °C)) placed in and around the catalyst bed are the following:

1. **TBR** Stands for Temperature Before Reactor and is the thermowell sensor placed before the catalyst bed. This is the sensor which acts as the temperature setpoint for the experiments, and PID-control of the pre-heater and indirectly the wall heaters.
2. **TAR** Stands for Temperature After Reactor and is the thermowell sensors placed after the catalyst bed directly above the outlet of the bed.
3. **Tc Reactor** Stands for Thermocouple Reactor and is the moveable thermocouple (SYSCAL Type K + 1100 °C 1.5 mm diameter) placed within the catalyst bed. When not doing measurements along the bed the sensor is held high up in the reactor to evaluate temperatures at the blind section.
4. **T Wall Heaters** Stands for Temperature Wall Heaters, and is the temperature of the controlled wall heater. Effectively this signifies at which temperature a part of the walls are being held.

Initially more temperature sensors were present on the wall of the reactor in order to understand the temperature distribution on the inlet of the reactor bed. This consisted of a group of 4 NTC places between the 3 wall heaters which each have an internal thermocouple aswell as can be seen in figure 4.15.

Figure 4.15: The temperature wall sensors placed on the reactor wall. The gray block are the heaters which each contain a internal thermocouple. The NTC are placed within the orange Kapton tape patches and are placed between the heaters. The wall heaters are placed directly above the inlet section of the reactor bed. The thermowell seen in the lower left is TBR (Temperature Before Reactor).

Unfortunately 2 of the wall heater thermocouples and all of the NTC had to be taken out of function due to damages to these sensors. The lead of the thermocouples of the wall heaters were found to be too short and had to be lengthened by soldering extra pieces of wire to them. These solder joints were apparently insufficient since signal was lost immediately on one of these heaters, and halfway through the experiments also on the second one likely due to damage received during catalyst bed swapping. The NTC's isolation was not resistant to the wall temperatures experienced and likely have melted. Due to the melting the two wires which form a NTC came into contact and shorted the entire PCB system. Although only one NTC was shorted during the finding of this issue all others were also disconnected to preserve the PCB.

4.2.2. Evaluation

Ideally the new reactor bed should give an increase in STY and allow for the usage of a smaller catalyst size than in case of the previous design. The underlying reasoning has been given in the reactor bed review in chapter 2 and reactor bed design in chapter 3.

Up until this point in the evaluation of the experimental results little attention has been paid to the transient behaviour of the reactor. This is mainly due to most processes following the transient behaviour of the reactor bed. In figure 4.16 typical start-up behaviour for two cases is shown. Note that the experiments were started at different points and hence the start-up behaviour appears to be non-synchronous. During the start-up phase of the fanned experiments the fan was not on due trepidation of causing a flow stall when cooling the condenser too much during start-up. Therefore the start-up sequence for both graphs has been identical, but there is distinct difference in the start-up as can be seen from the graphs. This is attributed to the reactor taking longer to heat up in the case of the slower start up as seen by the Fan-220. It is evident that the wall heater heats up in an identical manner, and therefore the following hypothesis was explored:

1. It can be seen that in the case of short start-up times the internal temperature is significantly higher, and the characteristic jump in temperatures of TAR due to exothermic reaction starting cannot be seen. Also it seems that less local flow phenomena occurred due to the less jittery nature of TBR in case of a quicker start-up time. Therefore it is suspected that the heating of the reactor bed and/or local conditions of the bed where such that exothermic reaction occurred earlier in the case of the quicker start up. Likely this is due to some sort of local flow phenomena occurring in the bed which has not been captured by the sensors.

Comparing the current start-up time of the reactor with the previous design it can be seen that the current design is significantly slower. Where the previous reactor could start-up in roughly 20 minutes the current design usually exceeds the 1 hour mark from moment heaters are turned on. It is shown in the heat exchanger section that as soon as the reaction start to occur the reactor reaches steady state relatively quickly. Therefore the main reason behind a long start-up time is the slow heating of the reactor bed. It is suspected that this is due to the catalytic pellets who are insulated from the hot walls by an air gap as can be seen in figure 4.10.

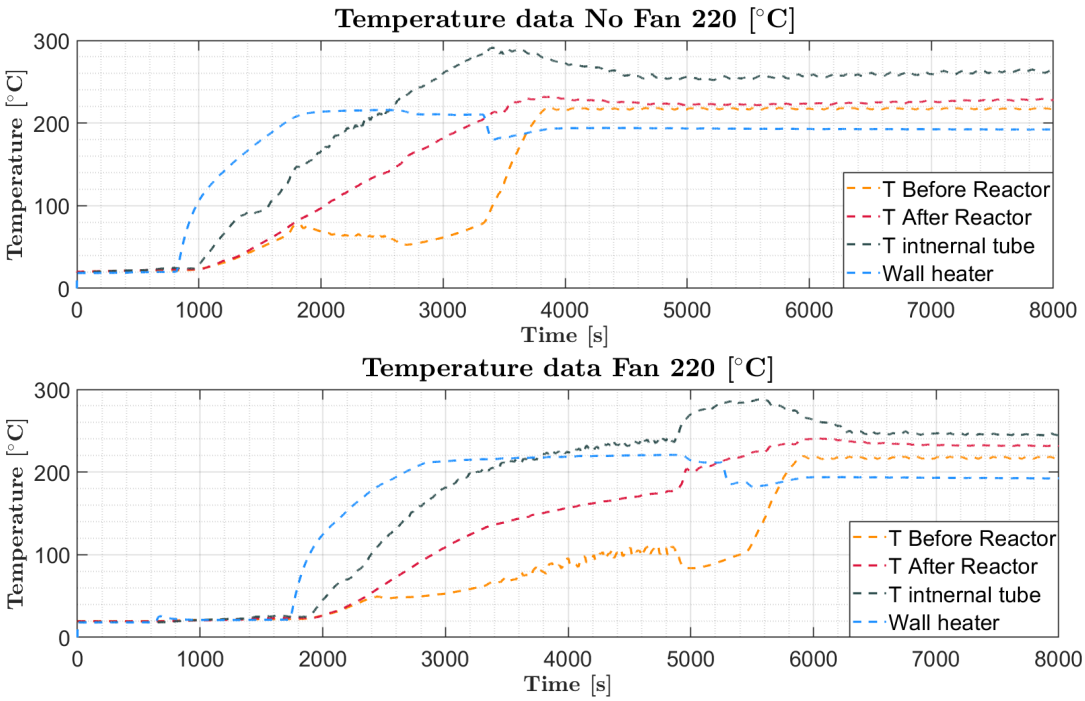

Figure 4.16: An example of temperature outputs in case of a pre-heater setpoint of 220 degrees °C. The top graph is the base case indicated as No Fan-2002 while the bottom graph is from the forced convection experiment in which the condenser was cooled by a radial fan.

Furthermore as has been shown this gas moves around in propably chaotic fashion as has been seen in figure 4.12 (the local flow phenomena witnessed/falling gasses) which means that not all heat is transferred to the reactor bed. This is problematic since such long start-up times can significantly hamper in dynamic operation of the microplant. Therefore a future design should contain measures to alleviate this. This can be through multiple routes such as conductive structures to the wall or local cartridges heaters within the reactor bed. Especially the later option is interesting since a design could be made in which a hybrid reactor bed pre-heater design is made. This would decrease the part count, and furthermore increase mass flow rate. As long as the bed is designed to not be limiting at a higher flow rate a higher production and thus STY can be reached.

Comparing the transient behaviour of the model versus the experiments the local differences between experiments also seems to apply. The heat transfer is being misjudged by the model significantly as can be seen in figure 4.17. This can be attributed to the correlation being used being inappropriate for modelling the heat transfer to the reactor bed, and the lower value of the mass flow rate in the experimental case. Experimental refitting is likely the quickest route although fitting to CFD results could also be an option.

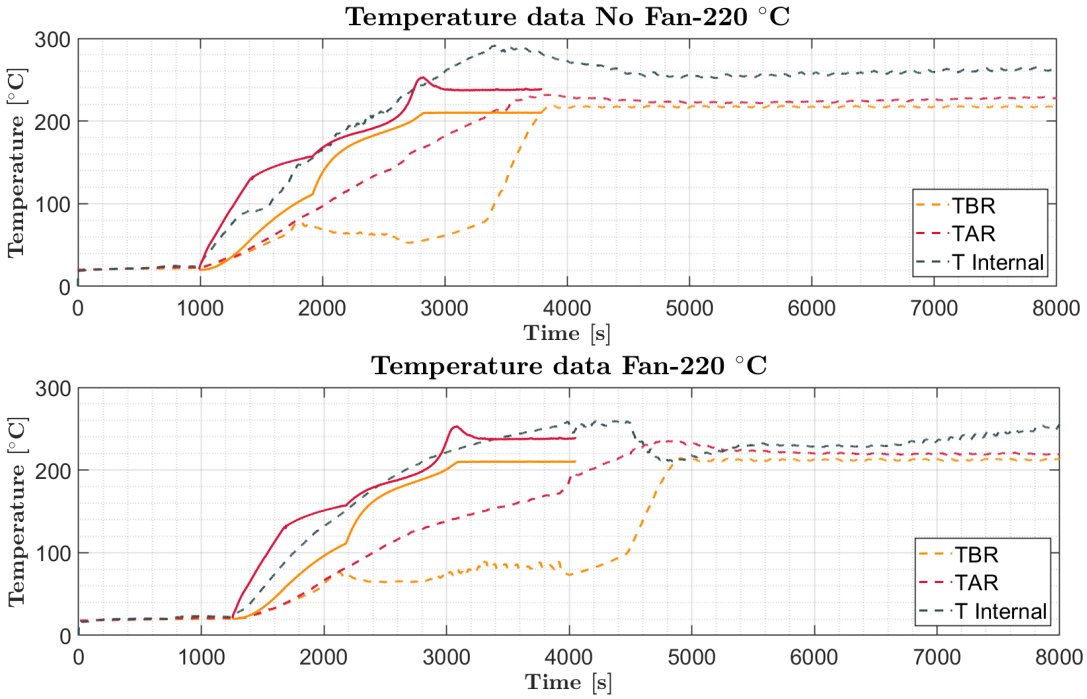

Figure 4.17: The modelled transient behaviour of the reactor, and the experiment using the same set point temperature. Dotted lines indicate experimental values while solid lines indicate simulated values.

When evaluating the steady state region of figure 4.16 which are exemplary for the other experiments it is evident that the temperatures after the reactor are different. Generally the temperature of TAR at the outlet of the reactor bed is lower compared to the internal thermowell in the outlet tube is. The TAR outlet is suspected to be some sort of mixed gas temperature and will be discussed in depth in the heat exchanger section.

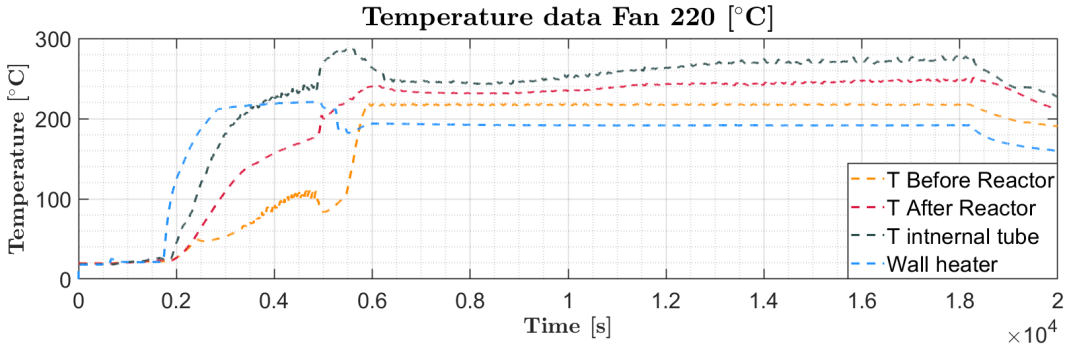

Figure 4.18: The temperature output for the transient and steady state behaviour of the reactor for an inlet temperature setpoint of 220 °C.

When comparing TBR to TAR it seems that the reactor is performing close to isothermal regime. However as discussed earlier the values of TAR are less an indication of the outlet temperature than $TC_{internal}$ is. This was noticed early on in the experiments, aswell as the effect that in the the blind section the highest outlet temperature is reached according to the internal thermowell as seen in figure 4.19. This higher temperature is seen as the true outlet temperature due to it being situated directly at the outlet of the bed. Using this temperature as the true outlet temperature it can be seen that the reactor bed does not perform close to the isothermal regime.

Table 4.2: The obtained experimental and simulation results. Note that the letter D means the top section of the catalyst bed at the blind inner tube is inactive. The model is currently unable to account for these effects, and the comparison between production is therefore not shown. NM indicates Not Modelled due to the model being unable to model flow maldistribution effects. - indicates production values are not taken directly into account due to dissimilar catalyst weights. Note that for all simulations a catalyst mass of 597 g was used.

Setpoint pre-heater	**Fan**	**Catalyst size**	$\dot{m}_{avg}$	**TBR**	**TAR**	$TC_{internal}$	**Prod.**	**STY**
[°C]	[-]	**[mm]**	$[g \cdot s^{-1}]$	[°C]	[°C]	[°C]	$[g \cdot h^{-1}]$	$[\frac{mmol}{g_{cat} \cdot h}]$
			Experimental || Simulated					
215	No	6x5	0.75||0.98	213||210	228||239	261||239	109||224	5.8||13
220	No	6x5	0.69||1.03	218||215	234||252	273||252	97||288	5.7||15
230	No	6x5	0.57||1.12	226||233	230||273	265||273	114||352	6.0||18
215	Yes	6x5	0.83||1.08	212||210	236||239	252||239	134||224	7.2||13
220	Yes	6x5	0.66||1.09	218||215	244||252	269||252	113||288	6.1||15
230	Yes	6x5	0.65||1.11	228||233	238||265	267||273	125||352	6.8||18
215D	No	6x2.5	0.74||NM	212||NM	215||NM	248||NM	92||NM	6.3||NM
220D	No	6x2.5	0.79||NM	217||NM	224||NM	260||NM	86||NM	5.9||NM
230D	No	6x2.5	0.69||NM	227||NM	228||NM	270||NM	113||NM	7.7||NM
215D	Yes	6x2.5	0.61||NM	213||NM	226||NM	251||NM	116||NM	8.0||NM
220D	Yes	6x2.5	0.62||NM	218||NM	246||NM	254||NM	118||NM	8.1||NM
230D	Yes	6x2.5	0.60||NM	228||NM	240||NM	275||NM	114||NM	7.8||NM
215D	No	6x2.5	0.84||0.98	213||210	212||240	240||240	74||-	6.4||12
220D	No	6x2.5	0.88||1.01	218||226	220||265	249||265	72||-	6.3||17
230D	No	6x2.5	0.80||1.02	228||234	231||272	267||272	74||-	6.9||17
215D	Yes	6x2.5	0.73||0.99	123||210	222|259	239||259	74||-	6.3||12
220D	Yes	6x2.5	0.78||1.00	217||219	228||257	254||257	74||-	6.5||16
230D	Yes	6x2.5	0.71||1.02	228||226	239||268	268||268	98||-	8.5||17

Figure 4.19: Axial temperature profile of the inner tube of the reactor bed.

Observing the STY data from the experiments presented in table 4.2 some interesting behaviour can be observed. Generally the STY is better during fanned experiments in the case a fully filled catalyst bed is being used. This is within line with the work of Vroegindeweij and is assumed to be attributed to an increase in mass flow rate [1]. It is important to note that all experiments making use of a reduced size catalyst (6x2.5 mm) are done using a different catalyst. It is known that this catalyst functions about 10 % worse compared to the catalyst used in the other experiments. The main reason for doing so is that the worse performing smaller catalyst could be cut more easily and uniformly in half cylinder shapes.

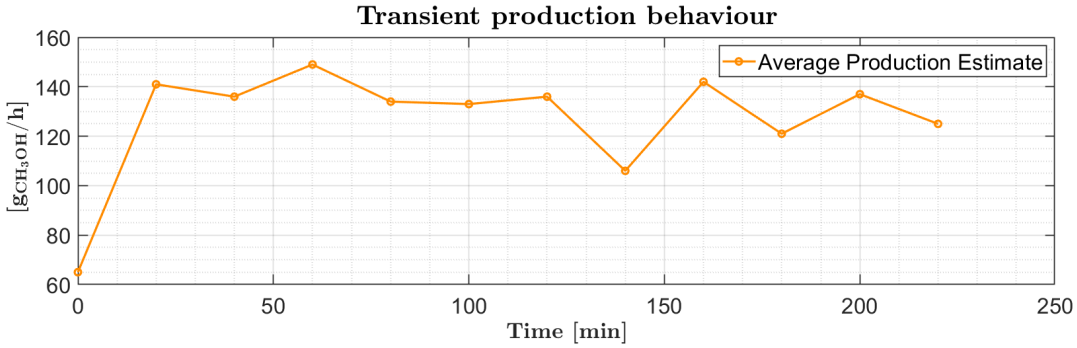

Figure 4.20: The production per hour based on 20 minute interval measurements (a circle means the point where the measurement was taken). Note that these measurements are started when the reactor is at steady state in terms of temperatures. This the t = 0 is actually from the point of achieving steady state. The production behaviour can be seen to be relatively constant.

The model significantly over-predicts the production of the reactor bed, and thereby the exothermic heat released to the reactor. The insulation will be shown in the thermal section of this chapter to likely perform relatively close to what is predicted by the model. The exothermic heat release is under-predicted by the model. This is identified as the root cause as to why the reactor cannot obtain autothermal operation during experiments. The deviations between model and reality are identified to be a combination of the following factors:

- **Mass flow rate:** This is being over predicted by the model. The over prediction is of the order of 1.2-2 and a lower mass flow rate means less reactants are present at each point in time to be converted. The underlying assumption is that the reactor bed is not being limited in terms of mass transport.
- **Extra particle mass transport:** The model assumes that the mass transfer limitations are inside the particle. This is based on the work of Vroegindeweij [1] in which increasing mass flow rate did not increase production. Since the relative high mass flow rate compared to Vroegindeweij [1] this was seen as an appropriate assumption. However during experiments it is found that production is relatively constant despite a decreasing mass flow as shown in figure 4.20. This is a strong indication some sort of mass transfer limitation is occurring. Therefore a study on possible external vs internal limitations is warranted and could be part of the proposed new modelling strategy.
- **Modelling strategy:** The current reactor model is the simplest option that can be possibly used. The core principles is a strongly simplified flow field, and assuming the entire bed as a single homogeneous solid. However looking at the size of the pellets versus the size of the reactor bed it is highly likely that a non-homegenouse approach is required. In this the gas and solid pellets are modelled as separate entities. Normally this is undesirable due to the size of reactors and thus the high computational load of such a model. However with the small size of the reactor this might be an viable approach. It is highly encouraged to make some sort of simple non-homogenous model. This allows to better model the following two important parameters which greatly effect the chance of optimizing the STY:

1. **Homogeneous flow:** The model assumes a homogeneous flow, but experimental data seems to suggest that this is not occuring. Furthermore the size of the catalytic pellets versus the path are within an order of 5 or less of each other. To be able to model these effects it is encouraged to make a model incorporating flow around spheres. Of course the route of a fully fledged CFD model can be used, but this would means discarding the nodal model which allows vital insights in the synergy of the many process occurring. Therefore it is proposed to make a sub nodal model within the nodal model to emulate the reactor bed. The flow network can than be tuned to model the local 2-D flow based on fluid flow correlations around spheres. The additional computational increase might be worth the additional insights gained.
2. **Internal heat transfer:** The model seems to model the heat transfer of the pellets relatively well as can be seen in table 4.2. However, this is based on a singular type of flow while this is assumed not to occur during experiments. Therefore currently no defining statement can be made if the modelling method works. However by using the sphere's based nodal model local heat transfer correlations for pellets can be used. There exist multiple correlations for this and therefore it is expected that the prediction of the heat exchange might also increase. Furthermore due to using a local heat transfer model in this new strategy, the option exist to model local external mass transfer rates thanks to the heat-mass transport analogue. Therefore by making this local model a fully fledged multiphysics model can be created while keeping the benefit of the nodal model (synergy and condensation modelling).

- **Inter particle mass transport:** The current model makes use of a Thiele modulus based sub model to predict particle effectiveness. The experimental data shows that deceasing particle size increases production at roughly the same mass flow rate. Therefore it can be stated that internal mass transfer limitations play a role in the reactor. When assuming for example the case of the setpoint of 215 °C shown in table 4.2 an increase in effectiveness when reducing catalyst size of 5 % is found. The case of 230 °C shows a large increase, and can be seen as an indication the effectiveness of the bed becoming higher. However due to the smaller pellets size it is also possible that a more beneficial flow field is occurring. Therefore currently no conclusion can be reached whether the Thiele modulus based model predicts accurately. However the model generally gives values as stated by industry and therefore is trusted. Furthermore it is well known that a smaller catalyst size negates diffusion limitations for the price of increased pressure drop. The bed used in experiments as shown in table 4.2 appears to not suffer form this increase in pressure drop, and therefore catalyst size reduction remains a viable path for the design.

The experiments using the inert material at the blockage section as shown in figure 4.13 of the bed yields interesting results as shown in table 4.2. The STY significantly increased meaning that likely the hypothesis holds. The hypothesis effectively states that: due to catalyst also being present at the blocked section during operation there is no means to release the produced methanol at the blocked section. The only option is through a section of the bed to where the it is open as shown in figure **??**. This is highly undesirable since this methanol concentration negatively impact the local chemical equilibrium in the bed. Furthermore due to the escape flow the flow in the reactor bed is disturbed which possibly further harms the performance of the reactor bed. The results indicate that this is the case which can be seen by the significant increase in STY. Further experiments using the catalyst pellets of a smaller size therefore also used an inert top layer. In future design the blockage can thus be significantly smaller since the catalyst size reduction is not as severe as predicted, and an oversized blockage section greatly harms the performance of the reactor bed. Besides proposing a new modelling strategy for the reactor bed a new design is also proposed. It is based around the following experimental findings:

- The experiments of using a inert section shows that catalyst always requires an in- and outlet. Furthermore it was found that the catalyst experiences little shrink thus the blockage section can be greatly reduced.
- Smaller catalyst improves STY and should therefore by kept in use.

The catalyst size should remain at the smaller catalyst size since the pressure drop increase has been shown to be non significant. This should ensure a more uniform flow, a higher mass flow rate, and give more heat exchange between the pellets.

Performance perspective

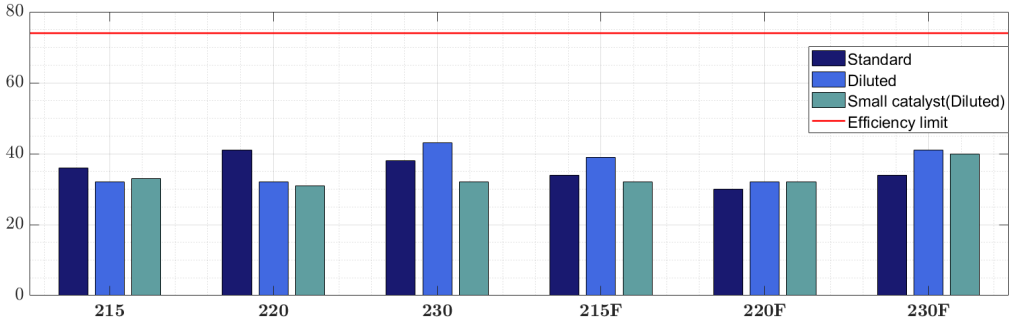

Figure 4.21: The obtained energy efficiencies for the experimental set. In which F stands for fanned experiments

An important possible characteristic is the autothermal operation of the reactor. Effectively this means that the released exothermic heat is sufficient to pre-heat all reactants, and no heater power is thus required. To evaluate how close a reactor is to autothermal operation the following equation is used [1]:

$$\eta = \frac{\dot{n}_{CH_3OH} LHV_{CH_3OH}}{\dot{n}_{H_2O} HHV_{H_2} + P_{heaters}} = \frac{\dot{n}_{CH_3OH} 0.6375 \cdot 10^6}{\dot{n}_{H_2O} 0.2856 \cdot 10^6 + P_{heaters}} \tag{4.3}$$

In the case of autothermal operation (no heater power) an efficiency of 74 % is seen [1]. It is evident from figure 4.21 that the reactor is not attaining the autothermal regime. As discussed earlier it is deemed to be mainly due to the reactor bed under performing. Due to the lower amount of exothermic heat released than designed for the input of the heaters needs to be higher to maintain the required bed inlet temperature. It will be shown that the heat exchanger, and thermal insulation perform relatively well. Therefore the main reason for the relatively low efficiency is due to the reactor bed significantly under performing to what has been predicted by the model.

Table 4.3: The performance of the initial concept as presented by Brillman and the previous ZEF reactor designs. Note that the chosen case (230FannedDilutedSmall) of this reactor has been based on the best STY reported. This means the lowest amount of catalyst weight used during experiments is presented here. Un identifies an unknown value.

	Brillman [31] [1]	Basarkar [24] [1]	van Laake [32][1]	Mishra [33][1]	Vroegindeweij [1]	230FSD
m_{cat} [g]	52.5	45	120	120	460	360
STY [mmol/g_{cat}h]	17	6.8	4.1	4.8	6.24	8.5
Y_{CH_3OH} [g/h]	28.4	9.8	16	18.7	95.9	98
$\dot{m}$ [g/s]	Un	0.046	0.41	1.1	0.313	0.71
$T_{bed,in}$ [°C]	180	Un	Un	205	213	226
$T_{bed,out}$ [°C]	200	Un	Un	224	238	268
$P_{Heaters}$ [W]	Un	64.8	125	156	38.5	135
η_{energy} [-]	Un	43.6	36.3	35.0	70.7	40.1

Comparing the current reactor design with the previous generations the increase in STY is apparent as can be seen in table 4.3. This increase is attributed to the usage of the new bed in which smaller catalyst could be used more effectively. The optimal temperature range is also somewhat higher which is in accordance with data presented in [43]. However the highly important energy efficiency has taken a nosedive with the current reactor. Effectively it means that the reactor is further away from being autothermal. The underlying reasoning is the under performance of the reactor in terms of yield, and this indicates that less exothermic heat is released than is designed for.

It is expected that with the new reactor bed design the efficiency values presented by Vroegindeweij can be reattained. This is expected since the new bed design should allow for a higher STY, and a higher yield. Furthermore this reactor follows the thermal design of Vroegindeweij to a significant degree meaning that the changes of reattaining the high thermal efficiency are high.

Findings - Reactor bed

- **The reactor bed performs significantly worse than predicted in terms of STY by a factor of 1.8-3. This is attributed to apparent external mass transfer limitations, lower than modelled mass flow rate, and a flow which has a significant axial component.**
- **Reducing catalyst size significantly increases STY by in the best case a factor of 1.21 without significantly decreasing mass flow rate. This can be due to an increased pellet effectiveness and/or due to having a more uniform flow due to increased pressure drop. Therefore using a smaller catalyst size is encouraged.**
- **The blockage section proofed to decreased the performance of the reactor bed in terms of STY. This is likely due to having adverse temperature and concentration gradient's caused by escaping flow in the reactor bed. Decreasing the size of this blockage section is possible since the catalyst is found to not decrease in size significantly during usage.**
- **In general the bed leads to an increase in STY beyond what was historically achieved at ZEF with the best STY performance being 8.5 mmol/g_{cat}h, and improvement of 21 %. It is felt by the author that if homogeneous flow, a high mass flow rate, and small catalyst are applied the STY can be boosted significantly.**
- **The thermal efficiency has decreased by a factor of 1.8 compared to the Vroegindeweij reactor. This is attributed due to the reactor bed releasing less exothermic heat than designed for. Due to the significant similarities in thermal design it is expected that with a better performing reactor bed design the energy efficiency of the Vroegindeweij reactor can be reattained.**
- **The modelling of the reactor bed is likely erroneous due to it being based on the homogeneous approach. Due to the dimensions of the pellets and of the bed involved a non-homogeneous approach should be followed. A strategy is indicated, and might aid in creating a better fitting model. However to achieve high modelling accuracy an experimental refitting is likely required due to the complex nature of the reactor bed. Therefore the modelling work might take the form of a half modelling - half experimentally fitted approach.**
- **The model for heat transport within the reactor bed might contain errors due to the complex nature of the heat transfer behaviour of the bed. It is felt by the author that an experimentally fitted equation will eventually be required. Up until that point adiabatic models should be used since these represent the worst case scenario, and any heat transfer likely improves the production estimation.**

4.3. Heat transport - Condensation Domain

Using the evaluated experimental values of the mass flow rate it is now possible to evaluate the condensing behaviour within the reactor. Condensation is a vital process since by condensing the products the chemical equilibrium is kept at an advantageous position at the reactor bed inlet. Furthermore the temperature of the condenser section acts as the cold-sink temperature for the natural convection in the reactor. In previous work by Vroegindeweij it has been shown that an on average lower condenser temperature leads to a higher mass flow which can cause an increase in product generation [1]. Besides evaluating how the reactor performs in the physical world it is also possible to evaluate how well the model is able to emulate condensation behaviour. By doing so it can be found which correlation is able to accurately capture the condensing behaviour and which correlation requires refitting/redefining.

4.3.1. Thermal losses

The insulation of the reactor has been carried out using a custom plastic mould in which loose stonewool is held as shown in figure 3.12. The main aim of using such a casing is to reduce the possibility of heat leaks between separate pieces of pipe insulation previously used. The insulation is made such that every part of the reactor has at least a covering of 60 mm of loose stonewool. Due to the the nature of the shape, a one-on-one analytical model does not exist. However, analytical solutions for conduction over cylindrical shapes do exist. Since the reactor itself consists of tubing which is covered by the stonewool to at least 60 mm these analytical formula (shown in the appendix on insulation) are seen as a good approximations of the complex insulation casing. These formula might overestimate the losses due to the connecting tube to the reactor bed and the reactor bed tube itself being held within the same casing. This decreases the exterior area for this section to exchange heat with the environment which should reduce the overall heat loss. The analytical equations used by the nodal model are the following [1]:

$$Q = \frac{\Delta T}{\sum R_i} = \frac{\Delta T}{1/UA} \tag{4.4}$$

$$\sum R_i = R_{gas} + R_{wall} + R_{insulation} + R_{air} \tag{4.5}$$

$$R_{wall,insulation} = \frac{\ln(r_o/r_i)}{2\pi k_i L_i} \tag{4.6}$$

$$R_{gas,air} = \frac{1}{2\pi r_i L_i h_{c,i}} \tag{4.7}$$

It should be noted that multiple uncertainties are present in the formula above and in the appendix. These are mainly the correlations for convective heat transfer and the conductivity of the loose stonewool. Convective heat transfer can be altered by for example the air flow of the fumehood. A convective heat transfer coefficient of 15 W/m^2K is used which was found to be appropriate by Vroegindeweij [1]. The conductivity of the stonewool is hard to quantify due to its loose nature and its susceptibility to the degree of compacting in the casing. Currently it is assumed to perform equally well in terms of conductivity as commercially available prefabricated stonewool pipe pieces. In order to evaluate the performance and discern between these uncertainties three methods are used in unison:

1. Lumped capacitance model: In order to evaluate the modelling of the insulation cooling curves as shown in figure 4.22 are used while ensuring no mass flow is occurring within the reactor. After an experiment (usually taking between 4-7 hours) the reactor is usually left at 20 Bar of pure H_2 to keep the catalyst in a reduced state. Due to the much lower pressure and density of the gas within the reactor the mass flow rate is significantly reduced. The differential pressure sensor data indicates that relatively quickly the mass flow rate stops in the reactor when left at these conditions. Due to no flow occurring the resulting cooling curves are due to conduction to the wall+insulation and convection to the ambient air alone.

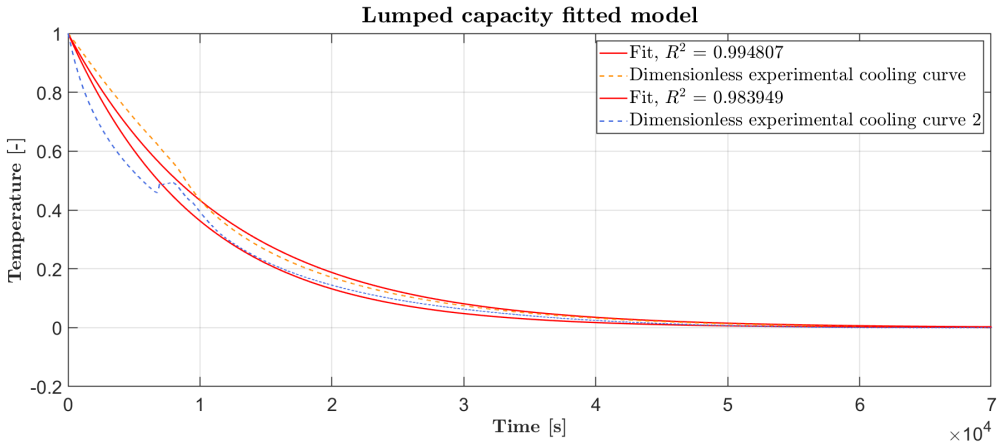

Figure 4.22: An example output for the cooling curves and the fitted lumped capacitance curves. Note that these are in a non-dimensionless form to allow for fitting and universal usage.

The resulting cooling curves as seen in figure 4.22 are fitted to the lumped thermal capacitance model. In this consideration the lumped material is assumed to be the steel of the reactor. The air and insulation heat transfer are assumed to be lumped in the value of the heat transfer coefficient h_c. This gives an effective heat transfer resistance for the casing independent of shape, and whether condensation is occurring in the reactor. The required information on surfaces of the reactor is taken from the CAD model, and the thermal responses of the thermowells averaged to increase the accuracy of the evaluation.

2. FLIR data During two of the experiments FLIR images were taken from the reactor. This is possible since the casing is painted in a matt honey yellow (RAL 1005) which has a non-reflective surface allowing FLIR imaging. These images serve two purposes:

1. Evaluation of local heat phenomena such as heat leakage at casing seams.
2. Using the measured surface temperature, casing area, and the known ambient heat transfer coefficient the heat loss can be calculated. This allows for direct comparison of the analytical methods for evaluation of the performance of both methods. Although the values are obtained for only two experiments it still gives a strong indicator on typical heat losses behaviour: due to the large insulating factor small perturbations in temperature between experiments are expected to have a minimal effect.

The taken FLIR images are evaluated assuming 5 sections of the casing in which the highest measured temperatures are used for evaluation of that specific section. This is a rather crude method, but is a good indicator for model validity and whether this method holds any merit. An example of such an image analysis is given in figure 4.23.

Figure 4.23: An example of the FLIR image evaluation. Note that the at places with a stronger temperature variation smaller surface are used to enhance accuracy. The surfaces in the left image corroborate with those in the right image. Note that due to using a slightly different angle in the photographs the surfaces are unequal, the surfaces for calculations are taken from the CAD model.

4.3.2. Evaluation - Thermal losses

Table 4.4: Comparison between FLIR, lumped experimental and modelled heat losses for two set points. The F indicates that during this experiment the condenser fan was active.

	FLIR [W]	**Lumped 215 [W]**	**Lumped 230F [W]**	**Model 215 [W]**	**Model 230F [W]**
Casing section 1	40.1	18.9	20.6	21.9	25.8
Casing section 2	54.7	25.9	27.6	34.3	39.2
Casing section 3	34.0	18.7	20.0	3.40	4.28
Casing section 4	18.1	8.80	8.36	5.46	6.27
Casing section 5	23.5	14.5	8.76	1.07	1.16
Total	170.4	86.8	84.92	66.13	76.71

It can be seen from the data presented that the main heat losses occur in the section 1-3. This is expected since these are also the sections where all of the heat is generated, and the highest temperature occur. This can also be seen in the qualitative sense in figure 4.23. Generally the FLIR, lumped evaluation and nodal model show the same trends for each casing section of heat loss, but the differences between methods can be significant. It can be discerned from the data that the lumped evaluation and modelling cases are in relative proximity of one another. The FLIR evaluation is roughly a factor 2 above the lumped and simulated heat losses. This can be attributed to multiple factors:

1. FLIR images are very sensitive to the correct settings for emisitivity and reflection of the surface photographed. Although the FLIR camera used was set to settings recommended for matt surfaces deviation is likely.

2. The surface evaluation is for the highest temperature seen at that specific section. As a consequence the image is a worst case image, and if for example image evaluation programs are used a significantly lower heat losses estimate is found.

3. A natural convective heat transfer coefficient of 15 $\mathrm{W/m^2K}$ was used, however, this value is an approximation. It is likely that not every section experiences the same heat transfer coefficient due to for example the air flow in the fume hood.

Combining these effects it can be seen why the FLIR imaging based heat losses can differ to such a significant degree. For future evaluations each of the earlier mentioned factors needs to be better controlled. For example the FLIR camera should be calibrated for a known heat flux of the surface evaluated, and also an imaging toolbox should be linked to this calibration.

The found values are checked against a simple heat balance of the experimental data to evaluate which method is most likely to find the overall losses. The heat balance used has been an adoption of Vroegindeweij's thermal losses method [1]:

$$\mathrm{Q_{losses-casing}} = \mathrm{Q_{heaters}} + \mathrm{Q_{exothermic}} - \mathrm{Q_{riser}} - \mathrm{Q_{cooler}} \tag{4.8}$$

It is important to note here that the heat losses defined for the riser and cooler are determined through the use of $\mathrm{C_p}$ values based on the CHERIC correlations shown in appendix A [1]. This means that additional heat losses in the condenser due to condensation are neglected. As a consequence the actual heat lost through the condenser is likely more than the correlations used for this balance indicate. This means that the casing looses less heat than indicated by this balance.
The additional losses through the condenser are estimated to be in the range of 20-50 W when assuming condensation occurs in the cooler which is a typical value for the previous design [1]. Nonetheless the values obtained from the balance can still indicate which losses model (FLIR or Lumped) is best able to estimate the heat losses of the casing.

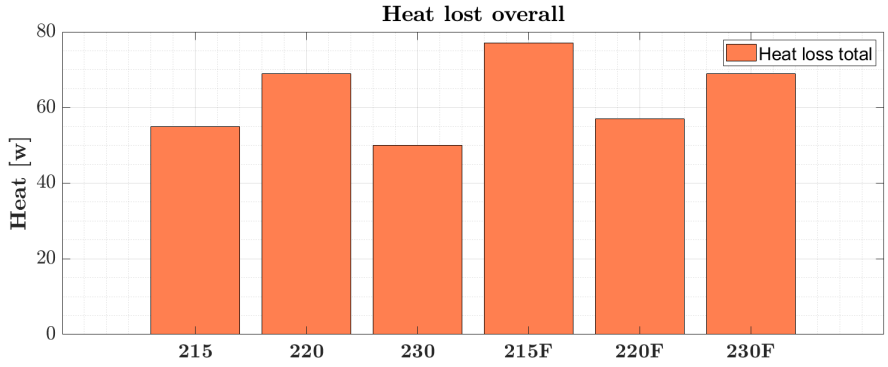

Figure 4.24: The summation of heat losses according to the thermal balance. The number indicates the set-point of the experiment, and the letter F indicates that the cooler was cooled by a fan. All experiments are from the full 6x5 catalyst bed set of experiments.

From the table and bar graph it can be seen that the losses of the thermal balance are generally within the values of the model. The lumped approach overestimates the losses with around 10-35 W, and the FLIR imaging method shows a deviation of around a factor 2 compared to experimental data. Combining these findings it is probable to state that the isolation casing performs within the prediction of the model. The casing looses on average 70 W according to the model, 85 W according to the lumped method, and 60 W according to the thermal balance method. For further evaluations in this work the Lumped method will be used since this indicates the worst case possible. The main reason for selection of this method is due to it being independent of released condensation heat/performance of the reactor bed. For future designs it is advised to start making use of heat flux sensors to negate the use of these worst-case estimation methods.

The results seem to proof the main aim of the usage of such a casing: the prevention of heat leaks due to cracks and seams in the isolation as experienced by Vroegindeweij [1]. Furthermore due to the heat balance overestimating the losses it is probable that the casing performs better than the model. The model assumes a pipe insulation structure which has more exchange area with the ambient area than the casing does. In order to evaluate whether this is the case a thermal analysis should be made using higher level methods such as a combined CAD - FEM/FVM approach.

Findings - Insulation casing:

1. **The insulation casing has a typical heat loss in the range of 50-85 W. In which the lower bound of the estimation is based on thermal balancing equations, while the higher bound is based on lumped capacitance evaluation of cooling curves.**
2. **FLIR imaging is seen as an outlier due to the significantly higher losses estimation compared to the other 2 methods employed. It is advised to calibrate the camera using a known heat flux and similar surface, and use imaging software to increase the accuracy of this method.**
3. **Heat-flux sensors are advised to be used in future designs to give a much clearer and likely more precise evaluation of heat losses of the reactor.**
4. **The insulation casing seems to meet the main developmental goals of significantly decreasing the amount of heat leaks due to crakcs/gaps. The model predicts the performance relatively well, but it is advised to do a more in depth study using the actual shape and more high levelling thermal modelling tools such as FEM/FVM.**

4.3.3. Evaluation - Heat Exchanger

The previous work of Vroegindeweij showed a highly efficient heat exchanger [1]. In order to evaluate the transferred heat of the condenser the same approach as used by Vroegindeweij is used [1]. In this approach it is assumed no condensabels are present in the tube side, and therefore the released heat can be calculated with relative ease. The released heat is assumed to all be transferred to the shell side without losses due to the tubes not being in contact with the walls. This gives the following set of formula, as appeared in the work of [1]:

$$\mathrm{LMTD} = \frac{(\mathrm{TAR} - \mathrm{TAH}) - (\mathrm{TAS} - \mathrm{TAC})}{\ln(\mathrm{TAR} - \mathrm{TAH}) - \ln(\mathrm{TAS} - \mathrm{TAC})} \tag{4.9}$$

$$\mathrm{U_{HEX}} = \frac{\dot{m}\mathrm{C_p}(\mathrm{T_{in}} - \mathrm{T_{out}})}{\mathrm{A_{TS}LMTD}} \tag{4.10}$$

Sensor suite Heat Exchanger

Figure 4.25: The wall sensors used on the heat exchanger.

The following set of sensors (identical type as the reactor bed) as shown in figure 4.26 are used to evaluate the behaviour of the heat exchanger:

1. **TAC** Temperater After Cooler is the thermowell placed within the catchtank and is seen as the **tube side inlet temperature**.
2. **TAH** Temperature After Heat Exchanger is placed at the **outlet** of **tube side** and gives its **temperature**.
3. **TAR** Temperature After Reactor is a thermowell placed at the reactor outlet and indicates indicates the **shell side inlet temperature**.
4. **TAS** Temperature After Shell is placed at the start of the condenser and gives the **shell side outlet temperature**.
5. **Wall 1-4** These NTC's are placed at the outside wall of the heat exchanger. This is at the left side of the heat exchanger, and the senors are placed between two baffles with an interval of 2 baffles (being 50 mm total distance between sensors).

Figure 4.26: The temperature probes used at the cold side of the reactor. Note the equal spacing of the wall mounted temperature sensors at the shell of the heat exchanger. The red blue arrow indicates flow direction with red a high and blue a low temperature.

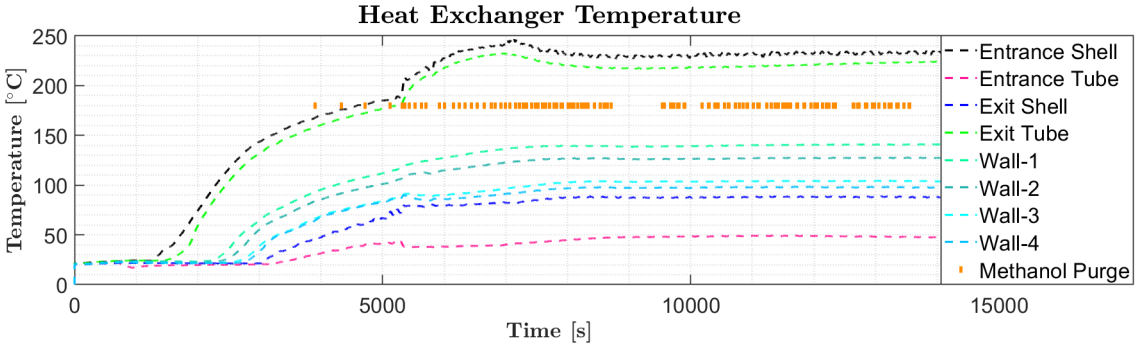

Figure 4.27: The typical temperatures (with the location of the sensors shown in figure 4.26) of the heat exchanger during an experiment. Especially the qualitative behaviour can be generalised for all experiments. Note the decrease in temperature slope between the wall sensors as also shown in figure 4.24. Furthermore the sudden increase in all temperatures at t=4000s is due to the onset of exothermic reaction. It clearly signifies the importance of the onset of exothermic behaviour on the overall start-up time. The methanol purge indicates when product was released from the catch tank due to the level sensor indicating 'wet'. The large interval at for example t=9000 s is when the level control is temporaroly off due to other measurements taking place.

Comparing between the experimental results it is evident that the heat exchanger exchanges a significant amount of heat. The typical increase in temperature of around 180-200 °C at the tube side clearly signifies this. It is interesting to note that typically the heat exchanger temperature data is relatively constant during an experiment. It is furthermore interesting to note that the transient behaviour of the heat exchanger is a good indicator of the importance of the onset of reaction. It can be seen in figure 3.17 that when the reactions start to occur (the reactor bed has a temperature above 180-190 °C there is a sharp rise in all temperatures. This is made further evident in figure 4.27 by the start of purging of condensate by the reactor. This operation is controlled by the level control system, and therefore the start of purging is due to the formation of condensate (onset of production).

Comparing the simulation and experimental results the large difference in total heat transferred is apparent as can be seen in figure 4.28. However this difference can be explained due to the discrepancy in methanol production between model and experiments. This has been thoroughly discussed in the section on the reactor bed, and the differences in heat flux are likely to be due to the higher production estimate of the model.

Table 4.5: The numerical and experimental results found for the heat exchanger. The values in parenthesis for TAC are the values for the lowest measured condenser temperature. These are likely more representative in comparison with the model. This is due to the condensate in the catch tank not having an influence on the temperature measurement as is likely the case with the TAC thermowell situated in the catch tank.

Setpoint pre-heater [°C]	**Fan** [-]	**Catalyst size** **[mm]**	**TAC** [°**C**]	**TAH** [°**C**]	**TAR** [°**C**]	**TAS** [°**C**]	**TC-internal** [°**C**]
			Experimental || Simulated				**Experimental**
215	No	6x5	45(35) || 33	222 || 248	229 || 273	96 || 88	259
220	No	6x5	46(41) || 30	230 || 229	233 || 251	93 || 82	270
230	No	6x5	47(38) || 33	224 || 249	227 || 273	99 || 89	264
215	Yes	6x5	40(29) || 33	216 || 220	236 || 239	85 || 89	253
220	Yes	6x5	42(31) || 31	224 || 230	243 || 252	89 || 82	264
230	Yes	6x5	39(31) || 33	228 || 251	238 || 265	91 || 88	267
215	No	6x2.5	47(27) || 37	201 || 221	212 || 240	73 || 83	240
220	No	6x2.5	49(28) || 46	208 || 244	231 || 265	78 || 97	249
230	No	6x2.5	48(27) || 45	222 || 249	267 || 272	71 || 95	267
215	Yes	6x2.5	38(24) || 37	208 || 221	222 || 259	65 || 83	239
220	Yes	6x2.5	37(24) || 41	217 || 236	228 || 258	70 || 91	254
230	Yes	6x2.5	40(24) || 44	226 || 249	259 || 268	72 || 94	268

The temperatures of the heat exchanger are predicted fairly well by the model. It should be noted that the experimental values of TAH are likely lower than the actual outlet temperature of the reactor bed. The probe TC-internal is generally place at the outlet point of the reactor bed and therefore signifies the outlet temperature. The underestimation of TAH is suspected to be due to a combination of:

- The heat exchanger is close to the sensor of TAH, and thus the outlet gasses might be cooled by this heat exchanger decreasing the temperature.
- It could be that local flow phenomena, such as mixing or plume forming, cause a decrease in the temperature measured. With plume forming it is meant that the hot gasses rise much like how smoke does from a fire: in a small hot column with cold ambient air around. If the TAH thermowell is not within this plume the temperature measured is of the colder gas surrounding this plume giving lower values.

A similar discussion can be held for the sensors TAC, where the values in table 4.5 between parentheses signifies the coldest measured temperature in the cooler. The sensor TAC itself is placed within the catch tank where also condensate is held. If for example the gas travels in a plume like shape above the TAC sensors to the entrance of the heat exchanger it is possible that the gas entering the heat exchanger is colder than the TAC indicates. Furthermore, this is also more in line with how the model describes the heat transfer since it assumes no liquid hold-up. The outlet temperature of the cooler is close to this value in the experimental sense and therefore added to the table 4.5.

Temperatures are seen as the best comparison between model and experiments since temperatures are the driving forces in both. Furthermore all constraints in the model are based on temperature: lowest achievable temperature the condenser can attain, dew temperatures, inlet temperature of the bed, and maximum outlet temperature of the bed due to chemical equilibrium. Consequently this means that if the model and experiment have the same temperature but a difference in heat transfer is found that this must be due to the discrepancies in the heat transfer coefficient, heat capacity, and mass flow

Figure 4.28: Heat transfer and total heat transferred comparison between experiments and models for a set of experiments. E stands for experiment and S for simulation. F indicates the condenser was cooled by a radial fan.

rate. Especially the effect of the heat capacity is interesting: in the condensing region a temperature drop signifies a significantly higher amount of heat release than in the case of pure gas.
Therefore a deviation of a few degrees between reality and model can signify a large heat flux difference. It is known that the model over predicts the mass flow (generally in the realm of 1.5-2 too high) and the heat transfer is also over predicted by the model as can be seen in figure 4.28. This signifies that the heat transfer correlations used by the model are likely too optimistic, and this is attributed to the higher predicted mass flow and the correlations being relatively simple: they do not take into account by-pass flow, leaks, and a non-ideal flow path which was also found by [1].

Findings - Heat Exchanger

- **The model and experiments agree relatively well in terms of temperature. Due to temperature being the driving force and constraint in the model it is assumed this signifies that the modelling is relatively successful.**
- **Significant deviation is seen in terms of total heat transferred between model and experiments. This is attributed to the lower flow rate and production of methanol in the experiments. This also causes a noticeable difference in heat transfer coefficient. It is encouraged to create a custom heat transfer correlation for the heat exchanger to evaluate whether the higher heat transfer can be fully attributed to production and mass flow rate effects.**

4.3.4. Condenser

The section where condensation is expected to occur is the condenser section. The following sensors were used to evaluate the condenser design shown in chapter 3:

1. **TAH** Temperature After Heat exchanger is a thermowell placed directly at the outlet of the heat exchanger.
2. **TTC** Temperature Top Cooler is the temperature at the end of the insulation of the condenser. It can be see as the **inlet temperature for the condenser section** itself.
3. **Cooler 1-4** A group of 4 NTC sensors are placed on the surface of the condenser to track the temperature behaviour at the condenser locally.
4. **TAC** Temperature After Cooler is the catch-tank (condensate hold tank) temperature.

During experiments it was found that the difference in temperature between TAH and TTC (right section) was of the same order as TTC and TAC (left section). This is an unexpected result since the riser section (between TAH and TTC) as can be seen in figure 3.19 is insulated and should have a significantly lower drop in temperature. It was checked by through temperature measurements at the surface of the insulation whether the insulation was under-performing and this was not the case.

H_2 is injected in the insulated section and might cause such a temperature drop, but evaluation of the data using temperature, correlations for mass flow rate and heat capacity, and valve duty also ruled this out. Eventually the sensor itself was checked and was found to have partially slipped out of the thermowell. In order to further vary this, two additional NTC's were placed at the location of TTC and TAH to measure the wall temperatures, which should be in relative proximity of the thermowells (within 5 °C. This was found to be the case, and therefore a malfunctioning thermowell is seen as the cause. The remaining data showed behaviour one would expect with the right section of the condenser insulated, and previous experimental data was corrected. This correction is seen as permissible since it only concerns the amount of heat loss through the isolated section of the condenser which is a very well understood phenomena and overall of a very low amount. Therefore the upper-bound heat loss estimation is used to calculate the actual TTC temperature for the experiment where TTC was malfunctioning.

Evaluation

Table 4.6: Numerical and experimental results obtained for the condenser section.

Setpoint pre-heater [°C]	**Fan** [-]	**Catalyst size** **[mm]**	**TAC** [°**C**]	**TAS** [°**C**]	**TTC** [°**C**]	**T-Fin high** [°**C**]	**T-Fin low** [°**C**]
			Experimental || Simulated				
215	No	6x5	45(35) || 33	96 || 82	83 || 88	51 || 73	35 ||37
220	No	6x5	46(41) || 30	93 || 82	78 || 81	83 || 72	41 || 30
230	No	6x5	47(38) || 33	99 || 89	90 || 87	54 || 76	38 || 33
215	Yes	6x5	40(29) || 33	85 || 89	73 || 74	48 || 76	29 || 33
220	Yes	6x5	42(31) || 31	89 || 82	80 || 81	51 || 70	31 || 31
230	Yes	6x5	39(31) || 33	91 || 88	73 || 90	52 || 76	31 || 34
215	No	6x2.5	47(27) || 37	82 || 83	73 || 81	51 || 73	27 || 38
220	No	6x2.5	49(28) || 46	84 || 97	78 || 95	55 || 87	28 || 46
230	No	6x2.5	48(27) || 45	89 || 95	81 || 94	54 || 85	27 || 45
215	Yes	6x2.5	38(24) || 37	76 || 87	65 || 81	44 || 73	24 || 37
220	Yes	6x2.5	37(24) || 41	78 || 91	70 || 90	46 || 81	24 || 42
230	Yes	6x2.5	40(24) || 44	82 || 94	72 || 93	48 || 85	24 || 45

Generally the riser insulation performs about a factor 2 worse than simulated. This was expected since the riser is isolated using commercially available pipe insulation. It is known that this generally performs worse than modelled due to the presence of cracks [1].

The cooler section of the condenser generally shows a temperature decrease to near ambient temperature. The model shows the same trend and the discrepancies between model and experiments is mainly evident between TTC and T-fin high as can be seen in table 3.15. On first glance it seems like the experiments loose more heat than the model indicates, with a significant amount of heat lost before the finned section. However, when also taking into account figure 4.29 and the earlier shown discrepancies between model and experiments a different pictures starts to emerge. The model significantly over-predicts the amount of methanol and water as shown in table 4.2. This means that there are less condensables present in the experimental case. As shown in the pseudo-C_p method the amount of heat released due to the presence of condensate is significant. Therefore if less condensables are present there is also significantly less heat available to be released. In the case of two identical condensers with identical heat transfer coefficients the one with less condensables will therefore have a lower outlet temperature.

Therefore it is assumed that due to less condensable being present in the experiments versus the model there is less heat available to be ejected. This in turn allows for a larger drop in temperature in the experimental case. Due to the condenser being designed on the model results it also explains why the lowest temperature T-Fin low is relatively constant for all experiments. Effectively the finned section can condense more than is present in the experimental section. This also explains why the mass flow rates are in relative proximity of one-another (even for Fan and no-Fan cases); one of the dominant determining factors (the cooler/sink temperature) is relatively constant.

Looking at the heat transfer coefficients the difference between the experiments and model is large at a factor of 1.1-2.6. This is attributed to the lower amount of condensates present in the experiments. During experiments the Fan and no-Fan experiments are in relative proximity of one-another. This either means that the fanned section is able to already condense all condensable in the no-Fan (natural convection) case or that the fin efficiency is very high. It is deemed likely that all condensable are condensed in all cases due to the low temperature of T-Fin low. The fin efficiency is likely high aswell since during forced convection experiments the fin temperature decrease to relatively low temperatures.

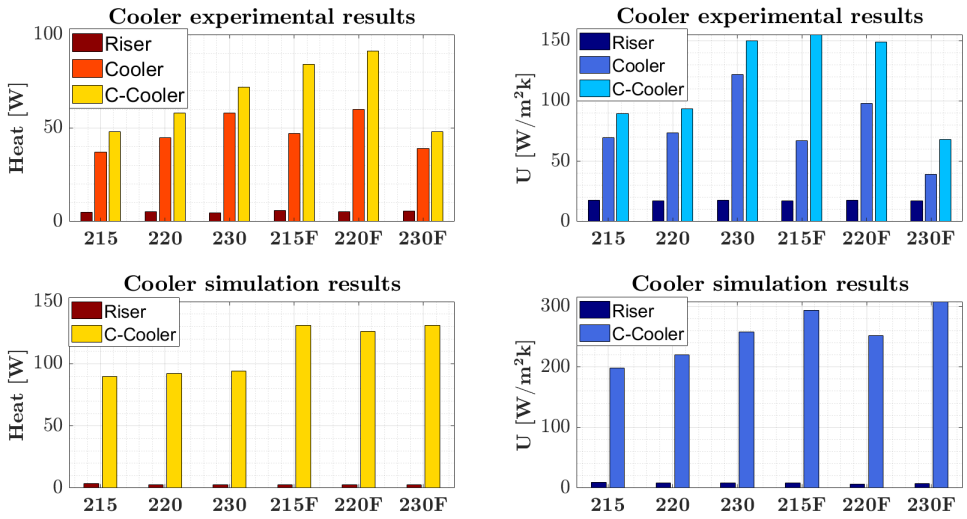

Figure 4.29: The values of E stand for experiments and S for simulated results for the indicated temperature set points. Note that the $\mathrm{E_c}$ values are calculated taking into account condensate being formed (this is denoted by the C- prefix).

The information of figure 4.29 and table 4.6 seems to suggest that the condenser in the experimental case is not thermally limited. This can be seen in the near constant temperature of the fins while the amount of heat transferred increases with the set-point. The model does not follow this trend since the heat transfer coefficient appears to be limiting. This has as a consequence that the condenser rises in temperature. This limiting effect of the heat transfer coefficient is due to the air side, since otherwise the heat transfer coefficient would be significantly higher (in the order of 1000 $\mathrm{W/m^2K}$). It is furthermore important to note that the decrease in heat transfer and coefficient for the experimental F set-point is likely due to analysis. This value is on average production values and sensitive to the mass flow rate measurements which are known to be decreasing during an experiment. It is therefore possible that the decrease seen is due partially due to these analysis methods. Since the temperatures reported in table 4.6 are also in relative proximity this decreasing trend is put to mass rate measurements.

The model is able to predict the temperatures in closer proximity than is the case with the previous version where latent heat was not accounted for. More in depth validation alike the methods proposed in the heat exchanger are called for, and should be performed. The experimental data indicates that NCG is not a limiting factor, which is in accordance with the modelling results. Future experiments could focus on causing this limitation to evaluate the NCG model. Regardless the model seems to indicate that even at a much higher heat release through the condenser no NCG condensation limitation is found (evident from the steady increase in heat release). It could therefore be likely that the NCG limitation will not affect fin design appropriate for ZEF. This also means that the NCG model can be taken out of the model which reduces complexity of the model and increases computational speed.

Findings - Condenser

- **The condenser section shows a significantly lower amount of heat release than predicted by the model. This is mainly attributed to the lower amount of condensables present than predicted by the model.**
- **The condenser has been designed to cool a significantly higher amount than experiments achieve, and data seems to suggest this is also the case. As a consequences the lowest temperature in the reactor is nearly constant across all experiments, and therefore condenser temperature seems to have little influence on the mass flow rate.**
- **NCG limiting effects could not be identified in the data. Significantly more efficient condenser designs (liquid cooled for example) could incur these limitations. This is beyond the use case for ZEF and therefore the NCG modelling can be taken out of the nodal model. This should aid in increasing computational time of the model.**

5

Conclusions & Recommendations

Using the modelling and experimental results of the previous chapter the research questions of chapter 1 can be answered or a strong indication can be given of the likely answer. Furthermore recommendations will be given for possible future research to further the understanding of the design and improve its performance. The conclusion will be discussed per research domain indicated in chapter 1. These conclusion are based on the model and experimental data. For the underlying reasoning why certain effects or results are accepted (or seen likely) the reader is referred to the previous chapter. Recommendations are also immediately given in order to keep an overview between the separate research domains.

5.1. Control

What feed design is able to not let flow stall occur in the reactor?

Through experiments it was found that an injection system where H_2 is injected close to the shell side exit does not promote flow stall (known as option III in figure 3.10). Large volume injections of H_2 do not incur flow tall indicating that this injection system shows great resilience. No data currently suggests that this injection site of CO_2 (at the tube side inlet of the heat exchanger) causes adverse effect and therefore should be kept as is.

What control method and/or design can prevent drift from occurring?

The usage of a cascaded PID coupled to composition was found to be appropriate. Generally the reactor can be kept in relative close proximity of the desired composition. Experimental data seem to suggest that reactor bed geometry has an influence on how well the reactor can be kept at a certain composition. This is probably due to certain bed designs having a non-steady consumption of reactants.

Which approach can be used to measure the mas flow rate in the reactor?

It was found that using a custom built differential pressure sensor allowed for relative accurate measurement of the mass flow rate, and is seen as the preffered method for mass flow rate measurements. A method based on the lumped thermal capacitance model being coupled to the pre-heater behaviour shows promise, but is very susceptible to changes in the underlying correlations used.

5.1.1. Recommendations

- The effects of reactor bed design on composition control should be better understood. If the reactor bed consumption of reactants can be modelled accurately the composition control will not require to increase its sampling rate.

- Further experiments should be performed to calibrate the lumped pre-heater mas flow rate measurement method. It might be the case that this method allows for a cost effective method to measure mass flow rate in the reactor. It is also imaginable that this could work for the autothermal mode of the reactor using a pulsing mode.

5.2. Condensation

What is the effect of condensation on the temperature profile and lowest obtainable temperature of a natural convection methanol synthesis reactor designed to operate autothermally within ZEF's KPI's?

Condensation causes a non-linear temperature profile in the condensing regions which is seen in experiments as well as in the model. The model is able to capture the qualitative behaviour but deviations are seen in the quantitative comparison of temperatures. These deviations are largely attributed to differences in mass flow rate and total methanol production between model and experiment.

The condenser is over designed and is able to fully condense all available remaining products exiting the heat exchanger. The model and experiments agree in qualitative behaviour but quantitatively differ up to a significant degree in temperature. This is mainly attributed to the differences in mass flow rate and production of methanol between model and experiment. NCG caused limitations are not observed in model and experiments, and it is seen as highly likely that these will not be incurred for any possible air cooled condenser design for this type of reactor.

5.2.1. Recommendations

- Calibration experiments with a known amount of condensate should be performed. By doing so the model can be evaluated without the ambiguity/influences of reactor bed performance.

- Experiments should be performed to measure the composition of the condensate present. By doing so it can be evaluated how well the reactor bed performs.

5.3. Reactor bed

What is the significance of the intra-particle diffusion limitations and how can these be mitigated?

Modelling results indicate that the intra-particle diffusion effects are present and are in the realm of 0.7-0.8 catalyst effectiveness on average. Due to other limitations being present in the experiments the intra-particle diffusion effects cannot be quantified. However decreasing catalyst pellet size increases overall STY which is linked to mitigation of diffusion limitations.

What packed bed reactor geometry/design is able to approach isothermal behaviour while maintaining a simple mass producible design?

Experimental and modelling results indicate that the design is not capable of approaching an isothermal design as of yet. This attributed to the lack of conductive structures and sub-optimal flow (in terms of mass flow rate and path) which can aid in attaining a higher degree of temperature homogenisation. A STY increase of a factor of 1.25 is experimentally found. An improved design is presented which should offer a significant increase in performance (STY) while retaining the mass manufacture characteristics. The model over-predicts the performance of the bed and a different modelling strategy is proposed.

5.3.1. Recommendations

- The testing of the presented new reactor bed design is highly encouraged. The new bed should increase the STY due to negating adverse flow effects.
- The decreasing of catalyst size should continue since currently mass flow rate was not affected by a significant amount by the decrease in catalytic pellet size.
- Experiments in which the catalyst is diluted with an inert material is advised. It will aid in identifying the size of mass transfer limitations at the outside of the catalytic material. Furthermore, it could aid in decreasing the potential of hot spot formation in the reactor bed which is detrimental to STY.
- A comparison with structured catalyst or 3-D printed catalyst is highly recommended. The potential STY increase and the predictability of degradation of the overall bed is of great advantage of this type of reactor.
- The reactor model requires significant overhaul due to how the length scales in the bed are much closer than in the case of the previous bed designs. A sub nodal-model (to allow for synergy modelling with condensation) is advised to be developed for the reactor bed which might emulate the heterogenous reactor bed modelling possible with FVM models.

5.4. Conclusions outside of scope

Model performance

The model is clearly overestimating production and mass flow rate. The first effect has been identified due to how the bed likely deviates from the assumptions of the model. Especially deviations in flow is suspected to be a significant reason as to why the model and experimental results differ so greatly. Furthermore, the deviations in mass flow rate between the real world and model likely have a significant impact. Therefore an increase in model fidelity is warranted and potential methods have been indicated. Heat transfer mechanisms of the bed are likely the case why the transient behaviour of the model differs significantly from the real world. The used correlation overestimates heat transfer, and a more conservative equation should be found. Direct contact between catalyst with the heaters is advised.

Insulation casing

The Insulation casing is found to offer better insulation than would be expected from using pre-fabricated pipe shell sections. Practical experience indicates that for quick prototyping the casing is not advised: it roughly takes 1 day to fully assemble the casing and therefore sensor or heater changes to the surfaces held within is practically never performed. Foams are advised for mass manufacturing.

A

Correlations used

All correlations and data re-used in the nodal model as presented by Vroegindeweij's work [1]. All presented here unless indicated otherwise is taken from Vroegindeweij [1].

Fluid correlations

Name equation	Application	Equation
Darcy-Weisbach	Pressure drop pipes	$\Delta P = f_D \frac{L}{D_h} \frac{\rho u^2}{2}$
Churchill	Friction factor Darcy-Weisbach	$\Theta_1 = \left[2.457 \cdot \log\left[(\frac{7}{Re})^{0.9} + 0.27\frac{\epsilon}{D_h}\right]\right]$ $\Theta_2 = (\frac{37530}{Re})^{16}$ $f_D = 8\left[(\frac{8}{Re})^{12} + \frac{1}{(\Theta_1+\Theta_2)^{1.5}}\right]^{\frac{1}{12}}$
Kern	Shell side pressure drop	$A_s = \frac{(p_t - d_o)D_s l_b}{p_t}$ $u_s = \frac{\dot{m}}{\rho A_s}$ $d_e = \frac{1.27}{d_o}(p_t^2 - 0.785 d_o^2)$ $Re = \frac{u_s d_e \rho}{\mu}$ $f = 25.66 Re^{-1.057} + 0.05034$ $\Delta P = 8f \frac{D_s(N_b+1)}{d_e}(\frac{\rho u_s}{2}(\frac{\mu}{\mu_w})^{-0.14})$
Ergun	Pressure drop packed bed	$\Delta P = 150 L_b \frac{(1-\epsilon)^2}{\epsilon^3}\frac{\mu u}{d_p^2} + 1.75 L_b \frac{(1-\epsilon)}{\epsilon^3}\frac{\rho_f u^2}{d_p}$ $d_p = \frac{\nu_p}{s_p}$
Pascal	Static pressure differential	$\Delta P = \rho g \Delta h$

Thermal correlations

Name equation	Application	Equation
Laminar Gnielinski	h_c HEX tubes local	$Nu_{x,lam,1} = 3.66$
		$Nu_{x,lam,2} = 1.077\sqrt[3]{RePrD_i/x}$
		$Nu_{x,lam,3} = \frac{1}{2}(\frac{2}{1+22Pr})^{1/6}(RePrd_i/x)^{1/2}$
		$Nu_{x,lam} = (Nu_{x,lam,1}^3 + 0.7^3 + [Nu_{x,lam,2} - 0.7]^3 + Nu_{x,lam,3}^3)^{1/3}$
Laminar Gnielinski	h_c Hex tubes mean	$Nu_{x,lam,1} = 3.66$
		$Nu_{m,lam,2} = 1.615\sqrt[3]{RePrD_i/l}$
		$Nu_{m,lam,3} = (\frac{2}{1+22Pr})^{1/6}(RePrd_i/l)^{1/2}$
		$Nu_{m,lam} = (Nu_{x,lam,1}^3 + 0.7^3 + [Nu_{x,lam,2} - 0.7]^3 + Nu_{x,lam,3}^3)^{1/3}$
Turbulent Gnielinski	h_c HEX tubes local	$Nu_{x,turb} = \frac{(f_D/8)RePr}{1+12.7\sqrt{f_D/8}(Pr^{2/3}-1)}\left[1 + \frac{1}{3}(d_i/x)^{2/3}\right]$
Turbulent Gnielinski	h_c HEX tubes mean	$Nm_{x,turb} = \frac{(f_D/8)RePr}{1+12.7\sqrt{f_D/8}(Pr^{2/3}-1)}\left[1 + (d_i/l)^{2/3}\right]$
Gnielinski	Transitional regime	$Nu = (1-\gamma)Nu_{lam,2300} + \gamma Nu_{turb,10^4}$
		$\gamma \frac{Re-2300}{10^4-2300}$
Laminar Gnielinski	h_c other tubes mean	$Nu_{lam,1} = 3.66$
Turbulent Gnielinski	h_c other tubes mean	$Nm_{turb} = \frac{(f_D/8)RePr}{1+12.7\sqrt{f_D/8}(Pr^{2/3}-1)}$
Kern	h_c shell side	$f_h = 0.49Re^{-0.48}$
		$Nu = f_{hRePr^{0.33}}(\frac{\mu}{\mu_w})^{0.14}$
Mill	h_c packed bed	$Nu = (0.5Re^{1/2} + 0.2Re^{2/3})Pr^{1/3}$
		$\nu = \frac{\dot{m}}{\rho\epsilon A_c}$
		$a = \frac{s_p}{\nu_p}(1-\epsilon)$

CHERIC correlations

$$\mu = A_\mu + B_\mu T + C_\mu T^2$$
$$k = A_k + B_k T + C_k T^2 + D_\mu T^3$$
$$C_p = A_{C_p} + B_{C_p} T + C_{C_p} T^2 + D_{C_p} T^3 + E_{C_p} T^4$$

	H_2	CO_2	CH_3OH	H_2O	CO	N_2
A_μ	0.002187	0.002545	$-5.636 \cdot 10^{-4}$	-0.003189	0.003288	0.003043
B_μ	$2.220 \cdot 10^{-5}$	$4.549 \cdot 10^{-5}$	$3.445 \cdot 10^{-5}$	$4.145 \cdot 10^{-5}$	$4.747 \cdot 10^{-5}$	$4.989 \cdot 10^{-5}$
C_μ	$-3.751 \cdot 10^{-9}$	$-8.649 \cdot 10^{-9}$	$-3.340 \cdot 10^{-10}$	$-8.272 \cdot 10^{-10}$	$-9.648 \cdot 10^{-9}$	$-1.093 \cdot 10^{-8}$
A_k	0.008099	-0.007215	-0.007797	0.007341	$5.067 \cdot 10^{-4}$	$3.919 \cdot 10^{-4}$
B_k	$6.689 \cdot 10^{-4}$	$8.015 \cdot 10^{-5}$	$4.167 \cdot 10^{-5}$	$-1.013 \cdot 10^{-5}$	$9.125 \cdot 10^{-5}$	$9.816 \cdot 10^{-5}$
C_k	$-4.158 \cdot 10^{-7}$	$5.477 \cdot 10^{-9}$	$1.214 \cdot 10^{-7}$	$1.801 \cdot 10^{-7}$	$-3.524 \cdot 10^{-8}$	$-5.067 \cdot 10^{-8}$
D_k	$1.562 \cdot 10^{-10}$	$-1.053 \cdot 10^{-11}$	$-5.184 \cdot 10^{-11}$	$-9.100 \cdot 10^{-11}$	$8.199 \cdot 10^{-12}$	$1.504 \cdot 10^{-11}$
A_{C_p}	27.00	29.27	34.37	33.77	29.65	29.80
B_{C_p}	0.01193	-0.02236	-0.01340	-0.005946	-0.006502	-0.007019
C_{C_p}	$-2.407 \cdot 10^{-5}$	$52.653 \cdot 10^{-4}$	$2.236 \cdot 10^{-4}$	$2.236 \cdot 10^{-5}$	$1.833 \cdot 10^{-5}$	$1.744 \cdot 10^{-5}$
D_{C_p}	$2.146 \cdot 10^{-8}$	$-4.153 \cdot 10^{-7}$	$-2.0904 \cdot 10^{-7}$	$-9.962 \cdot 10^{-9}$	$-9.395 \cdot 10^{-9}$	$-8.480 \cdot 10^{-9}$
E_{C_p}	$-6.148 \cdot 10^{-12}$	$2.006 \cdot 10^{-10}$	$6.212 \cdot 10^{-11}$	$1.097 \cdot 10^{-12}$	$1.082 \cdot 10^{-12}$	$9.337 \cdot 10^{-13}$

Table A.1: Coefficients for CHERIC correlation per species

Fluid specific parameters

	H_2	CO_2	CH_3OH	H_2O	CO	N_2
ω	-0.216	0.239	0.556	0.344	0.066	0.039
T_c[K]	32.97	304.14	512.5	647.14	132.91	126.21
P_c[Bar]	12.93	73.75	80.84	220.60	34.99	33.90

Interaction coefficients used in the Peng-Robinson EOS

	H_2	CO_2	CH_3OH	H_2O	CO	N_2
H_2	-	-0.1622	0	0	0.0919	0.0711
CO_2	-0.1622	-	0.022	0.0063	0	-0.0222
CH_3OH	0	0.022	-	-0.0778	0	-0.2141
H_2O	0	0.0063	-0.0778	-	0	0
CO	0.0919	0	0	0	-	0.033
N_2	0.0711	-0.0222	-0.2141	0	0.033	-

B

Thermal insulation analysis miscellaneous

Cooling curves insulation estimation

Based on the cooling curves of the reactor while ensuring no flow occurs a lumped convective heat transfer coefficient is found. It assumes the standard thermal lumped capacitance approach:

$$\frac{T - T_e}{T_0 - T_e} = e^{-\frac{h_c A}{mC_{steel}}t} = e^{-t/t_c} \tag{B.1}$$

In this approach the steel is assumed as the thermal mass while the insulation and ambient air are seen as the 'fluid' surrounding the mass. By assuming an equivalent resistance the insulation and ambient air are lumped, since these dominate the time transient:

$$\dot{Q}UA(T - T_e) = \frac{T - T_e}{R} \tag{B.2}$$

$$\frac{1}{U} = \sum \frac{1}{R_{resistance}} \tag{B.3}$$

$$\dot{Q} = mc_p \frac{dT}{dt} \tag{B.4}$$

(B.5)

The cooling curves have been shown in chapter 4. These cooling curves are fitted to the model based above in which the to be fitted parameter is h_c. All temperatures are fitted for the overall mass of the reactor due to the temperature being non-dimensional therefore making only use of relative changes which are assumed equal for all. Below follows the list of values used for thermal evaluations, and can be seen as equivalent resistances of the shell.

Table B.1: Heat transfer analysis data lumped approach.

UA_1	0.1283 W/k
UA_2	0.0947 W/k
UA_3	0.0958 W/k
UA_4	0.1053 W/k
UA_5	0.1863 W/k
A_{steel}	0.3464^2
m_{steel}	7.88 kg
$C_{p,steel}$	502 j/kgK

Thermal analysis FLIR data

THe thermal analysis of the FLIR data is based around a measured external area, measured temperature, and assumed external heat transfer coefficient of 15 $\mathrm{W/m^2K}$ for natural convective heat transfer.

$$\dot{Q} = Ah_c(T_{surface} - T_e) \tag{B.6}$$

The following data was used for evaluation, and is based on CAD data for the CNC-mould of which the casing is made:

Table B.2: Heat transfer analysis data FLIR approach.

A_1	0.19497 m^2
A_2	0.162842 m^2
A_3	0.098936 m^2
A_4	0.096698 m^2
A_5	0.14644 m^2
FLIR setting	Mate
Emittance	0.8

The following images were used to check for the presence of thermal leaks, and images seem to indicate these are relatively small.

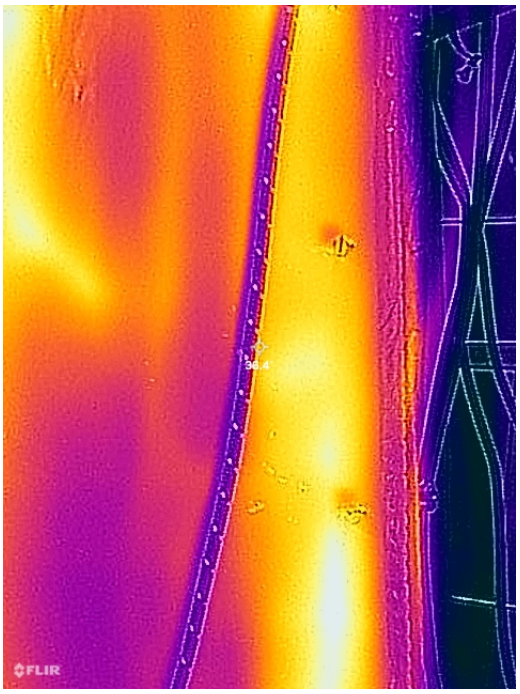

Figure B.1: Seem of section I, the whiter the colour the higher the temperature observed.

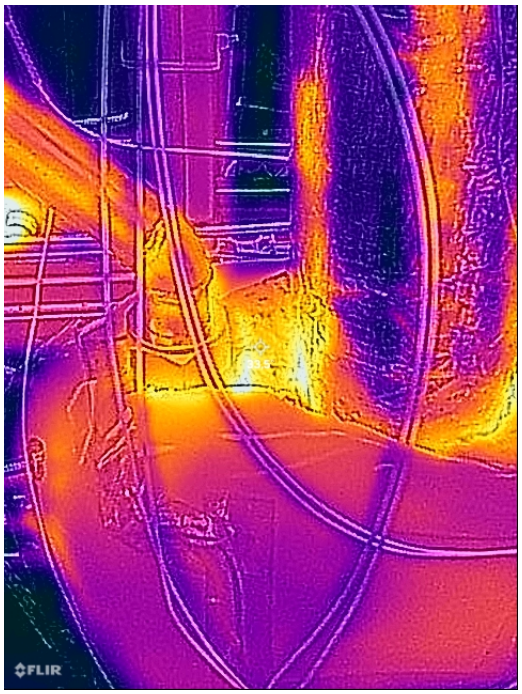

Figure B.2: Open section at the condenser. Some heat leakage can be seen, however the temperature observed here are relatively low (sub 40 °C).

Figure B.3: Seem of section II, there seems to be a minimal amount of heat leakage. The lower end is where the closure system is situated, and contains reflective material. The reading at that section should therefore not be taking into account.

C

Thermodynamic model decision tree

The thermodynamic model decision tree as appeared in [70]. All images and information in this section is taken from [70] unless stated otherwise.

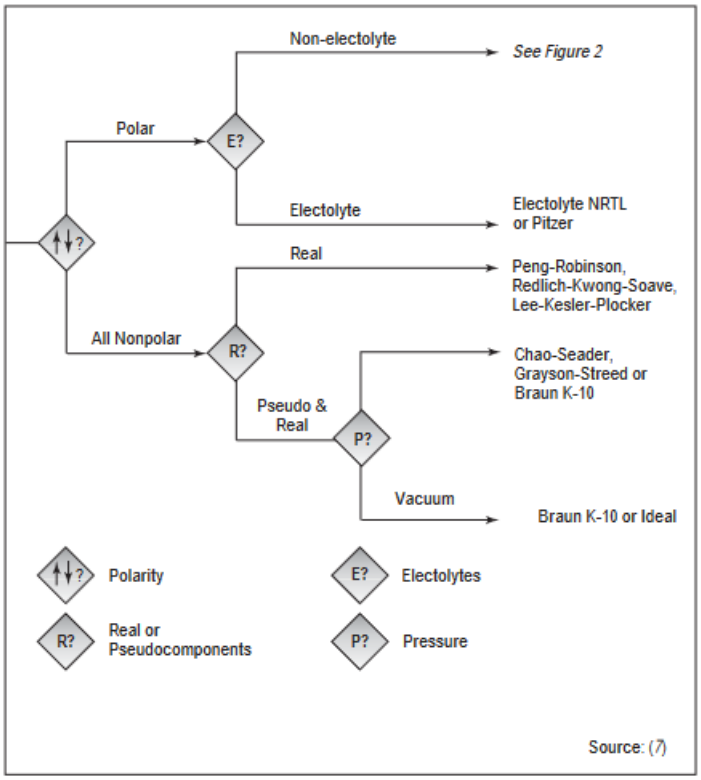

Figure C.1: Section 1 of model selection tree. Image adapted from [70].

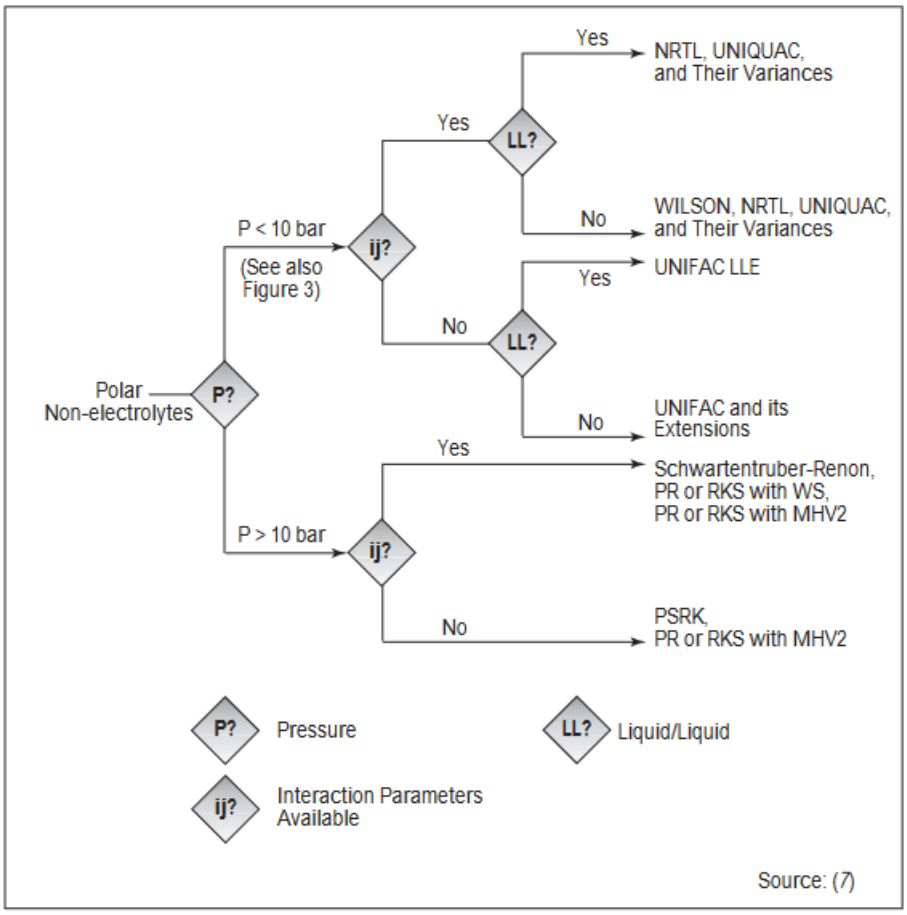

Figure C.2: Section 2 of model selection tree. Image adapted from [70].

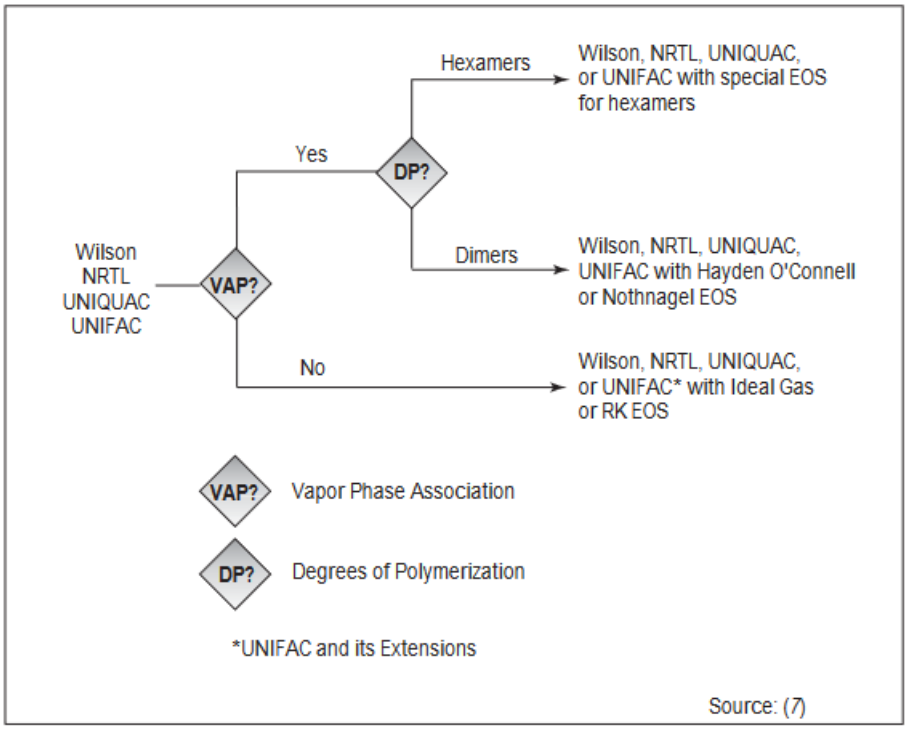

Figure C.3: Activity coefficient selection. Image adapted from [70].

D

Bibliography

[1] P. S. M. Vroegindeweij, “Modelling, Experimental Validation and Characterization of a novel small scale Methanol Synthesis Reactor,” Delft University of Technology, 2021. [Online]. Available: http://resolver.tudelft.nl/uuid:9dde9763-f83b-45ea-b393-f2c3f119d5fa.

[2] IPCC, “Climate change 2014: Synthesis report. contribution of working groups i, ii and iii to the fifth assessment report of the intergovernmental panel on climate change [core writing team, r.k. pachauri and l.a. meyer (eds.)],” IPCC, Geneva, Switzerland, 2014, 151 pp. [Online]. Available: https://www.ipcc.ch/report/ar5/syr/ (visited on 01/24/2022).

[3] E. A. Wrigley, *Energy and the English Industrial Revolution*. Cambridge University Press, 2010. DOI: 10.1017/CBO9780511779619.

[4] H. Lightfoot and O. Mamer, “Calculation of atmospheric radiative forcing (warming effect) of carbon dioxide at any concentration,” *Energy Environment*, vol. 25, pp. 1439–1454, Dec. 2014. DOI: 10.1260/0958-305X.25.8.1439.

[5] D. L. Chandler. “Explained: Radiative forcing.” (2010), [Online]. Available: https://news.mit.edu/2010/explained-radforce-0309 (visited on 02/15/2022).

[6] H. D. Lightfoot and O. A. Mamer, “Calculation of atmospheric radiative forcing (warming effect) of carbon dioxide at any concentration,” *Energy and Environment*, vol. 25, no. 8, pp. 1439–1454, Dec. 2014, ISSN: 20484070. DOI: 10.1260/0958-305X.25.8.1439.

[7] EPA. “Impacts of climate change.” (2021), [Online]. Available: https://www.epa.gov/climatechange-science/impacts-climate-change (visited on 02/07/2022).

[8] UNFCCC. “The paris agreement.” (2015), [Online]. Available: https://unfccc.int/process-and-meetings/the-paris-agreement/the-paris-agreement (visited on 02/07/2022).

[9] H. Ritchie and M. Roser, “Co□ and greenhouse gas emissions,” *Our World in Data*, 2020. [Online]. Available: https://ourworldindata.org/co2-and-other-greenhouse-gas-emissions (visited on 02/07/2022).

[10] NASA. “Drought shrinks california’s shasta lake.” (2021), [Online]. Available: https://climate.nasa.gov/images-of-change/?id=771#771-drought-shrinks-californias-shasta-lake (visited on 02/06/2022).

[11] M. R. Hannah Ritchie, “Energy mix,” *Our World In Data*, 2020. [Online]. Available: https://ourworldindata.org/energy-mix (visited on 02/06/2022).

[12] EIA. “Few transportation fuels surpass the energy densities of gasoline and diesel.” (2013), [Online]. Available: https://www.eia.gov/todayinenergy/detail.php?id=9991 (visited on 02/07/2022).

[13] P. Levi and J. Cullen, “Mapping global flows of chemicals: From fossil fuel feedstocks to chemical products,” *Environmental Science Technology*, vol. 52, Jan. 2018. DOI: 10.1021/acs.est.7b04573.

[14] M. J. Bos and D. W. Brilman, “A novel condensation reactor for efficient CO2 to methanol conversion for storage of renewable electric energy,” *Chemical Engineering Journal*, vol. 278, pp. 527–532, Oct. 2015, ISSN: 13858947. DOI: 10.1016/j.cej.2014.10.059. [Online]. Available: https://linkinghub.elsevier.com/retrieve/pii/S1385894714013916.

[15] G. Hodson, E. Wilkes, S. Azevedo, and T. Battaglene, “Methanol in wine,” *BIO Web of Conferences*, vol. 9, p. 02 028, 2017, ISSN: 2117-4458. DOI: 10.1051/BIOCONF/20170902028. [Online]. Available: https://www.bio-conferences.org/articles/bioconf/full_html/2017/02/bioconf-oiv2017_02028/bioconf-oiv2017_02028.html%20https://www.bio-conferences.org/articles/bioconf/abs/2017/02/bioconf-oiv2017_02028/bioconf-oiv2017_02028.html.

[16] S. Simon Araya, V. Liso, X. Cui, *et al.*, "A review of the methanol economy: The fuel cell route," *Energies*, vol. 13, no. 3, 2020, ISSN: 1996-1073. DOI: 10.3390/en13030596. [Online]. Available: https://www.mdpi.com/1996-1073/13/3/596.

[17] M. Bertau, H. Offermanns, L. Plass, F. Schmidt, and H. J. Wernicke, *Methanol: The basic chemical and energy feedstock of the future: Asinger's vision today*. Springer Berlin Heidelberg, Jan. 2014, ISBN: 9783642397097. DOI: 10.1007/978-3-642-39709-7.

[18] F. Dalena, A. Senatore, A. Marino, A. Gordano, M. Basile, and A. Basile, *Methanol Production and Applications: An Overview*. Elsevier B.V., 2018, pp. 3–28, ISBN: 9780444640109. DOI: 10.1016/B978-0-444-63903-5.00001-7. [Online]. Available: http://dx.doi.org/10.1016/B978-0-444-63903-5.00001-7.

[19] M. Bertau, H. Offermanns, L. Plass, F. Schmidt, and H. J. Wernicke, *Methanol: The basic chemical and energy feedstock of the future: Asinger's vision today*. Springer Berlin Heidelberg, Jan. 2014, ISBN: 9783642397097. DOI: 10.1007/978-3-642-39709-7.

[20] A. González-Garay, M. S. Frei, A. Al-Qahtani, C. Mondelli, G. Guillén-Gosálbez, and J. Pérez-Ramírez, "Plant-to-planet analysis of CO 2 -based methanol processes," *Energy & Environmental Science*, vol. 12, no. 12, pp. 3425–3436, Dec. 2019, ISSN: 17545706. DOI: 10.1039/C9EE01673B. [Online]. Available: https://pubs.rsc.org/en/content/articlehtml/2019/ee/c9ee01673b%20https://pubs.rsc.org/en/content/articlelanding/2019/ee/c9ee01673b.

[21] V. Dieterich, A. Buttler, A. Hanel, H. Spliethoff, and S. Fendt, "Power-to-liquid via synthesis of methanol, DME or Fischer–Tropsch-fuels: a review," vol. 13, no. 10, 2020, ISSN: 17545706. DOI: 10.1039/d0ee01187h.

[22] Zero Emission Fuels B.V. "Zero emission fuels webpage." (), [Online]. Available: http://zeroemissionfuels.com. (visited on 03/23/2022).

[23] A. Stankiewicz, T. Van Gerven, and G. Stefanidis, *The Fundamentals of Process Intensification.* Newark : John Wiley & Sons, Incorporated, 2019, p. 362, ISBN: 9783527680139.

[24] P. Basarkar, "Experimental Characterization of a Novel Small Scale Natural Circulation Loop Methanol Synthesis Reactor," Delft University of Technology, 2018. [Online]. Available: http://resolver.tudelft.nl/uuid:3f5c1c51-d04f-4026-88a5-0bb4c800cf2b.

[25] Y. Slotboom, M. J. Bos, J. Pieper, *et al.*, "Critical assessment of steady-state kinetic models for the synthesis of methanol over an industrial Cu/ZnO/Al2O3 catalyst," *Chemical Engineering Journal*, vol. 389, no. December 2019, p. 124 181, 2020, ISSN: 13858947. DOI: 10.1016/j.cej.2020.124181. [Online]. Available: https://doi.org/10.1016/j.cej.2020.124181.

[26] "Le Chatelier's Principle Fundamentals - Chemistry LibreTexts." (), [Online]. Available: https://chem.libretexts.org/Bookshelves/Physical_and_Theoretical_Chemistry_Textbook_Maps/Supplemental_Modules_(Physical_and_Theoretical_Chemistry)/Equilibria/Le_Chateliers_Principle/Le_Chatelier's_Principle_Fundamentals (visited on 03/01/2022).

[27] D. Sheldon, "Methanol Production □ A Technical History," *Johnson Matthey Technology Review*, vol. 61, no. 3, pp. 172–182, Jul. 2017, ISSN: 2056-5135. DOI: 10.1595/205651317X695622. [Online]. Available: http://www.ingentaconnect.com/content/10.1595/205651317X695622.

[28] BASF, *BASF-Geschichte chemie, die verbindet 1865-2015*. Unternehmenskommunikation & Regierungsbeziehungen BASF-gruppe, 2015. [Online]. Available: https://www.google.com/url?sa=t&rct=j&q=&esrc=s&source=web&cd=&cad=rja&uact=8&ved=2ahUKEwjW75fshKX2AhUNSfEDHbqhttps%5C%3A%5C%2F%5C%2Fwww.basf.com%5C%2Fglobal%5C%2Fimages%5C%2Fabout-us%5C%2Fhistory%5C%2FBASF-Geschichte_Chemie-die-verbindet-1865-2015.pdf&usg=AOvVaw2LacmhWZskYO0ZdAnssJ9T.

[29] V. Palma, E. Meloni, C. Ruocco, M. Martino, and A. Ricca, *State of the Art of Conventional Reactors for Methanol Production*. Elsevier B.V., 2018, pp. 29–51, ISBN: 9780444640109. DOI: 10.1016/B978-0-444-63903-5.00002-9. [Online]. Available: http://dx.doi.org/10.1016/B978-0-444-63903-5.00002-9.

[30] G. H. Graaf and J. G. Winkelman, “Chemical Equilibria in Methanol Synthesis Including the Water-Gas Shift Reaction: A Critical Reassessment,” *Industrial and Engineering Chemistry Research*, vol. 55, no. 20, pp. 5854–5864, 2016, ISSN: 15205045. DOI: 10.1021/acs.iecr.6b00815.

[31] M. J. Bos, Y. Slotboom, S. R. Kersten, and D. W. Brilman, “110th Anniversary: Characterization of a Condensing CO2 to Methanol Reactor,” *Industrial and Engineering Chemistry Research*, vol. 58, no. 31, pp. 13 987–13 999, Aug. 2019, ISSN: 15205045. DOI: 10.1021/acs.iecr.9b02576. [Online]. Available: https://doi.org/10.1021/acs.iecr.9b02576.

[32] D. Van Laake, “Development And Characterization Of A Small Scale Methanol Synthesis Reactor Based On Natural Convection,” Delft University of Technology, 2019. [Online]. Available: http://resolver.tudelft.nl/uuid:4d6d1637-9c56-4069-9d7b-323eeeea84b9.

[33] S. Mishra, “Characterization of Transient behaviors and Operability study of a novel small scale Methanol Synthesis Reactor,” Delft University of Technology, 2020. [Online]. Available: http://resolver.tudelft.nl/uuid:6fc5d6c4-825c-406a-8cc9-02c460f0ff56.

[34] M. J. Bos, Y. Slotboom, S. R. A. Kersten, and D. W. F. Brilman, “Supporting Information: 110th Anniversary: Characterization of a condensing CO 2 to methanol reactor,” 2019. DOI: 10.1021/acs.iecr.9b02576.

[35] S. F. Deli, “Optimization and characterization of a novel methanol synthesis reactor,” InHolland university of applied sciences, 2022.

[36] J. Hagen, “Industrial catalysis: A practical approach,” *Industrial Catalysis: A Practical Approach*, pp. 1–522, Sep. 2015. DOI: 10.1002/9783527684625.

[37] S. K. Wilkinson, L. G. Van De Water, B. Miller, M. J. Simmons, E. H. Stitt, and M. J. Watson, “Understanding the generation of methanol synthesis and water gas shift activity over copper-based catalysts-A spatially resolved experimental kinetic study using steady and non-steady state operation under CO/CO2/H2 feeds,” *Journal of Catalysis*, vol. 337, pp. 208–220, 2016, ISSN: 10902694. DOI: 10.1016/j.jcat.2016.01.025. [Online]. Available: http://dx.doi.org/10.1016/j.jcat.2016.01.025.

[38] G. Bozzano and F. Manenti, “Efficient methanol synthesis: Perspectives, technologies and optimization strategies,” *Progress in Energy and Combustion Science*, vol. 56, pp. 71–105, 2016, ISSN: 03601285. DOI: 10.1016/j.pecs.2016.06.001.

[39] R. Van Den Berg, G. Prieto, G. Korpershoek, *et al.*, “Structure sensitivity of Cu and CuZn catalysts relevant to industrial methanol synthesis,” *Nature Communications 2016 7:1*, vol. 7, no. 1, pp. 1–7, Oct. 2016, ISSN: 2041-1723. DOI: 10.1038/ncomms13057. [Online]. Available: https://www.nature.com/articles/ncomms13057.

[40] G. H. Graaf, E. J. Stamhuis, and A. A. Beenackers, “Kinetics of low-pressure methanol synthesis,” *Chemical Engineering Science*, vol. 43, no. 12, pp. 3185–3195, 1988, ISSN: 00092509. DOI: 10.1016/0009-2509(88)85127-3. [Online]. Available: https://linkinghub.elsevier.com/retrieve/pii/0009250988851273.

[41] K. M. Vanden Bussche and G. F. Froment, “A steady-state kinetic model for methanol synthesis and the water gas shift reaction on a commercial Cu/ZnO/Al2O3 catalyst,” *Journal of Catalysis*, vol. 161, no. 1, pp. 1–10, 1996, ISSN: 00219517. DOI: https://doi.org/10.1006/jcat.1996.0156. [Online]. Available: http://www.sciencedirect.com/science/article/pii/S0021951796901566.

[42] A. Jess and P. Wasserscheid, *Chemical technology : an integral textbook*. Weinheim, Germany : Wiley-VCH, 2013, 1 online resource (xxxvii, 850 pages) : ISBN: 3527670629.

[43] K. Ushikoshi, K. Mori, T. Kubota, T. Watanabe, and M. Saito, “Methanol synthesis from CO2 and H2 in a bench-scale test plant,” *Applied Organometallic Chemistry*, vol. 14, no. 12, pp. 819–825, Dec. 2000, ISSN: 0268-2605. DOI: 10.1002/1099-0739(200012)14:12<819::AID-AOC90>3.0.CO;2-{\#}. [Online]. Available: https://onlinelibrary.wiley.com/doi/abs/10.1002/1099-0739(200012)14:12%5C%3C819::AID-AOC90%5C%3E3.0.CO;2-%5C%23.

[44] M. Tatsumi, H. Tsukasa, and F. Daisuke, *US20130237618A1*. United States Patent Application Publication, Sep. 2013.

[45] R. Tesser and E. Santacesaria, “Revisiting the Role of Mass and Heat Transfer in Gas–Solid Catalytic Reactions,” *Processes 2020, Vol. 8, Page 1599*, vol. 8, no. 12, p. 1599, Dec. 2020, ISSN: 2227-9717. DOI: 10.3390/PR8121599. [Online]. Available: https://www.mdpi.com/2227-9717/8/12/1599/htm%20https://www.mdpi.com/2227-9717/8/12/1599.

[46] B. J. Lommerts, G. H. Graaf, and A. A. Beenackers, “Mathematical modeling of internal mass transport limitations in methanol synthesis,” *Chemical Engineering Science*, vol. 55, no. 23, pp. 5589–5598, Dec. 2000, ISSN: 0009-2509. DOI: 10.1016/S0009-2509(00)00194-9.

[47] G. H. Graaf, P. J. Sijtsema, E. J. Stamhuis, and G. E. Joosten, “Chemical equilibria in methanol synthesis,” *Chemical Engineering Science*, vol. 41, no. 11, pp. 2883–2890, 1986, ISSN: 00092509. DOI: 10.1016/0009-2509(86)80019-7. [Online]. Available: https://linkinghub.elsevier.com/retrieve/pii/0009250986800197.

[48] B. Lacerda De Oliveira Campos, K. Herrera Delgado, S. Pitter, and J. Sauer, “Development of Consistent Kinetic Models Derived from a Microkinetic Model of the Methanol Synthesis,” *Industrial and Engineering Chemistry Research*, vol. 60, no. 42, pp. 15 074–15 086, Oct. 2021, ISSN: 15205045. DOI: 10.1021/ACS.IECR.1C02952/SUPPL{_}FILE/IE1C02952{_}SI{_}001.PDF. [Online]. Available: https://pubs-acs-org.tudelft.idm.oclc.org/doi/full/10.1021/acs.iecr.1c02952.

[49] H. D. Baehr and K. Stephan, “Convective heat and mass transfer. Flows with phase change,” *Heat and Mass Transfer*, pp. 443–543, 2011. DOI: 10.1007/978-3-642-20021-2{_}4. [Online]. Available: https://link.springer.com/chapter/10.1007/978-3-642-20021-2_4.

[50] G. Towler and R. Sinnott, “Chapter 19 - Heat-Transfer Equipment,” in *Chemical Engineering Design*, G. Towler and R. B. T. .-. C. E. D. (E. Sinnott, Eds., Boston: Butterworth-Heinemann, 2013, pp. 1047–1205, ISBN: 978-0-08-096659-5. DOI: https://doi.org/10.1016/B978-0-08-096659-5.00019-5. [Online]. Available: http://www.sciencedirect.com/science/article/pii/B9780080966595000195.

[51] J. Huang, J. Zhang, and L. Wang, “Review of vapor condensation heat and mass transfer in the presence of non-condensable gas,” *Applied Thermal Engineering*, vol. 89, pp. 469–484, Oct. 2015, ISSN: 1359-4311. DOI: 10.1016/J.APPLTHERMALENG.2015.06.040.

[52] S. P. Venkateshan, “Special Topics in Heat Transfer,” *Heat Transfer*, pp. 815–913, 2021. DOI: 10.1007/978-3-030-58338-5{_}17.

[53] J. W. Rose, “CONDENSATION, OVERVIEW,” *A-to-Z Guide to Thermodynamics, Heat and Mass Transfer, and Fluids Engineering*, Aug. 2011. DOI: 10.1615/ATOZ.C.CONDENSATION{_}OVERVIEW. [Online]. Available: https://thermopedia.com/content/653/.

[54] X. Ma, J. Ma, H. Tong, and H. Jia, “The Investigation on Heat Transfer Characteristics of Steam Condensation in Presence of Noncondensable Gas under Natural Convection,” 2021. DOI: 10.1155/2021/6689597. [Online]. Available: https://doi.org/10.1155/2021/6689597.

[55] W. Fu, L. Zhang, X. Li, and X. Wu, “Numerical Investigation of Natural Convective Condensation with Noncondensable Gases in the Reactor Containment after Severe Accidents,” *Science and Technology of Nuclear Installations*, vol. 2019, 2019, ISSN: 16876083. DOI: 10.1155/2019/1673834.

[56] J. W. Kim, Y. G. Lee, H. K. Ahn, and G. C. Park, “Condensation heat transfer characteristic in the presence of noncondensable gas on natural convection at high pressure,” *Nuclear Engineering and Design*, vol. 239, no. 4, pp. 688–698, Apr. 2009, ISSN: 0029-5493. DOI: 10.1016/J.NUCENGDES.2008.12.011.

[57] H. J. Bart and S. Scholl, *Innovative heat exchangers*. 2017. DOI: 10.1007/978-3-319-71641-1.

[58] National Institue of Standards and Technology. “Water.” (), [Online]. Available: https://webbook.nist.gov/cgi/cbook.cgi?ID=C7732185&Mask=4&Type=ANTOINE&Plot=on#ANTOINE (visited on 03/03/2022).

[59] National Institue of Standards and Technology. “Methyl Alcohol.” (), [Online]. Available: https://webbook.nist.gov/cgi/cbook.cgi?ID=C67561&Mask=4&Type=ANTOINE&Plot=on (visited on 03/03/2022).

[60] L. Wu, Y. Liu, and H.-J. Jia, "Improved diffusion layer model based on real gas state equation for high pressure condensation," DOI: 10.1016/j.anucene.2015.05.006. [Online]. Available: http://dx.doi.org/10.1016/j.anucene.2015.05.006.

[61] Y. B. Peng, Y. J. Zhang, X. Z. Ma, and L. Wu, "Research on Pressure Influence Characteristic of Steam Condensation in Presence of Non-condensable Gas on Vertical Wall," *Yuanzineng Kexue Jishu/Atomic Energy Science and Technology*, vol. 51, no. 10, pp. 1813–1819, Oct. 2017, ISSN: 10006931. DOI: 10.7538/YZK.2017.YOUXIAN.0087. [Online]. Available: https://www.researchgate.net/publication/322445717_Research_on_Pressure_Influence_Characteristic_of_Steam_Condensation_in_Presence_of_Non-condensable_Gas_on_Vertical_Wall.

[62] X. Ma, X. Xiao, H. Jia, *et al.*, "Experimental research on steam condensation in presence of non-condensable gas under high pressure," *Annals of Nuclear Energy*, vol. 158, p. 108 282, Aug. 2021, ISSN: 0306-4549. DOI: 10.1016/J.ANUCENE.2021.108282.

[63] *Weight & Density of Stainless Steel 304, 316, 316L & 303 in lb/in3, g/cm3, lb/ft3, kg/m3*. [Online]. Available: https://www.theworldmaterial.com/weight-density-of-stainless-steel/ (visited on 11/21/2022).

[64] *Hydrogen - Specific Heat*. [Online]. Available: https://www.engineeringtoolbox.com/hydrogen-d_976.html (visited on 11/21/2022).

[65] *Specific heat capacity of materials - The Engineering Mindset*. [Online]. Available: https://theengineeringmindset.com/specific-heat-capacity-of-materials/ (visited on 11/21/2022).

[66] "ChemSep: Program - Overview." (), [Online]. Available: http://www.chemsep.org/ (visited on 03/23/2022).

[67] "COCO: Software - Overview." (), [Online]. Available: https://www.cocosimulator.org/ (visited on 03/23/2022).

[68] S. M. Walas, *Phase equilibria in chemical engineering*. Butterworth, 1985, p. 671, ISBN: 978-1-4831-4508-2. DOI: 10.1016/C2013-0-04304-6.

[69] H. A. Kooijman and R. Taylor, *The ChemSep Book Second Edition*. 2000, p. 468, ISBN: 3831110689.

[70] E. C. Carlson, "Don't gamble with physical properties for simulations," *Chemical Engineering Progress*, vol. 92, pp. 35–46, 10 Oct. 1996.

[71] "304, 316 & l-grade stainless steels: What are the differences? | vortex." (), [Online]. Available: https://www.vortexglobal.com/resources/304-316-l-grade-stainless-steels-what-are-the-differences (visited on 11/21/2022).

[72] "Carbon and stainless steel pipe and tube dimensions and pressure rating tables - atlas steels." (), [Online]. Available: https://atlassteels.com.au/dimension-and-pressure-rating-charts-for-pipe-and-tube/ (visited on 11/21/2022).

[73] "Pressure calculator." (), [Online]. Available: https://www.alleima.com/en/technical-center/pressure-calculations/pressure-calculator/ (visited on 10/07/2022).

[74] G. Schreuder, "Optimization of a shell and tube heat exchanger within a small-scale Methanol Synthesis Reactor," Haagse Hoogeschool, 2020.

[75] E. R. Likhachev, "Dependence of water viscosity on temperature and pressure," *Translated from Zhurnal Tekhnichesko oe Fiziki*, vol. 48, pp. 135–136, 4 2003. DOI: 10.1134/1.1568496.

[76] "Dynamic viscosity of methanol from dortmund data bank." (), [Online]. Available: http://www.ddbst.com/en/EED/PCP/VIS_C110.php (visited on 10/09/2022).

[77] A. F. Mills, "Chapter 1," in *Basic Heat and Mass Transfer*, 2nd ed., Pearson Education Limited, 1998, ch. 1.

[78] M. Hölzem, M. J. Sprague, K. Harth, M. Schüssler, M. Karl, and S. Boneberg, *US6926880B2 - Methanol Reforming Catalyst Having A Reduced Volume Shrinkage*. United States Patent, Aug. 2005.

Technische Universiteit Delft